Collider Experiments: the LHC & Beyond

Roger Forty
CERN

The basic concepts of experimental particle physics at colliders are presented, over four introductory lectures, using examples taken from the highest energy collider in the world: the LHC at CERN.

Lecture 1: *Accelerators & experiments*, introduces the field, discussing the physics motivation for collider experiments, including the Standard Model and beyond, and the Dark Sector. It also covers (briefly) particle acceleration, including accelerator design, and the LHC. Then colliders around the world are discussed, at CERN and elsewhere, categorised according to their collider types. Finally collider experiments are introduced, including general aspects of proton collisions at the LHC.

Lecture 2: *Detectors & data*, discusses the detection of particles in collider experiments. It starts with tracking detectors, describing particle interactions, and gaseous, silicon and vertex detectors. Calorimetry is explained, both for electromagnetic and hadronic types, including a discussion of photon detection. This is followed by the techniques of particle identification, including a description of particle signatures, and methods of hadron identification. The lecture ends with a brief overview of aspects related to data taking, including triggering, data acquisition, and data analysis.

Lecture 3: *LHC physics highlights* presents a whistle-stop tour through a personal selection of highlights from LHC physics analyses to date, presented roughly in order of increasing rarity of the process. Starting with strong interactions, the measurement of cross-sections, jets, the quark-gluon plasma, and the top quark are discussed. The latter sits on the boundary with flavour physics (which follows next) as well as electroweak physics discussed afterwards. The selected highlights for flavour physics concern particle-antiparticle mixing, CP violation and rare decays, while for electroweak physics the study of the vector bosons, the W and Z, are covered. The lecture ends with a summary of the current knowledge of the Higgs boson's properties.

Lecture 4: *Looking beyond* is meant in two senses—looking beyond the Standard Model and also beyond the LHC. It begins with a summary of searches for physics beyond the Standard Model at the LHC, including Supersymmetry or other extensions, and Dark Matter. Possible hints of new physics in existing results are reviewed: the so-called flavour anomalies, the W mass, and the magnetic moment of the muon. Potential avenues for widening the search are then discussed, such as for long-lived or feebly-interacting particles, including experiments at non-collider facilities. Finally, the prospects for future colliders to follow the LHC are reviewed, including the HL-LHC, Higgs Factories and beyond.

Introduction

These are four introductory lectures covering the basic concepts of experimental particle physics at colliders, including the highest energy collider in the world: the LHC (Large Hadron Collider). I am an experimental particle physicist working at CERN, the European centre for particle physics based near Geneva on the border between Switzerland and France, the laboratory which organized this school. I work on LHCb (one of the LHC experiments) but have tried my best to be unbiased. Most lectures presented at this school were theoretical in nature, but testing theory with experiments is essential for scientific progress: a broad experimental programme, pushing back all of the frontiers (energy, intensity,

This article should be cited as: Collider Experiments: the LHC & Beyond, Roger Forty, DOI: 10.23730/CYRSP-2023-XXX.15, in: Proceedings of the 2023 CERN Latin-American School of High-Energy Physics,
CERN Yellow Reports: School Proceedings, CERN-2023-XXX, DOI: 10.23730/CYRSP-2023-XXX, p. 15.

and cosmic) is particularly relevant at this time, when there are compelling arguments for new physics but no clear guidance from theory as to where it will be found.

1 Accelerators & experiments

1.1 Physics overview and motivation

Particle physics is the study of the world around us, at the forefront of the human quest to understand what the world is made of and how it works. Understanding the make-up of the Universe can be pursued in two ways, either looking outward at what surrounds us at the largest scales (astronomy and cosmology) or inwards to see what things are made up of at the smallest scales (particle physics). The latter is achieved by depositing energy into a small volume, since the resolving power increases with energy—recall the dependence of wavelength λ on momentum, p: $\lambda = h/p$ (from de Broglie [1])—hence the alternative name of High Energy Physics.[1]

The two approaches are fundamentally linked, since cosmology tells us that the Universe has a finite lifetime, following the Big Bang approximately 14 billion years ago: it was created at high energy and has expanded and cooled since—so studying high energy collisions is like looking back in time to the conditions of the early Universe. The current knowledge of particle physics is encapsulated in a theoretical framework, the Standard Model of particle physics.[2] The constituents of matter are fermions (with spin half, quarks and leptons), the carriers of forces are bosons (with integer spin), and there is one scalar fundamental particle (spin zero): the Higgs boson. The masses of the particles vary over more than 14 orders of magnitude, see Fig. 1 (a). The reason for this highly non-trivial structure is one of the open questions in particle physics.

The forces experienced in Nature have been progressively unified, as shown in Fig. 1 (b); the remaining four fundamental forces are the following:

- **Strong:** that binds nuclei together, carried by the gluon; coupling[3] $\alpha_{\rm s} \sim 1$;
- **Electromagnetic:** responsible for electricity and magnetism as well as electromagnetic waves, carried by the photon; coupling $\alpha \sim 1/137$;
- **Weak:** plays a role in radioactivity e.g. the β decay $\rm n \to p e^- \nu_e$, and the shining of the Sun, carried by the weak vector bosons (W and Z); coupling (derived from the Fermi constant $G_{\rm F}$) $\sim 10^{-6}$;
- **Gravitation:** assumed to be carried by the graviton, coupling (derived from the gravitational constant G) $\sim 10^{-39}$.

They are described by quantum field theory, except gravitation, for which the current description in General Relativity has not yet been made compatible with quantum mechanics.

Each elementary particle has a corresponding antiparticle with opposite electrical charge, such as the negatively charged electron ($\rm e^-$) and its antiparticle the positron (with positive charge, $\rm e^+$). Symmetries and invariance play an important role in particle physics: Noether's theorem states that if a system

[1] Energies are quoted in eV, the energy gained by a charged particle if accelerated by 1 V (1 eV = 1.6×10^{-19} joule); masses also quoted in eV via the equivalence of energy and mass, $E = mc^2$ (strictly they should be written eV/c^2); 1 GeV = 10^9 eV.
[2] Bear in mind that there are also other Standard Models, e.g. of cosmology and the Sun.
[3] Note: couplings are scale dependent.

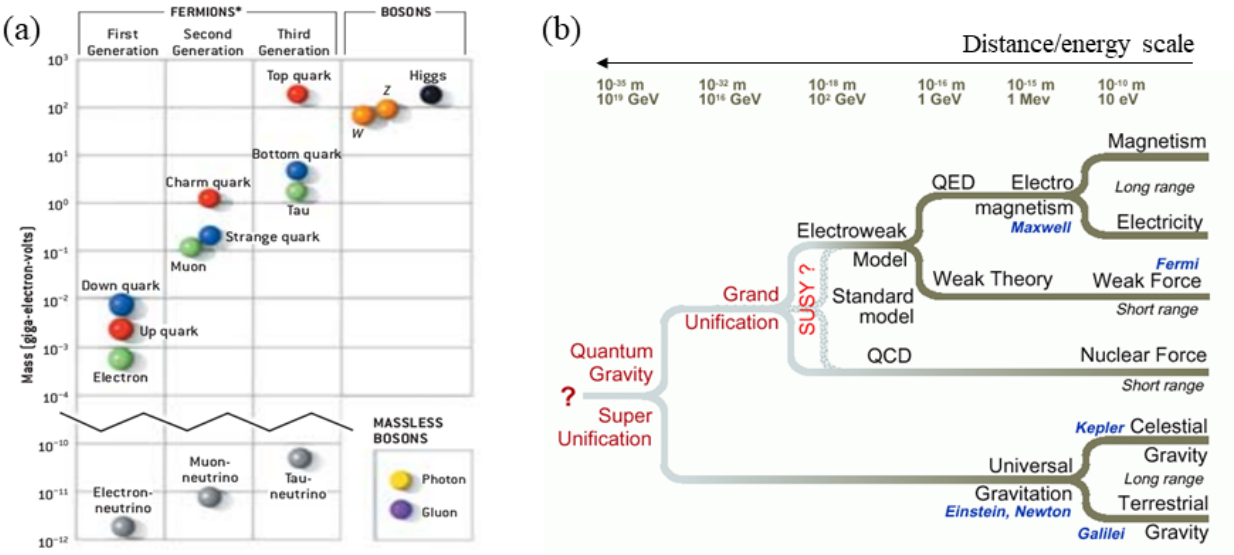

Fig. 1: (a) The masses of particles that make up the Standard Model [2]; (b) the progressive unification of the forces seen in Nature [3] (read from right to left, as the energy increases).

remains invariant under a continuous transformation, there is a corresponding conservation law, e.g. momentum conservation is a consequence of the invariance under spatial translation [4]. In addition to continuous transformations there are three possible *discrete* transformations:

- **C** = Charge conjugation: particles $\leftrightarrow$ antiparticles;
- **P** = Parity inversion: spatial coordinates $x, y, z \leftrightarrow -x, -y, -z$;
- **T** = Time reversal: time $t \leftrightarrow -t$.

The combined operation of all three is represented as CPT. Invariance under CPT is fundamental property of essentially all field theories, and guarantees that particles have exactly the same mass as their antiparticles. Although very rare in the every-day world, antiparticles are abundantly produced in high-energy collisions, in an equal amount as particles. Energy is transformed into matter (via $E = mc^2$) and particles and antiparticles are produced in pairs e.g. photon conversion: $\gamma \to \mathrm{e}^+\mathrm{e}^-$. [4]

The kinematics of two-particle scattering is described using the Mandelstam variables (s, t, u), combining particles' 4-momenta, as shown in Fig. 2 (a). The centre-of-mass energy in a collision of two particles is given by $\sqrt{s}$. Feynman diagrams are used to describe the interaction of particles, as illustrated in Fig. 2 (b)—technically, they show the spatial coordinate vertically and time horizontally, so the "s-channel" (e.g. $\mathrm{e}^+\mathrm{e}^-$ annihilation followed by creation) and "t-channel" (e.g. scattering of two electrons) processes are distinct.

The Standard Model's particle content was not complete when the LHC was built, 20 years ago. It was originally formulated for massless particles, but while $m_\gamma = 0$, the carriers of the weak force have $m_{\mathrm{W,Z}} \sim 100\,\mathrm{GeV}$. The mechanism of spontaneous Electroweak symmetry breaking was added

[4] Bringing antiparticles together to make *antimatter* e.g. $\mathrm{e}^+ + \overline{\mathrm{p}} \to \overline{\mathrm{H}}$ (antihydrogen) is studied at CERN at the antiproton decelerator (AD).

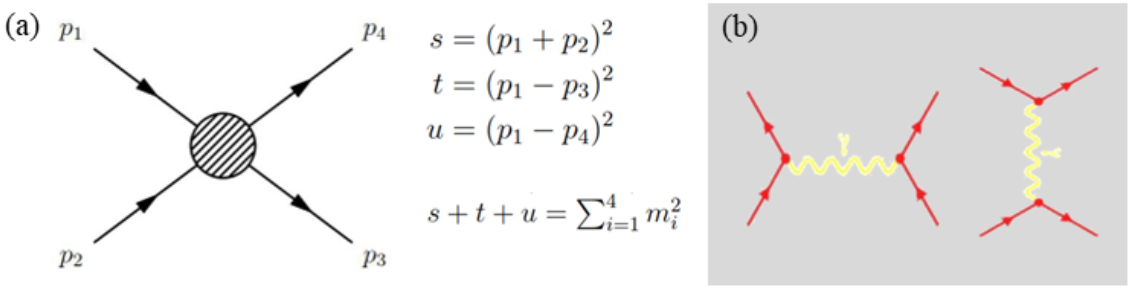

Fig. 2: (a) Definition of the Mandelstam variables describing two-particle interactions; (b) examples of Feynman diagrams, for an s-channel process (left) and t-channel (right).

$$
\begin{aligned}
\mathcal{L} \;=\; & -\frac{1}{4}B_{\mu\nu}B^{\mu\nu} - \frac{1}{8}tr(\mathbf{W}_{\mu\nu}\mathbf{W}^{\mu\nu}) - \frac{1}{2}tr(\mathbf{G}_{\mu\nu}\mathbf{G}^{\mu\nu}) && \text{(U(1), SU(2) and SU(3) gauge terms)} \\
& + (\bar{\nu}_L, \bar{e}_L)\,\tilde{\sigma}^{\mu} i D_{\mu} \begin{pmatrix} \nu_L \\ e_L \end{pmatrix} + \bar{e}_R \sigma^{\mu} i D_{\mu} e_R + \bar{\nu}_R \sigma^{\mu} i D_{\mu} \nu_R + \text{(h.c.)} && \text{(lepton dynamical term)} \\
& - \frac{\sqrt{2}}{v}\left[(\bar{\nu}_L, \bar{e}_L)\,\phi M^{e} e_R + \bar{e}_R \bar{M}^{e} \bar{\phi} \begin{pmatrix} \nu_L \\ e_L \end{pmatrix} \right] && \text{(electron, muon, tauon mass term)} \\
& - \frac{\sqrt{2}}{v}\left[(-\bar{e}_L, \bar{\nu}_L)\,\phi^{*} M^{\nu} \nu_R + \bar{\nu}_R \bar{M}^{\nu} \phi^{T} \begin{pmatrix} -e_L \\ \nu_L \end{pmatrix} \right] && \text{(neutrino mass term)} \\
& + (\bar{u}_L, \bar{d}_L)\,\tilde{\sigma}^{\mu} i D_{\mu} \begin{pmatrix} u_L \\ d_L \end{pmatrix} + \bar{u}_R \sigma^{\mu} i D_{\mu} u_R + \bar{d}_R \sigma^{\mu} i D_{\mu} d_R + \text{(h.c.)} && \text{(quark dynamical term)} \\
& - \frac{\sqrt{2}}{v}\left[(\bar{u}_L, \bar{d}_L)\,\phi M^{d} d_R + \bar{d}_R \bar{M}^{d} \bar{\phi} \begin{pmatrix} u_L \\ d_L \end{pmatrix} \right] && \text{(down, strange, bottom mass term)} \\
& - \frac{\sqrt{2}}{v}\left[(-\bar{d}_L, \bar{u}_L)\,\phi^{*} M^{u} u_R + \bar{u}_R \bar{M}^{u} \phi^{T} \begin{pmatrix} -d_L \\ u_L \end{pmatrix} \right] && \text{(up, charmed, top mass term)} \\
& + \overline{(D_{\mu}\phi)} D^{\mu}\phi - m_h^2[\bar{\phi}\phi - v^2/2]^2/2v^2. && \text{(Higgs dynamical and mass term)} \qquad (1)
\end{aligned}
$$

Fig. 3: The Standard Model Lagrangian, including neutrino mass terms [6].

via the Higgs mechanism[5] to fix this. The Higgs field gives particles mass and implies the existence of neutral scalar particle, the Higgs boson H. The Higgs boson mass m_{H} is not predicted, but must be below ~ 1 TeV to avoid violating unitarity in $\mathrm{W}^{+}\mathrm{W}^{-}$ scattering. The width of Higgs boson Γ_{H} increases with m_{H}; for m_{H} greater than about 1 TeV, the width would exceed the mass. The search for the Higgs boson was the Holy Grail of the LHC, and I will use that to illustrate the techniques of particle physics (spoiler alert: the Higgs boson *was* discovered, in 2012).[6]

For completeness, the full theoretical description of the Standard Model is given by its Lagrangian,[7] presented in Fig. 3. The Lagrangian is related to the action S which describes how a physical system changes over time, choosing the path of least action; $S = \int \mathcal{L}\, d^4x$.

Free quarks are not seen: this is the confinement property of QCD, they are bound together by gluons into colourless hadrons.[8] Hadrons mostly take the form of $q\bar{q}$ (mesons) or qqq (baryons), as illustrated in Fig. 4 (a). There are *many* types of them, corresponding to permutations of the six quarks q plus antiquarks $\bar{q}$. Most of their mass comes from their binding energy. Clear evidence has now been found at the LHC (and beyond) for "exotic" hadrons that do not fit into this scheme: tetraquarks ($q\bar{q}q\bar{q}$)

[5] More correctly the BEH mechanism after those credited with its formulation: Robert Brout, Francois Englert, and Peter Higgs (around 1964) [5].
[6] For more details see the lectures of John Ellis.
[7] For more details see the lectures of Gustavo Burdman.
[8] For more details see the lectures of Giulia Zanderighi.

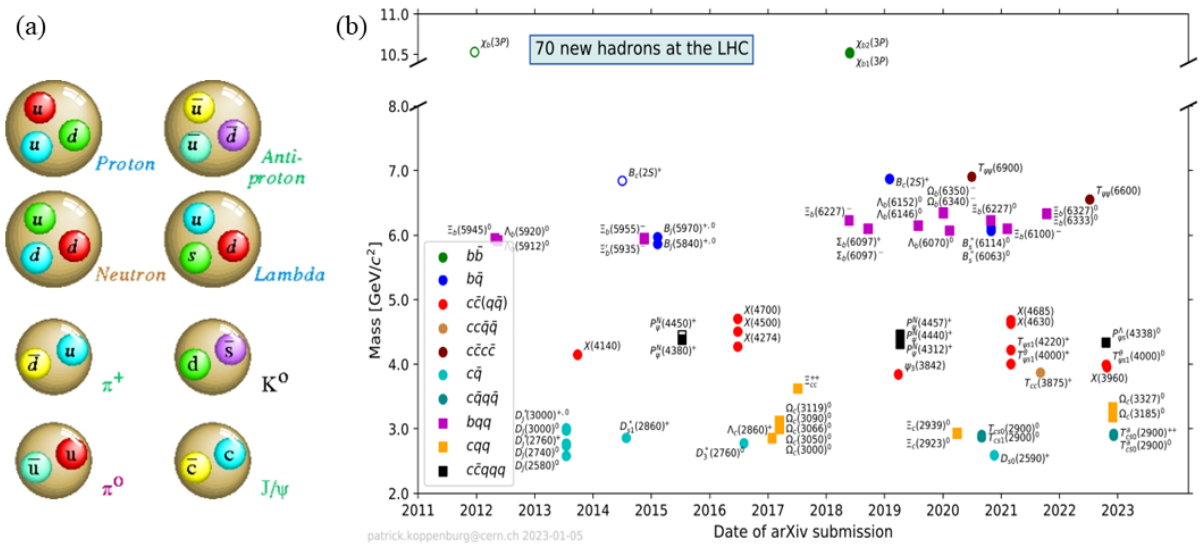

Fig. 4: (a) The quark composition of some common hadrons [3]; (b) new hadrons found at the LHC, with their mass plotted versus the date of their discovery [7]—the first convincing pentaquark was found in 2015 [8].

and pentaquarks ($q\bar{q}qqq$). The detailed structure of such hadrons is actively studied, but they can be accommodated within the Standard Model. The 70 new hadrons (and counting) so far found at the LHC, including such exotic types, are shown in Fig. 4 (b)—so the LHC has not "just found the Higgs boson and nothing else".

With the discovery of the Higgs boson, the Standard Model is complete. But there are compelling reasons why it cannot be the full story, including:

1. **Gravity:** The description of gravity (General Relativity) does not fit into the model. Why is natural scale of gravity, $m_{\rm P} = \sqrt{\hbar c/G} \sim 10^{19}$ GeV (the Planck mass), so much larger than the Electroweak scale $\sim 10^2$ GeV? This is known as the "hierarchy problem".
2. **Baryogenesis:** Why is the world we observe made up almost entirely of matter, while it is expected that equal quantities of matter and antimatter were produced in the Big Bang?
3. **Dark Matter:** Astrophysical measurements such as the rotations of galaxies indicate that normal "baryonic" matter makes up only $\approx 5\%$ of the total energy density of the Universe—what is the rest? Is it made up of elementary particles?

Answering these key questions drives the continued use of colliders. Let me add a few details concerning baryogenesis: in the Big Bang, matter and antimatter should have been equally produced, as in $\gamma \to {\rm e}^+{\rm e}^-$, and this would then have been followed by their mutual annihilation. We find $n_{\rm baryon}/n_\gamma \sim 10^{-10}$, so why didn't all of the matter annihilate (luckily for us)? No evidence has been seen for an "antimatter world" elsewhere in the Universe. One of the requirements to produce an asymmetric final state (our world) from a symmetric matter/antimatter initial state (the Big Bang) is that CP symmetry must violated [9]. CP *is* violated in the Standard Model (SM), through the weak mixing of quarks. For CP violation to occur there must be at least three generations of quarks, so the problem of baryogenesis may be intimately connected to why three generations exist, even though all normal matter is made up

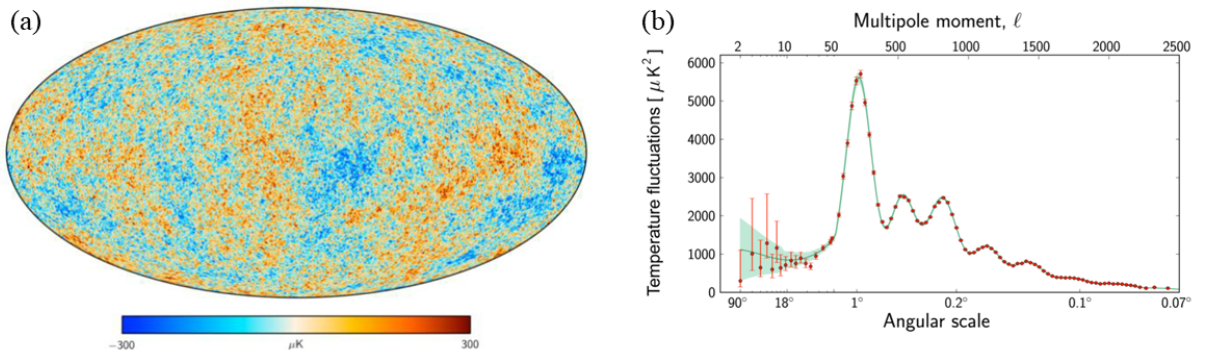

Fig. 5: (a) Fine structure seen in the temperature fluctuations of the cosmic microwave background; (b) analysis of the corresponding observed power spectrum, compared to the model [10].

from the first: $(\mathrm{u}, \mathrm{d}, \mathrm{e}, \nu_\mathrm{e})$. One way to probe CP violation is through the study of quark mixing: in particular, hadrons containing the b quark show large CP asymmetries. However, the CP violation seen in the SM is not sufficient to explain baryogenesis, and other sources of CP violation are expected, so this is a good place to search for new physics.

The Cosmic Microwave Background is the "afterglow" of the Big Bang. Since its accidental discovery in 1965, the CMB has been studied in greater and greater detail, detecting our relative motion to the rest of the Universe, and eventually resolving primordial structure, as shown in Fig. 5 (a). Analysis of its power spectrum, illustrated in Fig. 5 (b), has driven the development of the current cosmological model "ΛCDM" (Cosmological Constant Λ + cold dark matter).[9] The expansion of the Universe is *accelerating*, as discovered in 1998, and this is ascribed to "Dark Energy", a mysterious phenomenon that acts like the Cosmological Constant in the Einstein field equations of General Relativity, which represents the vacuum energy of empty space. Quantum fluctuations in the vacuum are expected, but when calculated they exceed the observed value by 120 orders of magnitude (known as "the worst prediction in physics", the Cosmological Constant problem). The evidence for Dark Energy is presented in Fig. 6 (a). It is a very rarefied phenomenon $\sim 10^{-27}$ kg/m^3, and is unlikely to be detectable at colliders: it is the province of the cosmic frontier, and it may e.g. require modifying our understanding of gravity.[10]

Of the remaining 28% of the mass-energy density of the Universe ascribed to matter, most does not appear to be normal "baryonic" matter—which leads to star formation and visible light. 23% is a form of matter that only appears to interact gravitationally, and not electromagnetically, known as Dark Matter. Clear evidence is seen for it from the rotation curves of stars in galaxies, as a function of distance from their centre (see Fig. 6 (b)), as well as from gravitational lensing. Only less than 5% of the mass-energy density is normal matter, so a lot remains to be understood! If Dark Matter is made up of particles, they are of unknown mass, and could be anywhere between 10^{-22} eV (from galaxy formation) up to black holes of tens of solar masses (from observational limits)—a vast space to be searched! Considering the possible two-particle interactions between normal matter (SM) and Dark Matter (DM) three avenues can be considered for investigation, as illustrated in Fig. 7:

[9] For more details see the lectures of Celine Boehm.
[10] Breaking news at the time of the school was a new suggestion that the accelerating expansion might instead be explained by Black Hole evolution [13].

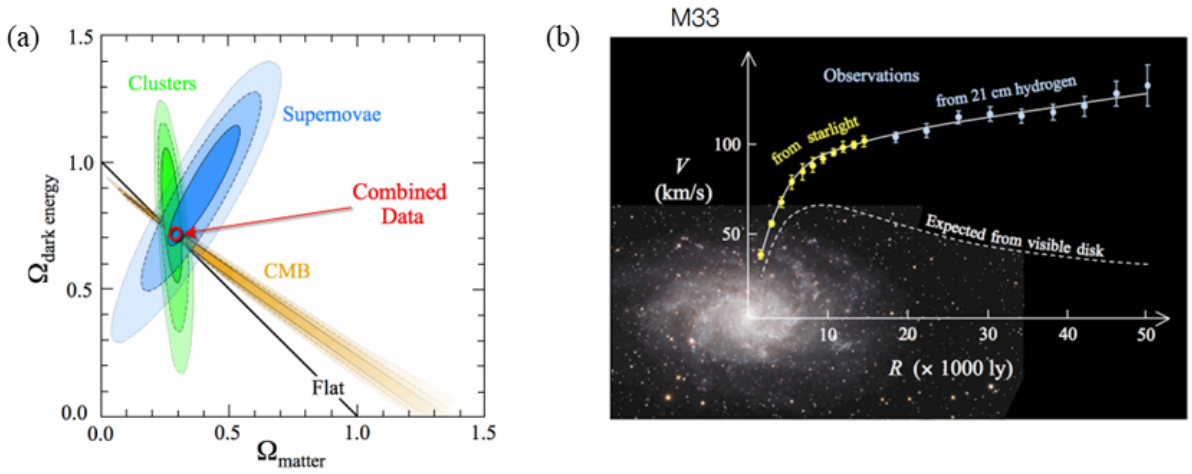

Fig. 6: The Dark Sector: (a) the evidence for Dark Energy, where Ω is the ratio of mass-energy density to the critical value for Universe to be flat; cosmological measurements indicate that $\sim$ 72% of mass-energy density of Universe should be attributed to Dark Energy [11]; (b) evidence for Dark Matter in the rotation curve of stars in a galaxy [12].

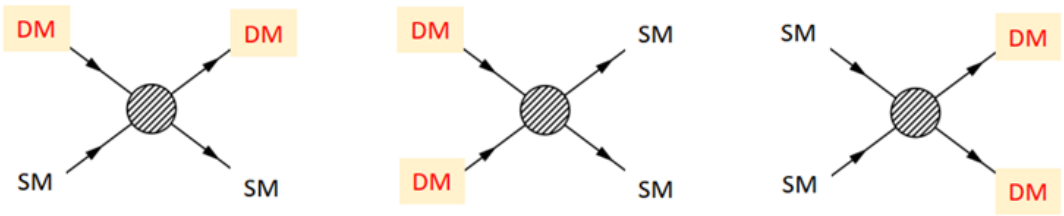

Fig. 7: The different approaches to searching for Dark Matter, direct detection (left), indirect detection (middle), and production at a collider (right).

1. **Direct Detection:** nuclear recoil when a DM particle scatters off the atomic nucleus of a target (the province of Underground experiments);
2. **Indirect Detection:** looking for the products of the annihilation or decay of DM particles (Astrophysics or Cosmic Ray experiments);
3. **Production at a collider:** producing DM particles by colliding SM particles at high energies (the province of collider experiments).

All three approaches are important and are being followed, providing complementary limits. The advantage of collider experiments is that parameters of the interaction are under control in the laboratory, and reproducible. On the other hand, cosmic rays reach higher energies than today's colliders. I will return to this topic in the 4^{th} lecture.

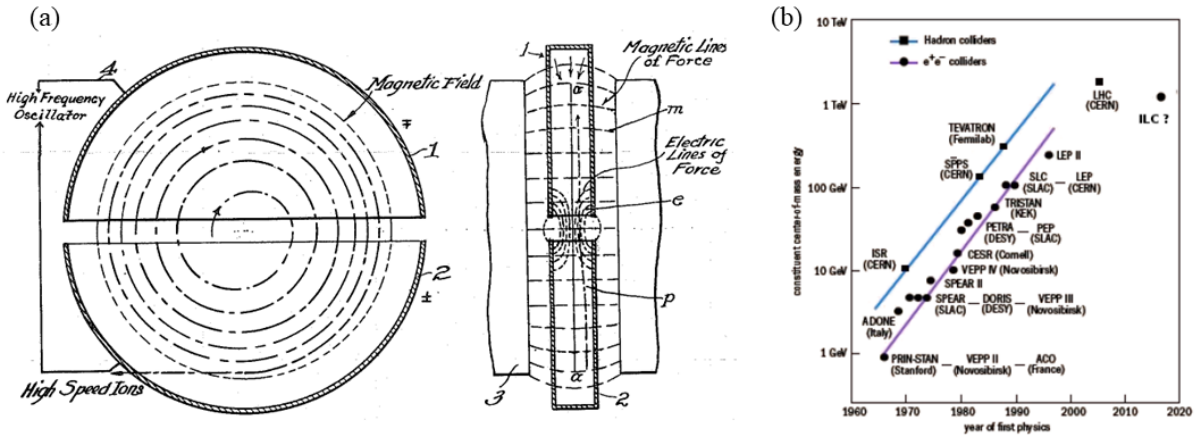

Fig. 8: (a) The design of the Cyclotron [14]; (b) the energy of colliders over the years (on a logarithmic scale) [15].

1.2 Particle acceleration

Charged particles are influenced by applied electric and magnetic fields according to the Lorentz force: $\boldsymbol{F} = q(\boldsymbol{E} + \boldsymbol{v} \times \boldsymbol{B}) = d\boldsymbol{p}/dt$. The affect of the electric field $\boldsymbol{E}$ is to increase the particle's energy, while the magnetic field $\boldsymbol{B}$ leads to curvature of the particle trajectory. In a simple particle gun the energy gained by an electron for an applied voltage of 1 V is 1 eV, while the energy per beam of the LHC is 7 TeV (i.e. 7000,000,000,000 eV). To achieve such high energies, a magnetic field is used to deflect particles in a roughly circular orbit, so that they pass the accelerating gap many times, as first implemented in the Cyclotron back in 1929, see Fig. 8 (a). Varying the fields with time allows the particles to be kept inside a small beam pipe, giving rise to the Synchrotron, widely used since the 1950s. The electric field to accelerate particles is applied using radio-frequency (RF) cavities, running at a frequency of 400 MHz for the LHC.

Early experiments used the extracted beam from the accelerator, fired onto a target ("fixed target"). The energy in the centre-of-mass frame $E_{\rm CM} = \sqrt{2m_{\rm p}\,E_{\rm beam}}$,[11] $= 115$ GeV for an LHC beam hitting a proton target. By colliding beams rotating in opposite directions $E_{\rm CM} = 2E_{\rm beam} = 14,000$ GeV at the LHC, a dramatic increase! The previous collider at CERN before the LHC, the Large Electron Positron collider (LEP), used oppositely charged beams (e^+ and e^-) so they follow the same trajectory through the magnets, and stay inside a single beam pipe. The energy was limited by synchrotron radiation losses: the power radiated $dE/dt \propto E^4 q^2/m^4\rho^2$ for a particle of mass m and charge q, and a bending radius ρ, which gave $\sim$ 2 GeV/turn at LEP, requiring $\sim$ 10 MW of electrical power to replace that lost by radiation. To reach higher energy, heavier particles can be used instead to reduce the synchrotron loss, hence the choice of protons in the LHC.[12] $E_{\rm LHC}/E_{\rm LEP} = 70$, but $m_{\rm p}/m_{\rm e} = 1800$, so the synchrotron loss at the LHC is only $\sim$ 6 keV/turn.

The increasing energy of colliders over the years is shown in Fig. 8 (b), illustrating the roughly exponential increase in energy versus time, although this will be difficult to maintain in the future. Lepton colliders like LEP are good for precision studies. Hadron colliders like the LHC are typically designed to

[11] Relativistic kinematics need to be used: at 7 TeV a proton has 99.999999% of the speed of light.
[12] Or one can go back to linear acceleration, and make the accelerator very long.

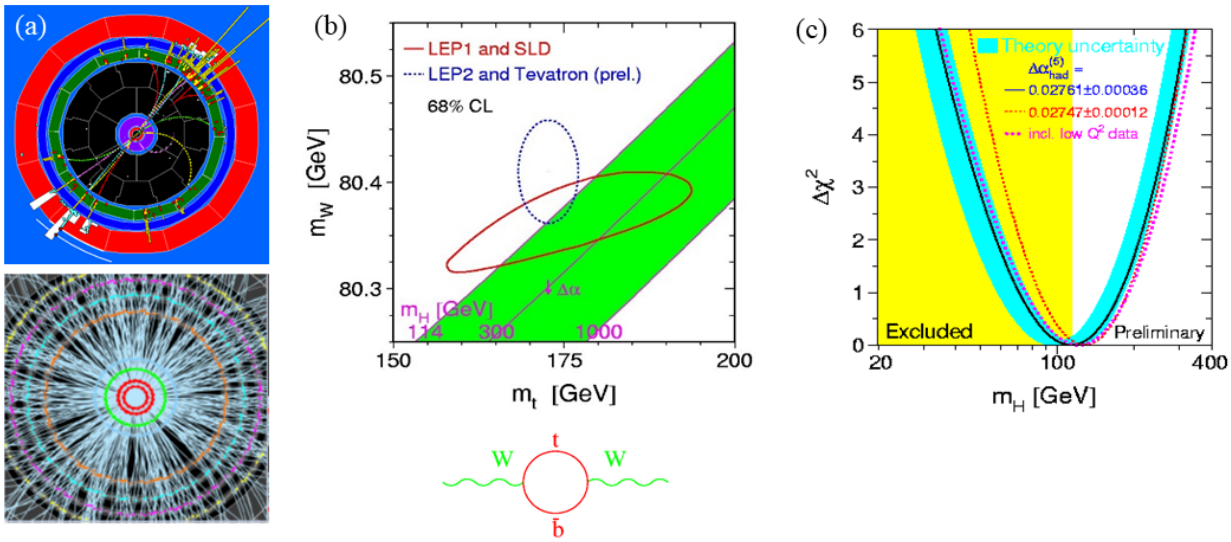

Fig. 9: (a) Event displays from experiments at LEP (above) and the LHC (below) illustrating the difference in complexity; (b) early results for the W mass *vs* top-quark mass compared to the prediction as a function of the Higgs boson mass (green band), with a diagram of a quantum contribution to the radiative corrections to the W mass (below); (c) the resulting constraints on the Higgs mass that came from LEP [16].

probe the energy frontier and are discovery machines, but are more challenging to use for precision studies due to the complex environment: protons are not elementary particles, and have strong interactions giving rise to many background tracks. LEP ran from 1989 to 2000 and collided e^+ e^- at $\sqrt{s} = 91$ GeV (m_Z) then 160 GeV (2 m_W) and finally $\sim$ 210 GeV to search for the Higgs boson. Each recorded collision in an experiment is known as an event, and a view of an event in one of the LEP experiments in the plane transverse to the beams is shown in Fig. 9 (a), showing the hits in the different detectors. This can be contrasted to a typical event at the LHC from proton-proton collisions at 13 TeV shown below, where one gets an impression of the complex, high-multiplicity events! I will return to a discussion of the detectors involved in making such event displays in the 2$^{\text{nd}}$ lecture.

Many measurements were made at LEP of the electroweak properties of the Z and W bosons. All were consistent with Standard Model predictions e.g. for the W mass. This is subject to radiative corrections, $m_W = m_0/\sqrt{1-\Delta r}$, as sketched in Fig. 9 (b), which depend in turn on the top quark and Higgs boson masses: $\Delta r = f(m_t^2, \log m_H) \approx 3\%$—this is example of an *indirect* search, where the measured results could constrain the Higgs mass, before it had been seen directly. Direct searches for the Higgs boson were also made at LEP, and led to a lower limit of $m_H > 114$ GeV (at 95% CL). Including this along with result of the electroweak fit gave $m_H < 200$ GeV (at 95% CL), see Fig. 9 (c), i.e. after analysis of the LEP data the Higgs boson was predicted to be "just around the corner" for discovery at the LHC.

The CERN accelerator complex is shown in Fig. 10. CERN has a wide variety of accelerators, some dating back to the 1950s. The LHC machine re-uses the tunnel that was excavated for LEP. Others (such as the PS or SPS) are used to accelerate protons before injection into the LHC, as well as maintaining their own physics programmes. Following the path of the protons that are accelerated in the LHC,

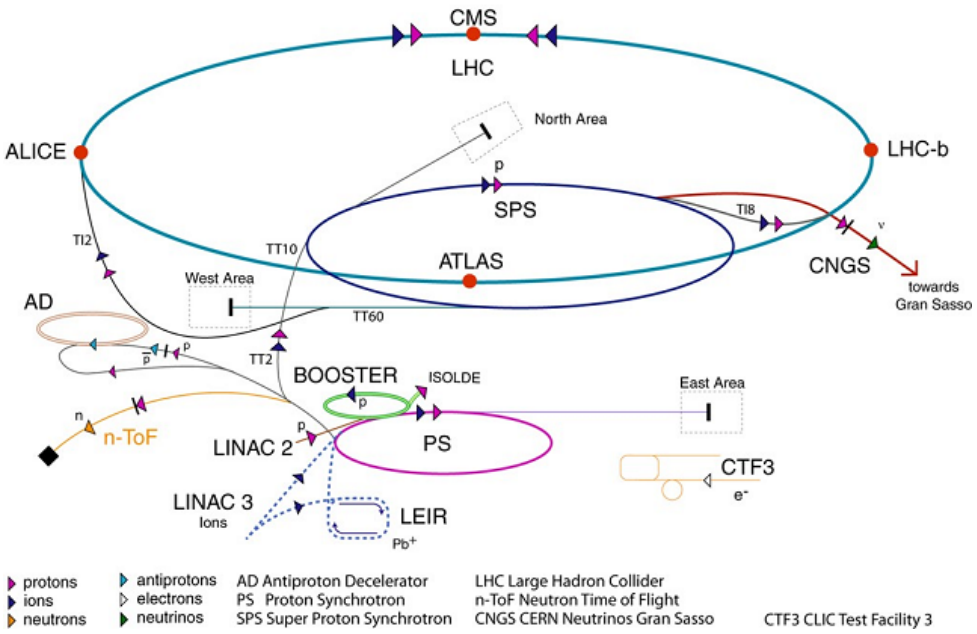

Fig. 10: The complex of accelerators at CERN; note that CNGS was an earlier neutrino beam sent to the LNGS lab at Gran Sasso in Italy, now replaced by studies for wake-field acceleration.

they start their lives as hydrogen nuclei in a gas bottle, from which they are extracted at 90 keV; a linac then accelerates the beam to 50 MeV over 33 m, providing one beam pulse every 1.2 s; the PS Booster is the first synchrotron in the chain, with 157 m circumference, which increases the proton energy to 1.4 GeV in 1.2 s; the PS is the oldest operating synchrotron at CERN, with 628 m circumference, and increases the proton energy to 26 GeV; the SPS has 6.9 km circumference, 30 m underground, and increases proton energy to 450 GeV, with up to 5×10^{13} protons per cycle; it provides beam both to the LHC and fixed-target areas. Finally the LHC itself has 26.7 km circumference and is located about 100 m underground, with four interaction points where the major experiments are sited, shown in Fig. 11 (a).

Dipole magnets are used to deflect the particles around the ring. The resulting radius of curvature r [m] = p [GeV] $/0.3\,B$ [T]. For the LHC, the machine had to fit in the existing 27 km tunnel, about $2/3$ of which is used for active dipole field. Hence $r \approx 2800$ m, so to reach $p = 7$ TeV requires $B = 8.3$ T. The beams are focused using quadrupole magnets. By alternating focusing and defocusing quadrupoles, one can arrange for focusing in both the horizontal and vertical planes. The LHC has 1232 dipoles and 858 quadrupoles in total. Earlier hadron colliders, such as the Tevatron in the US or the $\mathrm{Sp\overline{p}S}$ at CERN, collided protons against antiprotons, with the simplification that they would follow the same trajectory in the beam pipe, but their luminosity was limited by the available supply of $\overline{\mathrm{p}}$. The LHC beams are instead formed from counter-rotating bunches of protons (see Fig. 11 (b)) so separate beam pipes are needed, and a clever two-in-one design was devised where the two beam pipes sit inside the same magnet with opposite B field in each pipe, visible in Fig. 11 (c). High vacuum is needed in the pipes to avoid losing protons through collision with the residual gas: the pressure is kept below 10^{-10} mbar, similar to outer space. Care needs to be taken to ensure that the beams collide at the interaction points.

To achieve the high field required to reach 14 TeV the dipole magnets are wound using cable of niobium-titanium alloy (embedded in copper). This is a superconductor (i.e. suffers from no electrical

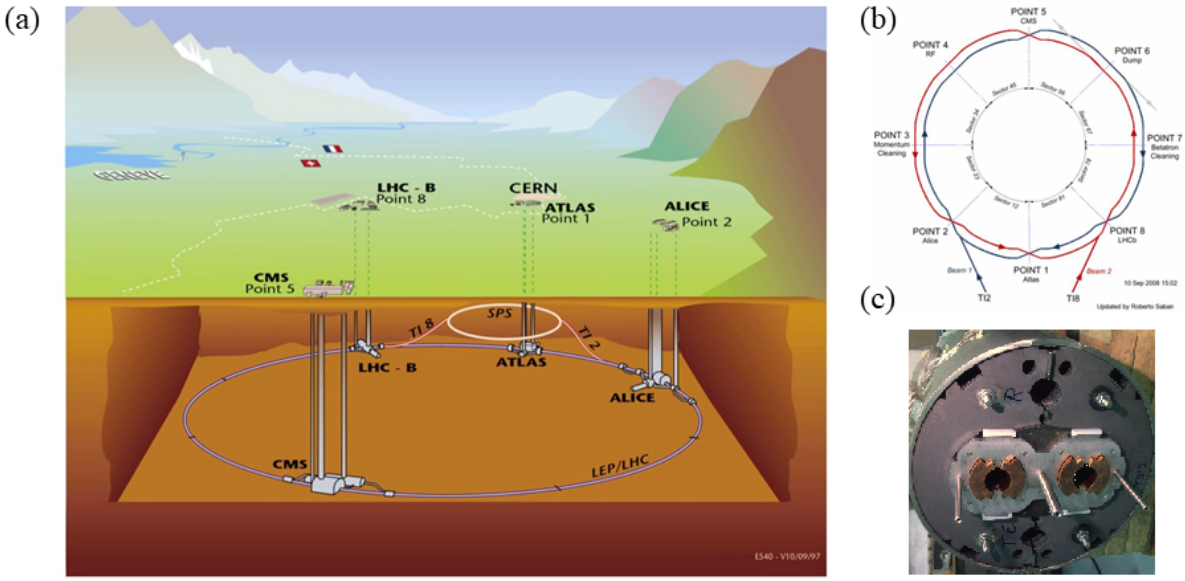

Fig. 11: (a) Artist's impression of the LHC tunnel and its experiments in underground caverns; (b) the bunches of protons that make up the counter-rotating beams; (c) an LHC dipole magnet, with twin beam apertures side by side.

resistance) if it is kept below the "critical surface" in the space of current density, flux density and temperature. To reach 8.3 T the coils are cooled to 1.9 K ($-271°$C, colder than outer space!). They carry a current of 11,700 A. The cooling is performed using liquid helium, and about 700,000 litres are required, making this the largest cryogenic system in the world.

Taking the search for the Higgs boson as a guide for the choice of the LHC parameters, there are various possible production diagrams, shown in Fig. 12; the $\mathrm{gg} \to \mathrm{H}$ process dominates at the LHC, and the predicted production cross-section is the order of a few picobarns, depending on mass.[13] On the other hand the total production cross-section at the LHC, $\sigma(\mathrm{pp} \to \mathrm{anything}) \approx 0.1$ barn, as shown in Fig. 12 (c). A 10 pb cross-section for the Higgs boson corresponds to one being produced every 10^{10} interactions! (and this is further reduced by the branching ratio to a given final state and the efficiency to reconstruct that state). Experiments have to be designed so that they can separate such a rare signal process from the background. The rate of interaction $= L \cdot \sigma$, where luminosity L is a measure of how intense the beams are (in units $\mathrm{cm}^{-2}\mathrm{s}^{-1}$). A "fill" of the LHC with beam can last a few hours, with the luminosity gradually decreasing as the protons interact, until eventually the beams are dumped and the machine refilled.

The luminosity of two colliding beams is given by: $L = N_1 N_2 k_\mathrm{b} f / A$, where (at the LHC) $N_1 = N_2 = 10^{11}$ p/bunch, the number of bunches $k_\mathrm{b} = 2808$, the revolution frequency $f = c/27$ km = 11 kHz, the effective area of the beam $A \approx 4\pi\,\sigma_x\,\sigma_y$, and the transverse beam size $\sigma_x \approx \sigma_y \approx 16\,\mu$m (RMS). The beams are strongly focused at the interaction points (IP) to maximize the luminosity. There is an additional factor $\mathcal{O}(1)$ that accounts for the beam crossing angle. This gives $L = 10^{34}\,\mathrm{cm}^{-2}\mathrm{s}^{-1}$

[13] Reminder: cross-section σ measures the probability of a reaction taking place; its unit is the barn (b): 1 barn $= 10^{-24}\mathrm{cm}^2$ ($\sim$ area of the nucleus), so 1 pb $= 10^{-36}\mathrm{cm}^2$.

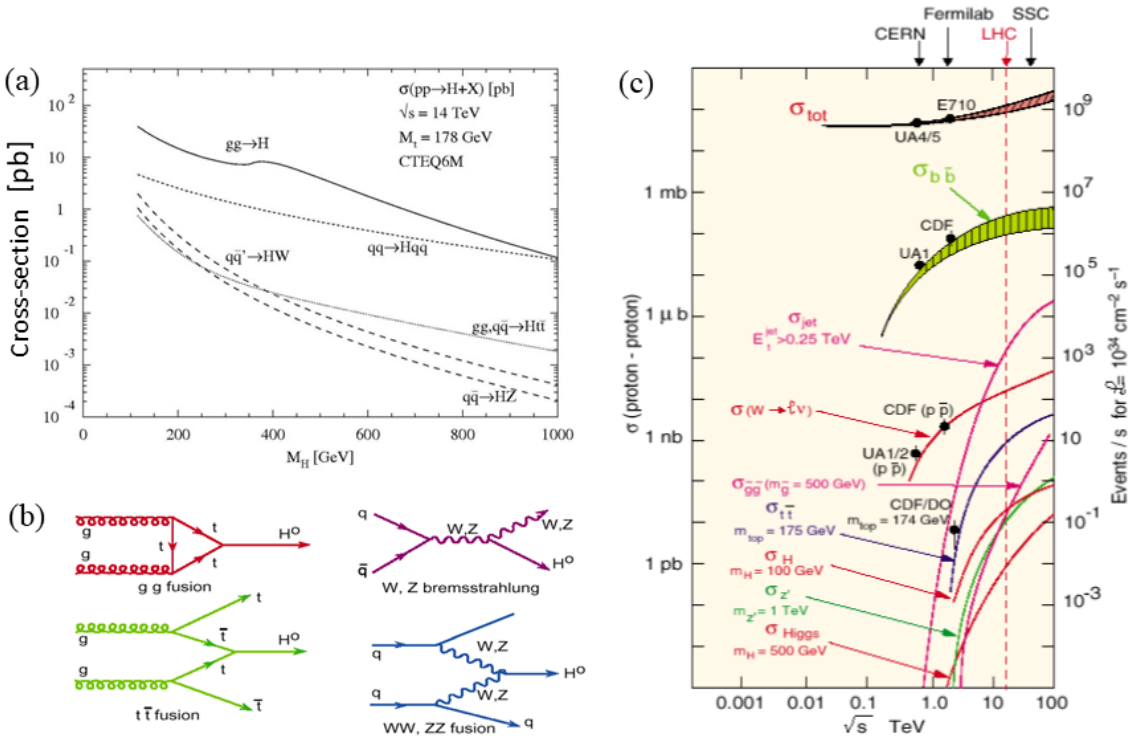

Fig. 12: (a) the Higgs production cross-section as a function of its mass [17]; (b) the various diagrams that contribute; (c) a compilation of cross-sections for different processes versus the collision energy [18].

(the design luminosity of the LHC), corresponding to about 0.6 amps of beam current. The *integrated* luminosity $L_{\text{int}} = \int L\,dt$ is what the experiments care about: it gives the total number of events produced for a given process, when multiplied by its cross-section. Assuming $\sim 10^7$ seconds of physics running per year (about 4 months, operating 24 hours/day) gives $L_{\text{int}} = 100\,\text{fb}^{-1}$/year ("inverse femtobarns").[14] The luminosity can also be expressed in accelerator-physics terms, replacing A in the equation above with $\varepsilon\beta^*/\gamma$: the emittance ε quantifies the beam brightness, given by its area in (x, x') phase-space, and Liouville's theorem [19] states that ε is a conserved quantity around the ring; β^* is the focusing strength at the IP (a parameter of the beam-optics function) and γ is the relativistic boost ($= E/m_0$).

At the design luminosity of the LHC the stored energy in each beam is 2808 bunches $\times 10^{11}\text{p} \times 7\,\text{TeV} = 400$ MJ. This corresponds to the explosive energy of about 100 kg of TNT, or the kinetic energy of a train travelling at 165 km/h! Extreme care has to be taken that none of this energy is lost into the superconducting magnets—it would cause them to quench, i.e. lose superconductivity and heat up, with potentially stressful consequences for the magnet construction—so an efficient collimator system and beam dump are essential, using e.g. graphite absorbers. Magnets have to be "trained" to reach high field, which requires many quenches, and is why the LHC beam energy is currently limited to 6.8 TeV, i.e. not quite reaching the design energy of 7 TeV (yet).

[14] An integrated luminosity of $100\,\text{fb}^{-1}$/year means that a process with cross-section of 1 fb will occur with a rate of 100 times/year (on average).

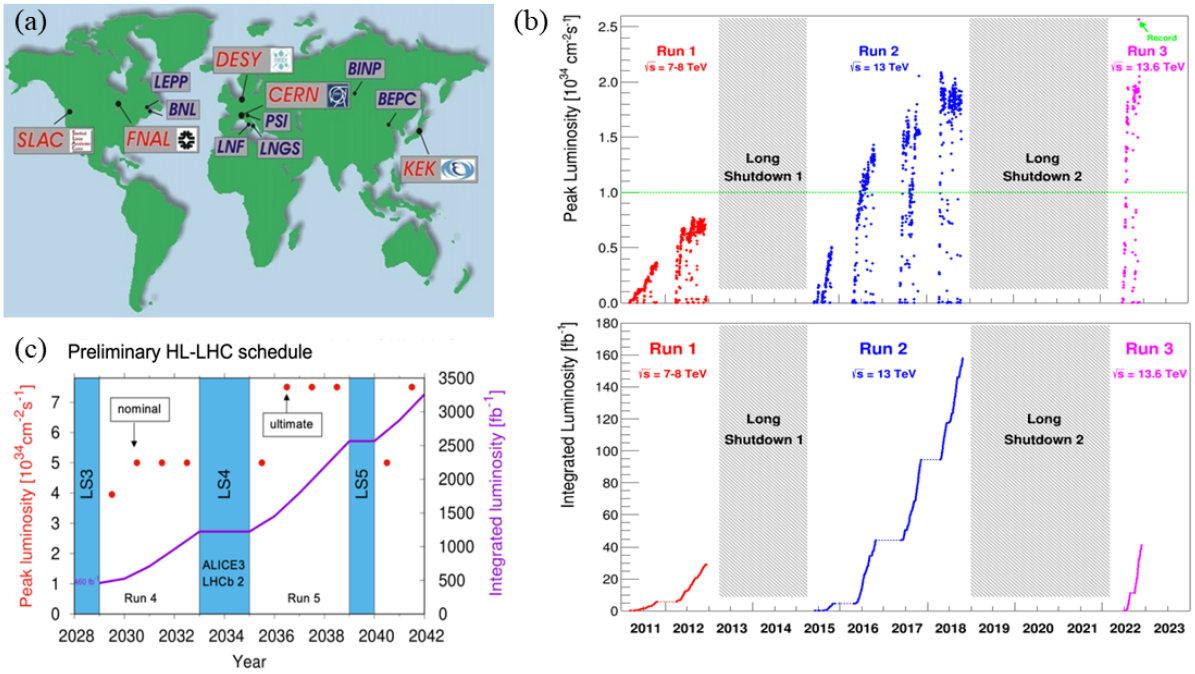

Fig. 13: (a) Major particle physics laboratories around the world [21]; (b) the luminosity of the LHC as a function of time, instantaneous (above) and integrated (below), as delivered to the general-purpose experiments ATLAS & CMS; (c) preliminary schedule for HL-LHC.

1.3 Colliders around the world

The title of this section brings to mind Fermi's speculation in 1954 about the highest possible energy that could be reached on Earth. He assumed fixed-target operation, 2 T magnets, and only reached 3 TeV for a circumference of 50,000 km encircling the entire world, with an estimated cost of 200 billion dollars. The LHC achieved 13.6 TeV, 50 years later, at a fraction of that cost ($\sim$ 5 B\$) in a 27 km tunnel: due to unforeseen developments in technology (8 T superconducting magnets) and clever idea (collider operation) that Fermi had not foreseen. The moral of the story is that we should keep optimistic, and look out for future breakthroughs![15] Meanwhile, the colliders operating around the world, currently or recently, will be discussed.

The major particle physics laboratories are shown in Fig. 13 (a). CERN is the largest: it is named from its original title Conseil Européen pour la Recherche Nucléaire, but is more usually referred to as the European laboratory for particle physics. It was founded in 1954 by intergovernmental treaty, and now has 23 Member States, 10 Associate Member States, 4 Observers (including the US), and about 50 International Cooperation Agreements with non-Member States. The CERN annual budget is 1.3 BCHF, provided by the Member States based on their net income. It is devoted to science for peace, with no military research permitted and all results published—those from the LHC are all open access. CERN's community includes more than 16,000 people from over 110 nationalities, made up of 2700 staff, 800 post-doctoral fellows, 12,700 users and other associates, and 3000 PhD students from all over the world. The laboratory takes care of running the accelerators on its site (such as the LHC), while the experiments are built and run by collaborations of users from institutes around the world—ATLAS and CMS each

[15] Pop quiz: if its circumference of 50,000 km is increased by 1 m, how far from the earth's surface would Fermi's collider move? (the answer is given in Ref. [20]).

Table 1: The parameters of colliders that are currently in operation, or which recently completed.

Lab.	Country	Collider	Beams	Energy [GeV]	Lumi. $[10^{30}/\mathrm{cm}^2\mathrm{s}]$	Circ. [km]	Dates	Experiments
FNAL	US	Tevatron	$\mathrm{p\overline{p}}$	900+900	400	6.3	1983-2011	CDF, D0
CERN	Europe	LEP	$\mathrm{e^+e^-}$	45+45 (Z)	100	26.7	1989-1995	ALEPH, OPAL,
		LEP II		104+104			1996-2000	DELPHI, L3
SLAC	US	SLC	$\mathrm{e^+e^-}$	45+45 (Z)	3	3.2*	1989-1998	SLD
DESY	Germany	HERA	$\mathrm{e^{\pm}p}$	27+920	15	6.4	1992-2007	H1, HERMES, ZEUS, HERA-B
LNF	Italy	DAFNE	$\mathrm{e^+e^-}$	1+1 (ϕ)	240	0.1	1999-2018	KLOE
SLAC	US	PEP II	$\mathrm{e^+e^-}$	3+9 (Υ)	5000	2.2	1999-2008	BaBar
KEK	Japan	KEKB	$\mathrm{e^+e^-}$	4+7 (Υ)	13000	3.0	1999-2010	Belle
		SuperKEKB			46000		2019-	Belle II
BNL	US	RHIC	pA, AA	250+250	160	3.8	2000-	STAR, PHENIX
IHEP	China	BEPC II	$\mathrm{e^+e^-}$	2+2 (ψ)	10	0.2	2006-	BES III
CERN	Europe	LHC	pp, pA, AA	6800+6800	25000	26.7	2009-	ALICE, ATLAS, CMS, LHCb, ...

*linear

have about 3000 authors.[16]

There are many thousands of accelerators in operation today, mostly for medical or industrial applications, but only a few *colliders*—the latter are only used for particle physics research. Current and recent examples are listed in Table 1. They can be grouped into different categories: (i) particle factories, (ii) heavy-ion, (iii) electron-proton, and (iv) discovery machines.

Particle factories arrange their beam energy to sit on the resonance of a known particle, so that they are copiously produced. LEP was a Z factory in its first phase (as was SLC) then moved to higher energy, above the $\mathrm{W^+W^-}$ threshold (since the W is charged, it cannot be made singly in $\mathrm{e^+e^-}$ collisions). DAFNE's energy was chosen to sit on the ϕ ($\mathrm{s\overline{s}}$ meson) which decays to $\mathrm{K^+K^-}$ or $\mathrm{K^0\overline{K}^0}$. BES III sits on (or near) the ψ ($\mathrm{c\overline{c}}$), decaying to charm and τ-leptons. BaBar and Belle were B Factory experiments, with their colliders tuned to sit on the Υ(4S), an excited state of the Υ ($\mathrm{b\overline{b}}$ meson), which is heavy enough to decay to $\mathrm{B\overline{B}}$ meson pairs. In the future, plans are being made for a Higgs Factory (I will return to this in the 4$^{\mathrm{th}}$ lecture). In B Factories the beam energies are chosen to be asymmetric between $\mathrm{e^+}$ and $\mathrm{e^-}$ so that the $\mathrm{B\overline{B}}$ pairs are boosted in the laboratory frame, allowing the lifetime information to be measured, important for CP violation studies. The Belle collider has been upgraded, to reach higher luminosity: now known as SuperKEKB it is one of the few colliders currently operating outside CERN (in KEK, Japan), with beam spot $\sigma_y \approx 100$ nm (referred to as "nanobeams"). It currently holds the world record for luminosity of $4.6 \times 10^{34}\,\mathrm{cm^{-2}s^{-1}}$, as a leading programme on the so-called "intensity frontier". Belle II aims to integrate 50 $\mathrm{ab^{-1}}$ (= 50,000 $\mathrm{fb^{-1}}$) in its current run and will compete with LHCb in the study of flavour physics (b hadrons, etc.).[17]

[16] Specific programmes to encourage CERN-Latin America collaboration have included HELEN: High-Energy physics Latin-American European Network (2005-9) and EPLANET: European Particle physics Latin-American NETwork (2011-15).

[17] The cross-section is much larger at the LHC energy for LHCb, so 1 $\mathrm{fb^{-1}}$ there is equivalent to about 1 $\mathrm{ab^{-1}}$ at a B Factory.

Heavy-ion colliders include RHIC (the Relativistic Heavy Ion Collider) that collides the nuclei of heavy atoms (Al, Au, Cu, Zr, Ru, U) as well as protons. The atoms are fully ionized before being accelerated. Due to their large mass, the energy density that can be achieved in the collisions is phenomenal, and the properties of matter at high temperature and density can be studied, as it was soon after the Big Bang ($< 10^{-6}$ s): hadrons are expected to "melt" to form a quark-gluon plasma. The LHC can also collide heavy-ions, usually Pb-Pb, although this requires a dedicated mode of operation so is in competition with the pp running, with about 4 weeks/year typically being devoted to heavy-ion running.

HERA was a classic example of an **electron-proton collider**. The main physics programme there was deep inelastic scattering, allowing detailed study of the proton structure. The EIC (Electron-Ion Collider) has been approved in the US to continue such studies, including polarized electrons to study spin effects. It aims to be operating at BNL by around 2030.

The final category of collider types is **discovery machines** like the Tevatron, the previous highest energy collider before the LHC. It collided protons and antiprotons up to 1.8 TeV. The experiments integrated about 10 fb^{-1} of luminosity, and made important discoveries such as the top quark (1995), before it finished operation in 2011. The SSC (Superconducting Super Collider) was proposed in the US as a competitor to the LHC, with circumference of 87 km and beam energy 20 TeV, but was cancelled in 1993 after cost overrun. Like them, the LHC is a discovery machine, pushing to the highest possible collision energy: the "energy frontier".

The LHC time-line illustrates the long-term nature of modern high-energy collider projects:

1984: first discussions took place of installing the LHC in tunnel of LEP, at a workshop in Lausanne;

2008: during the LHC startup an "incident" occurred with a magnet interconnect: a superconductor joint failed, causing catastrophic He-release that caused serious local damage to the magnets;

2010: the machine started up again, at lower energy (3.5 TeV beams, Run 1);

2016: run with 6.5 TeV beams (Run 2);

2022: run with 6.8 TeV beams (Run 3, in progress);

2029: high luminosity running (HL-LHC) is expected to start.

After the early teething trouble, the LHC has performed superbly, with over 200 fb^{-1} delivered to the general-purpose experiments, see Fig. 13 (b).[18] It is planned to continue running the LHC for another 20 years, with upgrades to reach higher luminosity (HL-LHC), see Fig. 13 (c).

1.4 Experiments at the LHC

The LHC collides protons, that are composite objects made up of partons (quarks and gluons), as illustrated in Fig. 14 (a). For each proton there is a probability that an individual parton carries a fraction "x" of the proton momentum, the "parton distribution function" shown in Fig. 14 (b). The effective centre-of-mass energy $\sqrt{s} = \sqrt{x_1 x_2 s}$. Partons typically only carry about 10% of the proton momentum, hence 7 TeV proton beams are needed to explore up to around 1 TeV in the parton collision centre-of-mass. The initial longitudinal momenta (along the beam axis, z) of the collision is not known ($x_1 \neq x_2$) and particles escape down the beam-pipe, so it is usual to work in the transverse plane where momentum is conserved. The variables used to describe pp interactions are:

[18] The luminosity delivered to LHCb can be tuned separately to the general-purpose experiments, and is chosen to be about an order of magnitude lower, to limit the complexity of the collisions; that delivered to ALICE is lower still.

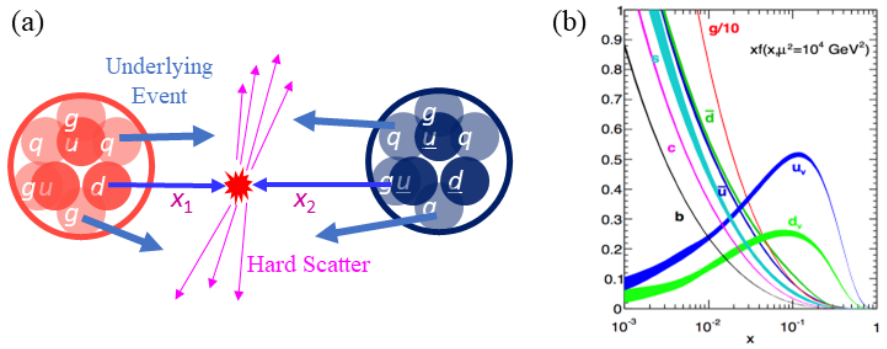

Fig. 14: (a) Schematic collision of partons from protons; (b) the parton distribution functions [22].

- **Transverse momentum** (perpendicular to the beam): $p_{\mathrm{T}} = p \sin\theta$, where θ is the dip angle relative to the beam axis;
- **Azimuthal angle**: ϕ, around the beam axis;
- **Rapidity**: $y = \frac{1}{2} \ln \frac{E+p_z}{E-p_z}$;
- **Pseudorapidity**: $\eta = -\ln \tan \theta/2$ (equal to rapidity in the massless limit, and easier to calculate).

p_{T}, Δy and $\Delta\phi$ are invariant under Lorentz boosts parallel to the z axis, i.e. the same when measured in the centre-of-mass or lab system. Particle production is roughly uniform when plotted vs rapidity, just extending to higher y as the energy increases.

Most pp interactions involve small momentum transfer: particles in the final state have large longitudinal momentum but small p_{T}: these are known as soft or "minimum bias" events. In a hard scatter, large-x partons collide head-on, and this comes with an "underlying event" from beam remnants, multiple parton interactions and radiation. Pileup refers to when there is more than one hard scatter in the same beam crossing, while out-of-time pileup (also known as spillover) refers to electronic signals belonging to earlier beam crossings. At the nominal LHC luminosity, the rate of inelastic pp interactions: $L\,\sigma_{\mathrm{tot}} = 10^{34}\,\mathrm{cm}^{-2}\mathrm{s}^{-1} \times 0.1\,\mathrm{b} = 10^{9}/\mathrm{s}$. The bunch crossing rate is given by the crossing frequency (11 kHz) $\times$ the number of bunches (2808) / 0.8 = 40 MHz, where the factor 0.8 is the fraction of the ring filled with bunches (gaps are needed for injection and beam dump). The ratio of these two numbers implies a pileup of about 25 pp interactions per bunch crossing, as illustrated in Fig. 15 (a), increasing with L, which gives an indication of the high occupancy seen in the general-purpose experiments.

If a pair of partons from each proton scatter off each other, this will usually lead to multiple jets of hadrons in the final state, but few leptons or photons; if, on the other hand, leptons with high p_{T} are observed then something interesting may have happened, such as Higgs boson production and decay. High p_{T} leptons and photons are important experimental signatures of such interesting events. Neutrinos and other escaping particles lead to missing energy, so the general-purpose detectors are designed to be "hermetic", i.e. as far as possible to catch all particles, over a large fraction of the 4π solid angle. However, energy can always escape down the beam pipe, so they measure the *transverse* energy balance to detect escaping particles: missing E_{T} is another important signature of interesting physics. Different types of massive particles have a chance of being created in each event, given by their cross-section. Most decay immediately into a few stable particles which are seen in the detectors. To look for the various decay products multi-component detectors are used, surrounding one other like layers of an

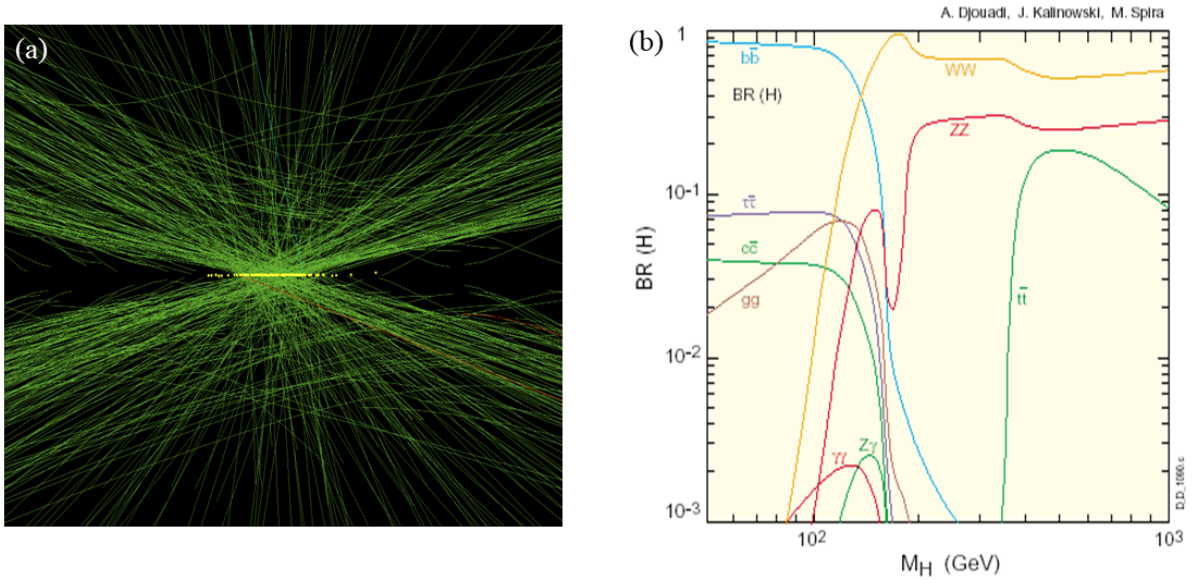

Fig. 15: (a) View of tracks in a general-purpose experiment at the LHC, showing the view along the beam axis with many piled-up interactions [23]; (b) the branching ratios of the Higgs boson to different final states as a function of its mass [24].

onion: these are the “sub-detectors" of the experiment. General-purpose detectors are usually cylindrical, with central barrel and removable endcaps for access to the sub-detectors. Each component measures different properties such as the energy or particle type of decay products, so the particles originally created in the collision can be identified. In particular, these experiments were designed to discover the Higgs boson. Since it couples to mass, the Higgs boson tends to decay into the highest mass particles that are kinematically allowed, as seen in Fig. 15 (b). At high mass, $\mathrm{H} \to \mathrm{ZZ}^* \to 4\mu$ is the easiest channel to detect. At low mass, the dominant $\mathrm{H} \to \mathrm{b\bar{b}}$ has a huge QCD jet background, so $\mathrm{H} \to \gamma\gamma$ is preferred instead: despite its low branching ratio, it is easier to pick out experimentally.

The LHC has four interaction points (IP) around which detectors are installed, shown in Fig. 16. Two are occupied by the general-purpose experiments ATLAS & CMS. They concentrate on high-p_{T} physics, such as searching for the Higgs boson and new particles, or precision physics with heavy particles (W, Z, top quark). **ATLAS** (A Toroidal Lhc ApparatuS, a rather contrived acronym) is the biggest HEP experiment ever, about the size of a five-story building: it is 45 m long and weighs 7000 tons; **CMS** (Compact Muon Spectrometer) might be *compact* compared to ATLAS, but is almost $2\times$ heavier: 21 m long, weighing 12,500 tons. The third experiment is dedicated to flavour physics—the physics of particles containing the b (beauty) and c (charm) quarks: **LHCb**. The fourth is designed for the study of heavy-ion collisions: **ALICE** (A Large Ion Collider Experiment) investigating properties of nuclear matter at high temperature and density. There are also other interesting (smaller) experiments sited near the large ones:

– **TOTEM**: measures protons that escape down the CMS beam pipe, for the total cross-section measurement and diffractive production;
– **LHCf**: studies forward production of neutral particles, at the ATLAS IP;
– **MoEDAL**: searches for magnetic monopoles at the LHCb IP, using e.g. plastic sheets to detect

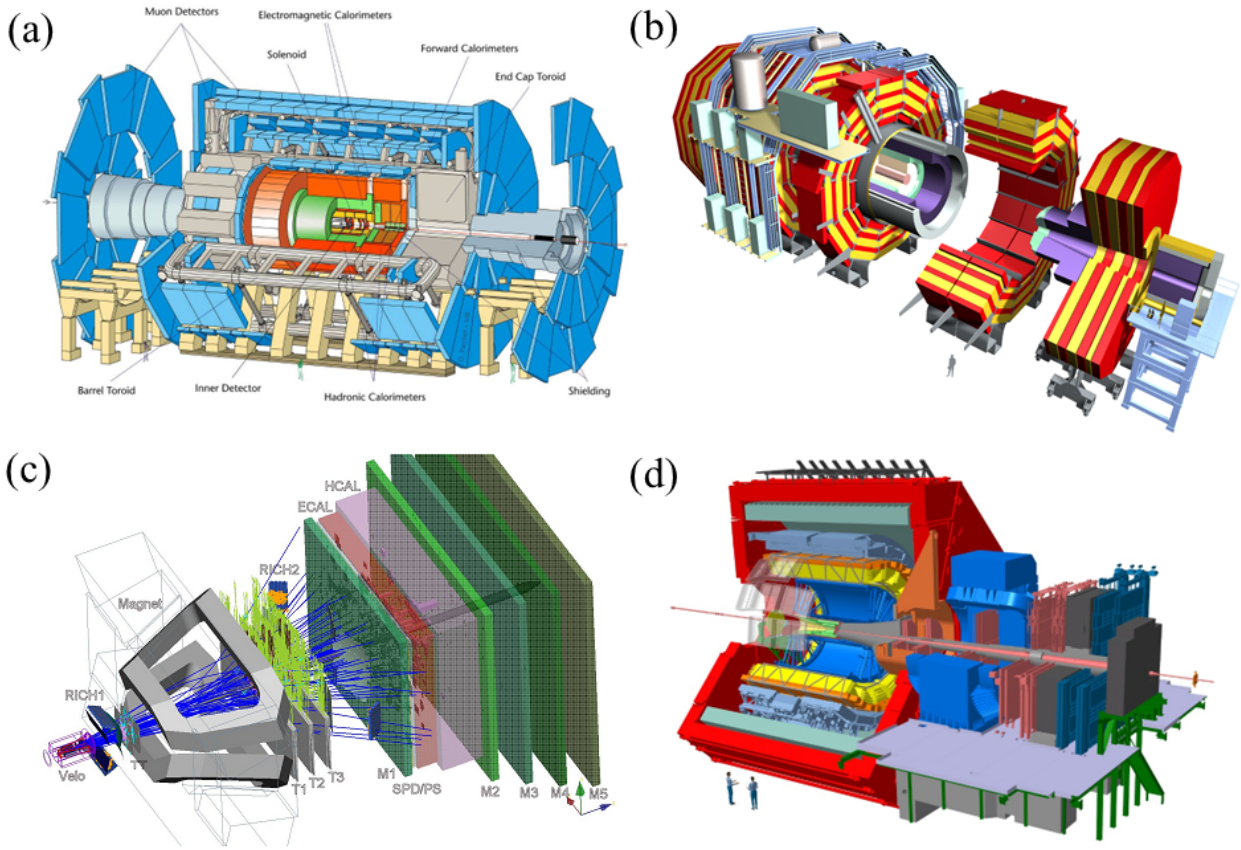

Fig. 16: The major LHC experiments: (a) ATLAS, (b) CMS, (c) LHCb, (d) ALICE.

highly ionizing tracks;

– **FASER** & **SND**: new experiments sited along the beam axis about 500 m either side of ATLAS, looking for penetrating particles, Dark Matter, or neutrinos.

1.5 Summary of the first lecture

The Standard Model is a remarkable theoretical framework that is consistent with essentially all particle physics measurements to date, but there are strong reasons why it cannot be the full description. Particle colliders are the best way to reach the highest possible energies in the laboratory, to study the structure of matter and confront it with theory. There are various types, including particle factories at the *intensity* frontier. The LHC is the highest-energy collider in the world, at the *energy* frontier: based at CERN, it was designed to provide proton collisions at a high enough energy (14 TeV) and high enough luminosity (over $10^{34}\,\mathrm{cm}^{-2}\mathrm{s}^{-1}$) to discover the Higgs boson and search for new particles. The experiments at the LHC have been designed to study the collisions and directly observe any new particles that are produced: two general-purpose (ATLAS, CMS) and two dedicated experiments (ALICE, LHCb), as well as five smaller experiments (TOTEM, LHCf, MoEDAL, FASER, SND), which will feature in the 3^{rd} and 4^{th} lectures. Meanwhile, the next lecture aims to explain why the big experiments look like they do, and how they detect particles.

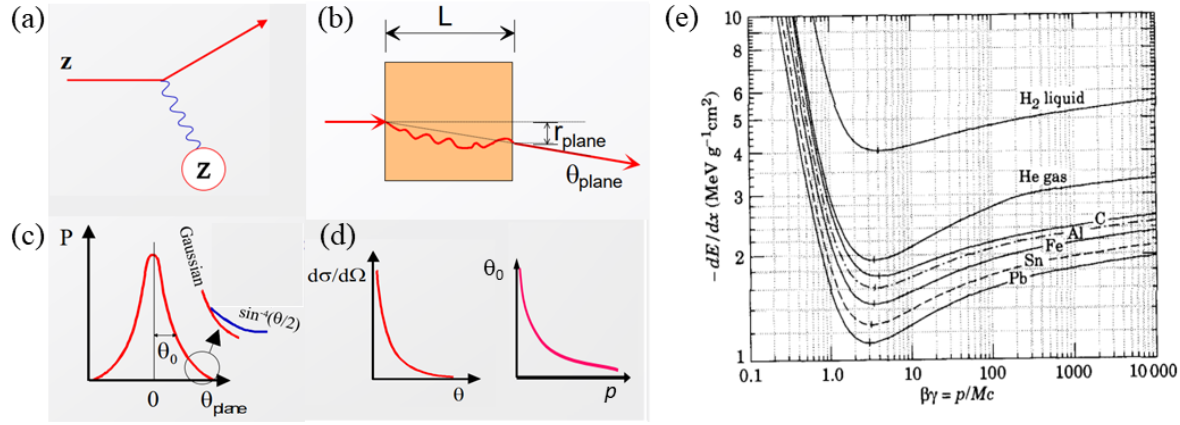

Fig. 17: Interaction of charged particles with matter [26]: (a) scattering off a nucleus; (b) multiple scattering in a layer of material; (c) the distribution of scattering angle; (d) functional dependence of the cross-section on the scattering angle, and the scattering distribution's width with momentum; (e) the dependence of ionization energy loss on $\beta\gamma$, for different materials [6].

2 Detectors & data

We wish to reconstruct as fully as possible the events where particles from the colliding beams have interacted, typically with many particles emerging from the interaction point. *Tracking* detectors determine whether the particles are charged, and (in conjunction with a magnetic field) measure the sign of the charge and the momentum of the particle. *Vertex* detectors are a subset of tracking detectors that are very precise, mounted close to the interaction point, to measure the vertex structure of the event: e.g. to see if there are short-lived decays. *Calorimeters* detect neutral particles, measure the energy of particles, and determine whether they have electromagnetic or hadronic interactions: typically with separate sub-detectors for the two interactions. *Particle identification* detectors determine what type of particles were produced: most experiments have muon detectors, and use information from their tracking detectors such as the amount of ionization. Others have dedicated sub-detectors for this, such as RICH detectors. These different detector types will be discussed in turn.[19]

Particles can only be detected if they deposit energy in the material of the detector. The cross-section as a function of solid-angle Ω for a particle with charge z to interact elastically with a target of nuclear charge Z, as illustrated in Fig. 17 (a), is given by the Rutherford formula [25]:

$$\frac{d\sigma}{d\Omega}(\theta) = 4zZr_{\mathrm{e}}^2 \left(\frac{m_{\mathrm{e}}c}{\beta p}\right)^2 \frac{1}{\sin^4 \theta/2} \quad , \tag{1}$$

where θ is the scattering angle of the particle and r_{e} is the classical radius of the electron. However, scattering does not lead to significant energy loss, since nuclei are heavy. In a sufficiently thick layer of material a particle will undergo multiple scattering, which is relevant to tracking, see Fig. 17 (b). The final distribution of scattering angle shown in Fig. 17 (c) is result of many random scatters, leading to a

[19] This is the most technically applied of the lectures: those of you studying theoretical physics can treat this as broadening your scientific culture, to understand how experiments actually work.

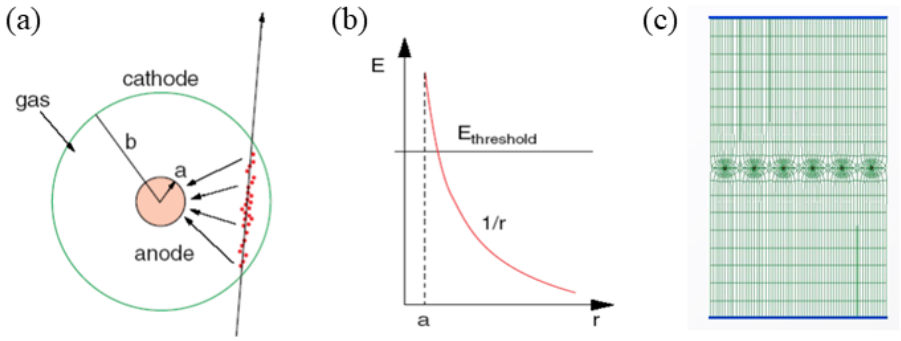

Fig. 18: (a) Cross-section through a wire chamber cell, showing the ionisation deposited by a charged particle passing through [27]; (b) the increasing electric field as the radius reduces, until the threshold for further ionization is passed; (c) an array of wires forming an MWPC.

Gaussian distribution (by the central limit theorem), with width:

$$\theta_0 \propto \frac{1}{p}\sqrt{\frac{L}{X_0}}\,, \tag{2}$$

where L is the length of the layer, and X_0 is the "radiation length", a property of the material. As indicated in Fig. 17 (c) there are non-Gaussian tails to the multiple-scattering distribution, due to occasional large scatters; also illustrated in Fig. 17 (d) are the dependence of the cross-section for scattering on θ, that is strongly forward peaked, and the width of the multiple-scattering distribution on momentum, that falls off like $1/p$.

Energy is deposited through discrete collisions with the atomic electrons of the absorber material (as noted above, collisions with nuclei are not important for energy loss), which leads to ionization. The Bethe-Bloch formula for energy loss by ionization, dE/dx, depends only on the velocity $\beta = v/c$ of the particle [6]:

$$\left\langle \frac{dE}{dx} \right\rangle = 4\pi\, N_{\rm A} r_e^2 m_e c^2 z^2 \frac{Z}{A}\frac{1}{\beta^2}\left[\frac{1}{2}\ln\frac{2m_e c^2\gamma^2\beta^2}{I^2}T^{\rm max} - \beta^2 - \frac{\delta}{2}\right] \quad , \tag{3}$$

where the relativistic boost $\gamma = E/m_0c^2 = 1/\sqrt{1-\beta^2}$, and details of the other parameters can be found in [6]. The resulting dependence of dE/dx on $\beta\gamma$ is plotted in Fig. 17 (e) for a variety of different materials. It is striking that the dependence is similar for most materials when plotted this way, except for the lightest ones (H_2 and He). In particular, there is an increase at low $\beta\gamma$, $\langle dE/dx\rangle \propto 1/\beta^2$ then the curve goes through a minimum for $\beta\gamma \approx 3$, referred to as "minimum ionizing particles" (MIP), before a gradual "relativistic rise" in the ionization loss at higher $\beta\gamma$.

2.1 Tracking detectors

A simple wire chamber is illustrated in Fig. 18: an anode wire is placed at high voltage (positive HV) in a gas volume, and electrons liberated by ionization in the gas drift towards the wire. The electrical field close to the wire is sufficiently high (above 10 kV/cm) for the drifting electrons to gain enough energy to ionize the gas further, leading to an avalanche: an exponential increase of number of electron-ion

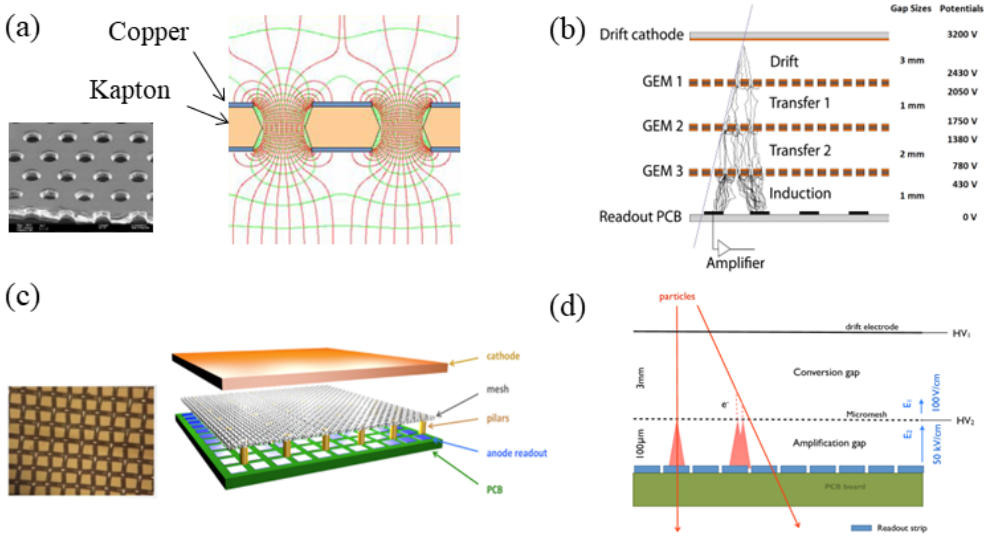

Fig. 19: Micropattern gas detectors [27]: (a) GEM, showing the perforated foil and the resulting field lines (b) GEM foils arranged in a stack to form a detector; (c) Micromegas, showing the wire grid and how it is arranged in the detector; (d) cross-section through a Micromegas chamber showing the signal formation.

pairs to several thousand, so that the signal becomes detectable with electronics. Simply repeating the cell using multiple wires gives the Multi-Wire Proportional Chamber (MWPC). "Drift chambers" are a variant where the time taken by the ionisation to reach the wire is measured, which allows the position of the incident particle to be determined more accurately.

Wires are not the only way to provide the accelerating field required. Modern versions of gaseous tracking detectors use Micro-Pattern Gas Detectors (MPGD): these allow higher precision, can operate at a higher rate and survive longer. Examples illustrated in Fig. 19 are the GEM (Gas Electron Multiplier) which uses holes in a foil for the accelerating structure; and Micromegas, which uses a fine wire mesh. The Time Projection Chamber (TPC) shown in Fig. 20 could be considered the "ultimate" gaseous detector: the detection planes (wire chambers or MPGDs) are moved to the end-plates and the ionization drifts across the full volume, with its arrival time measured to determine the longitudinal coordinate.

There are drawbacks of gaseous detectors: the charge drift is slow $\sim 3\,\mathrm{cm}/\mu\mathrm{s}$, so it can take tens of microseconds for the charge to reach the end-plate of a TPC, causing events to overlap in a high-rate environment. The small primary signal needs amplification, which can lead to ageing and rate limitations. They traditionally have limited spatial resolution ($\sim 100\,\mu$m), require massive frames to support the wire tension, and the supply of services such as HV and gas flow. Solid-state (usually silicon) trackers address some of those limitations, and are at the heart of many modern collider detectors, see Fig. 21 (a). They are required to be radiation hard, and have low mass (be thin) to minimize the multiple scattering of detected tracks.

Semiconductors such as silicon crystals are doped with impurities to alter their band structure (n or p-type, typically using phosphorus or boron, see Fig. 21 (b)). Features such as strips are implanted with different doping to the bulk material. Applying an external reverse voltage to a p-n junction depletes the bulk of free charges, as illustrated in Fig. 21 (c). Bringing two doped regions in contact leads to a

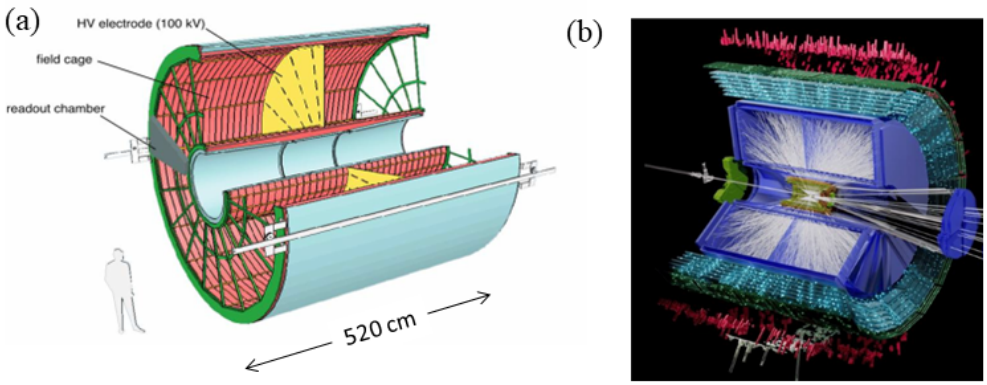

Fig. 20: (a) Cut-away view of the ALICE TPC; (b) display of an event taken in November 2022 showing a heavy-ion collision in the upgraded TPC, which uses GEMs for the readout chambers [28].

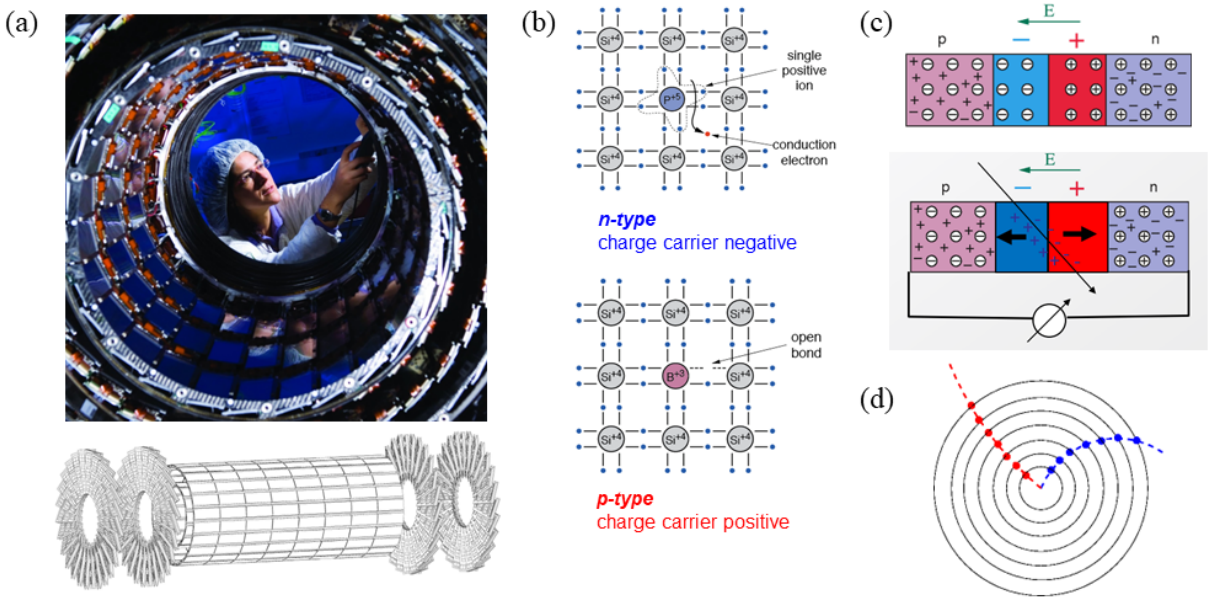

Fig. 21: (a) Silicon detectors arranged to form a tracker barrel, with (below) the many wafers tiling the CMS pixel barrel and endcap wheels; (b) the crystal structure of silicon, doped with phosphorus (above) and boron (below); (c) depletion layer that results when two doped silicon wafers are brought together (above) and the detection of a crossing charged particle (below); (d) how tracks are formed by "joining the dots" from hits on each layer of a silicon detector [22].

"depletion zone" with few free charges. The resulting electric field separates any newly created free charges, such as those from the ionisation of a passing charged particle, leading to a signal current that can be detected with low-noise electronics. The implants can be chosen to be microstrips with pitch $\sim 50\,\mu$m, providing an accurate measurement of one coordinate, see Fig. 22. The other coordinate can be measured with strips at a different angle, so that one knows that the track passed where the hit strips cross. At high occupancy this can lead to ambiguities, which can be countered by moving to pixel detectors. Trajectories are reconstructed from consecutive measurements as particles traverse layers of silicon sensors filling the detector volume, see Fig. 21 (d).

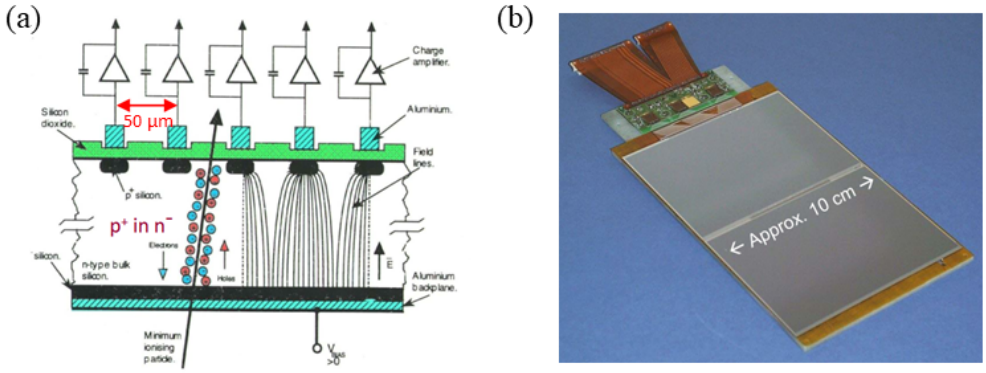

Fig. 22: (a) Cross-section through a silicon microstrip detector; (b) photograph of a typical microstrip detector, extended in length by wire-bonding two wafers [26].

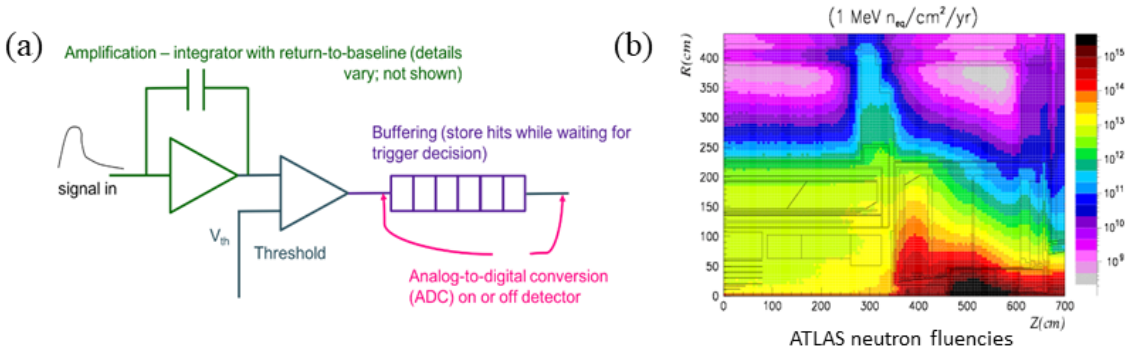

Fig. 23: (a) Typical layout of readout electronics [22]; (b) neutron fluencies around the ATLAS interaction point, where the beam axis is at the bottom of the plot [29].

The signals are readout via dedicated ASICs (Application-Specific Integrated Circuits). Pulses are small: 80 electron-hole pairs per mm $\times$ 150 mm-thick detector = 12,000 electrons = 2 fC. The readout electronics as sketched in Fig. 23 (a) can measure the time-over-threshold or just the presence of charge (binary). At the LHC bunch crossing rate of 40 MHz, the time between successive bunches is 25 ns. Fast electronics is therefore required, with a shaping time less than 25 ns to avoid overlapping events from the previous bunch crossing. The electronics also needs to be radiation resistant: the dose from pp collision products is high, especially in the forward region, as illustrated in Fig. 23 (b): $> 10^{15}\,\mathrm{n/cm^2}$ over 10 years, so deep sub-micron chip technology is used ($0.25\,\mu$m CMOS, or now even smaller feature sizes).

Experiments use a magnetic field to separate charges of particles and measure their momenta. The choice of magnet configuration determines the overall experiment layout. In a uniform magnetic field, charged particles follow circular trajectories in the transverse plane: $R = p_\mathrm{T}/0.3\,B$ using units [m], [GeV], [T], and in 3D the trajectories are helical, as shown in Fig. 24 (a). The tracks of charged particles are measured using particle detectors with given spatial precision $\sigma(x)$, and the p_T resolution:

$$\frac{\sigma(p_\mathrm{T})}{p_\mathrm{T}} \propto \frac{\sigma(x)\cdot p_\mathrm{T}}{B\,L^2} \quad . \tag{4}$$

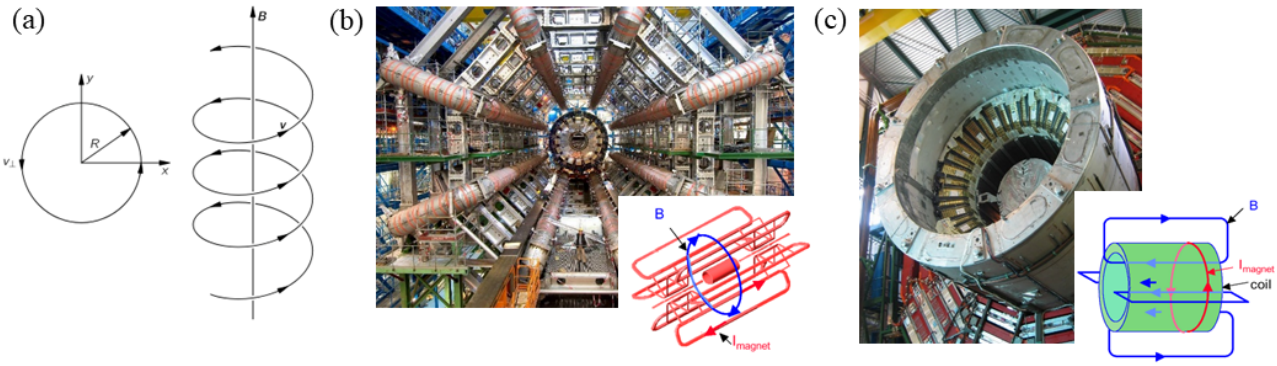

Fig. 24: (a) Effect of a magnetic field on a charged particle, in projection (left) and in 3D (right); (b) an iconic picture of the toroidal magnet of ATLAS, with (inset) the field configuration; (c) the solenoidal magnet of CMS with (inset) the field configuration [26].

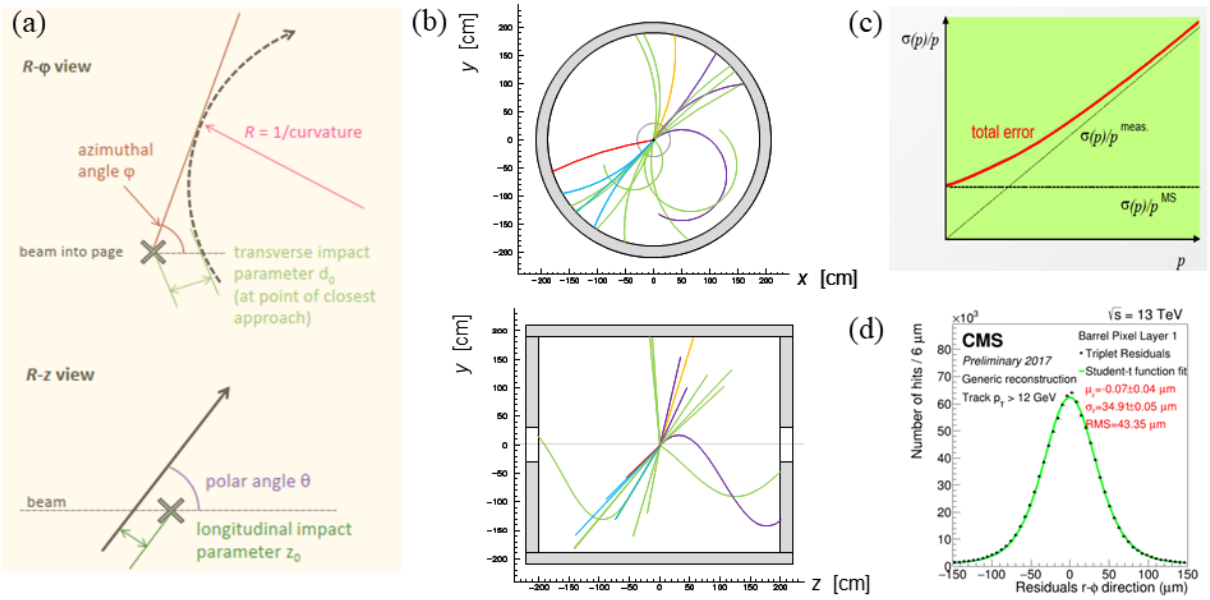

Fig. 25: (a) Definition of track parameters in the R-ϕ projection (above) and R-z projection (below) [22]; (b) display of tracks in a simulated Z decay in the same projections; (c) dependence of the tracking uncertainty on momentum; (d) plot of track residuals [31].

To measure to higher momentum, one needs to increase the field B or the length L that the track is measured over. General-purpose experiments at the LHC were designed to measure muons out to 1 TeV: they used the highest available field (superconducting magnets, up to 4 T) but still need to be very large, $L \sim \mathcal{O}(20\,\mathrm{m})$.

The type of magnet construction dominates their appearance. ATLAS has a toroidal field, illustrated in Fig. 24 (b): this has the advantages of being air cored and providing stand-alone muon measurement, but drawbacks of a tricky endcap configuraton and requiring an additional solenoid for central tracking. CMS has a more traditional solenoidal field, see Fig. 24 (c): with higher flux density (4 T) and allowing for a more compact layout, but at the cost of being very heavy (from the iron of the return

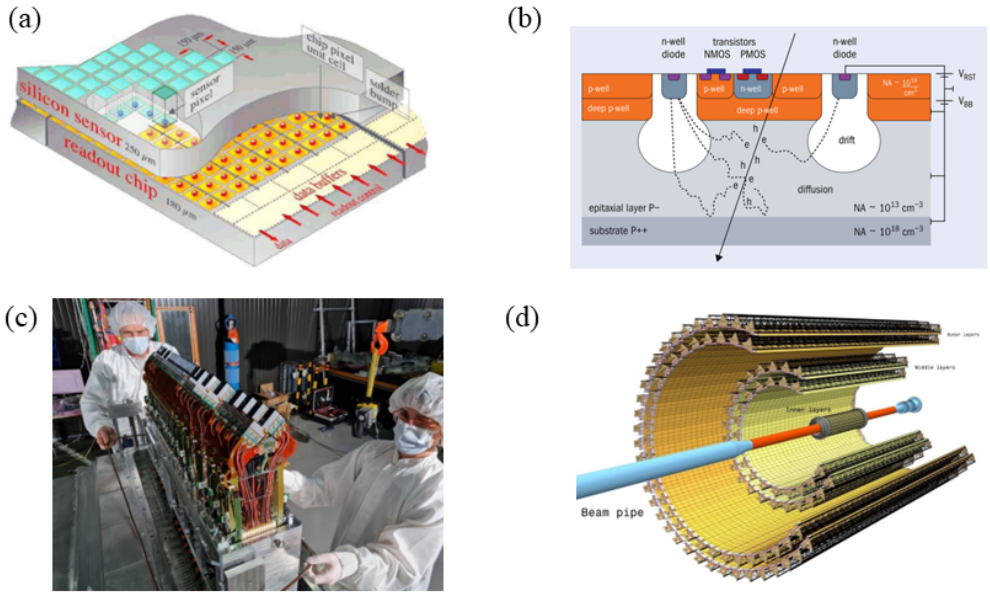

Fig. 26: (a) Cut-away view of a hybrid vertex detector [32]; (b) cross-section of a monolithic vertex detector [33]; (c) the LHCb VELO, where hybrid chips are visible as L-shaped elements for each layer, mounted in mechanics for retracting the detector half; (d) example of a monolithic vertex detector, the ALICE ITS.

yoke), and giving limited space for the calorimeter inside the coil. In projection, helical tracks give circular segments in (x, y),[20] or sinusoids in (y, z), which are almost straight lines for high p_{T} tracks in the longitudinal plane of the beam axis. A helical trajectory is defined by five track parameters: two impact parameters (d_0, z_0), two angles (θ, ϕ), and the track curvature $\propto q/p_{\mathrm{T}}$ for charge q, see Fig. 25.

The CMS tracker, illustrated in Fig. 21 (a), has 210 m^2 of silicon detectors! Thousands of wafers all have to be carefully aligned to each other e.g. using tracks that pass through overlap region between two adjacent wafers. Tracks are seeded with hits in the vertex detector, then a Kalman filter [30] is used for track extrapolation, with a subsequent fit to the helical trajectory. Recall $\sigma(p)/p \propto \sigma(x) \cdot p_{\mathrm{T}}$ from Eq. 4, and the multiple scattering contribution to the measurement error $\sigma(x) \propto \theta_0 \propto 1/p$ from Eq. 2, so the contribution to the momentum resolution from multiple scattering is constant vs momentum, as shown in Fig. 25 (c). The resolution can be determined by refitting the track after removing one of its hits, and comparing the "residual" distance between the hit and the refitted track—an example of a residual plot from the CMS tracker is shown in Fig. 25 (d). Generally it is harder to measure the curvature of straighter (higher-momentum) tracks, so the momentum resolution degrades at high momentum, and it is harder to extrapolate lower-momentum tracks: scattering in material matters, so the impact-parameter resolution is worse at low momentum.

Silicon pixel detectors are used for the precise vertex detectors. There are two major varieties, shown in Fig. 26: *hybrid* (with separate sensor and electronics chips) or *monolithic* (where the sensor and electronics are on the same silicon wafer). The LHCb VELO is an example of the first type, with $55\,\mu\mathrm{m} \times 55\,\mu\mathrm{m}$ pixels, bump-bonded to a readout chip. The sensors approach to a few mm from the LHC

[20] For Cartesian coordinates with the beam axis along z, y vertical, and x roughly horizontal to make up a right-handed system.

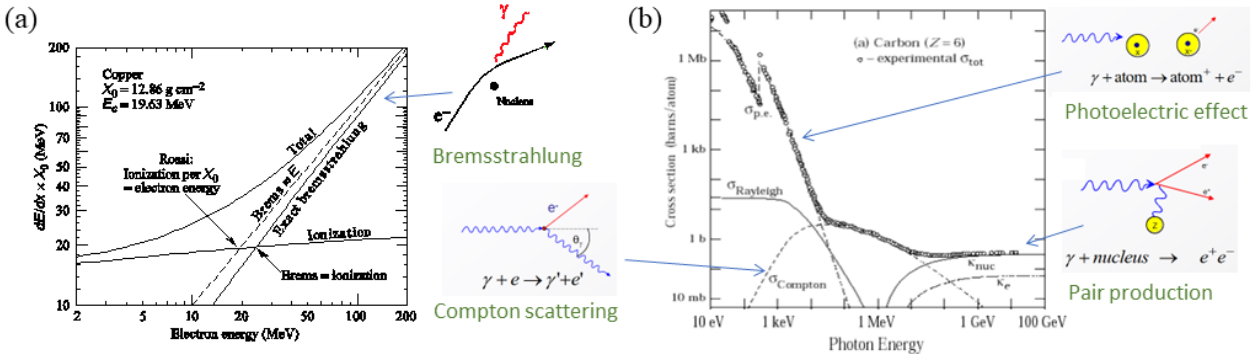

Fig. 27: Energy loss of (a) electrons and (b) photons passing through matter, as a function of energy, with the dominant processes highlighted [6, 26].

beams with a complex motorized system that is used to retract the detector while beams are injected. An incident with vacuum system occured in January 2023 leading to the RF foil that separates the detector from the LHC vacuum been deformed by about 1 cm—it will have to be replaced at end of the year. The ALPIDE chip of the ALICE ITS is an example of a monolithic vertex detector: each chip has $15 \times 30\,\mathrm{mm}^2$ area with over half a million pixels organised in 1024 columns and 512 rows. The sensitive volume is a 25 μm-thick layer of high-resistivity p-type silicon ($> 1\,\mathrm{k}\Omega\,\mathrm{cm}$) grown epitaxially on top of a standard CMOS wafer. It is radiation tolerance to beyond $10^{13}\,\mathrm{n/cm}^2$ (1 MeV equivalent), which is sufficient for the application in ALICE [33].

2.2 Calorimeters

Calorimeters measure energy: in a thermodynamics lab the temperature change of a known volume of water can be measured to determine the energy released in a reaction, sharing the reaction energy with many molecules evenly to determine its total. HEP calorimeters convert the energy of an incoming single particle into many lower-energy particles, and the number of particles can be counted to determine the total original energy. Basic properties of calorimeters include the use of dense material to cause particles to interact; the inclusion of active material to produce a measurable quantity: ionization charge or light; and they are thick, aiming to completely *contain* the energy in the detector. Calorimeters complement the magnetic spectrometers: they also measure the energy of *neutral* particles, and their energy resolution improves with energy while the track resolution degrades.

Electrons are stable particles and have low mass ($m_\mathrm{e} = 0.51\,\mathrm{MeV}$). When passing through matter they produce Bremsstrahlung radiation, and this effect scales with the radiation length X_0 of the material: seen earlier in the context of track scattering, it is the mean distance to reduce the energy by $1/e$,[21] see Fig. 27 (a). Photons interact with material via various processes, dominating at different energies, as shown in Fig. 27 (b)—at high energy they produce $\mathrm{e}^+\mathrm{e}^-$ pairs. Put those effects together at high energy: $1\gamma \rightarrow 2\mathrm{e} \rightarrow 2\gamma \rightarrow 4\mathrm{e}$..., leading to a shower of particles, as sketched in Fig. 28 (a). In this way *electromagnetic* calorimeters convert the energy of incoming particle into many lower-energy particles, until reaching the critical energy E_c at which showering stops. Eventually, the low-energy particles deposit their kinetic energy by ionizing or exciting the absorber. *Hadronic* calorimeters use showers

[21] e = base of natural logarithms ≈ 2.718.

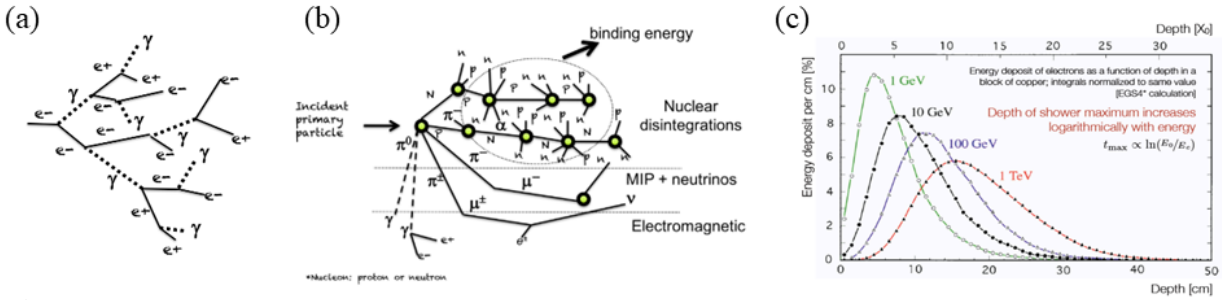

Fig. 28: (a) Electromagnetic shower from Bremsstrahlung and pair production; (b) contributions to a hadronic shower; (c) shower profiles vs depth in the calorimeter [22].

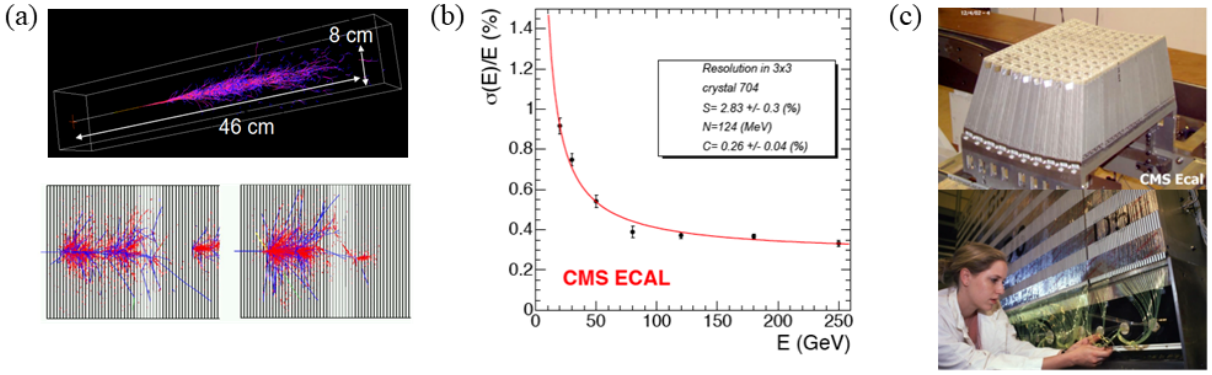

Fig. 29: (a) Simulation of an electromagnetic shower (above) and hadronic shower (below), where the less uniform energy deposition of the latter can be seen, the EM component shown in red comes from $\pi^0 \to \gamma\gamma$ decays; (b) energy resolution of the CMS ECAL; (c) crystals of the CMS ECAL (above) and construction of the ATLAS Tilecal (below) [34].

based on nuclear interactions, as sketched in Fig. 28 (b). The basic principle is to determine the total number of particles produced in the shower, which is proportional to the position of the peak of the energy deposit, as shown in Fig. 28 (c).

There are two major classes of calorimeter construction:

- **Homogeneous:** a single medium serves both as absorber and active detector. Plastic scintillators, glass or crystals produce light, that is read out by photodiodes or photomultipliers—they tend to be expensive.
- **Sampling:** reduce cost, by using layers of cheap, dense passive absorber (Pb, Cu, Fe) for the shower development alternated with active detector layers (silicon, scintillators or liquid argon) for signal measurement.

Scintillators are materials that convert ionization energy into light, typically by excitation of molecular energy levels.

Electromagnetic showers scale with the radiation length X_0 (= 1.8 cm for Fe, for example). Hadronic showers scale with the nuclear interaction length λ_I (= 17 cm for Fe). $\lambda_I \gg X_0$ so hadronic showers are longer, and hadron calorimeters are placed behind the electromagnetic ones (see Fig. 29 (a)).

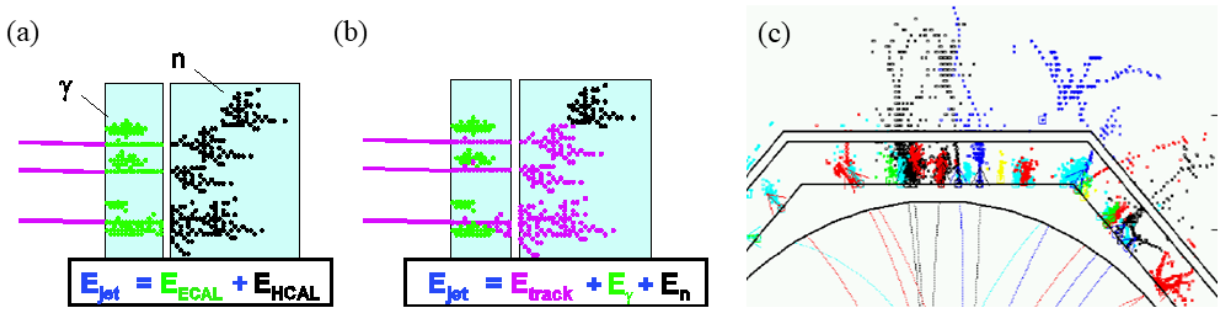

Fig. 30: (a) Traditional jet energy measurement in calorimeters; (b) the particle flow approach, using the more precise tracking information for charged showers; (c) simulation of an event in an e^+e^- Higgs Factory experiment, with deposits shown in the high-granularity calorimeters [35].

The general expression for the energy resolution of a calorimeter:

$$\frac{\sigma(E)}{E} = \frac{a}{\sqrt{E}} \oplus b \oplus \frac{c}{E} \quad , \tag{5}$$

where a is known as the "stochastic" term, coming from fluctuations in the number of signal processes; b is the constant term, due to inhomogeneities, bad cell inter-calibration, or non-linearities; and c is the "noise" term: due to electronic noise, radioactivity, or pileup. The transverse size of a shower is given by the Molière radius: $R_{\rm M} \approx (21\,{\rm MeV}/E_{\rm c})X_0$. The position of the shower maximum: $t_{\rm max} = (\ln E_0/E_{\rm c})\,X_0/\ln 2$ for EM calorimeters. As an example, for an incident particle with $E_0 = 100\,{\rm GeV}$ in lead glass, $E_{\rm c} = 11.8\,{\rm MeV}$, giving $t_{\rm max} \approx 13\,X_0$, $R_{\rm M} = 1.8 \cdot X_0 \approx 3.6\,{\rm cm}$.

Examples of electromagnetic calorimeters: CMS uses scintillating crystals ($PbWO_4$), giving very good energy resolution: $\sigma_E/E = 2.8\%/\sqrt{E} \oplus 0.3\% \oplus 0.128\,{\rm GeV}/E$, as shown in Fig. 29 (b), but with no longitudinal segmentation; ATLAS uses a sampling calorimeter: Pb plates embedded in liquid argon to collect the charge produced in showers: $\sigma_E/E \sim 10\%/\sqrt{E}$, but with the advantage of being very radiation hard. Due to their large size hadron calorimeters are usually sampling, to save cost. An example is the ATLAS Tilecal: iron plates interleaved with scintillator, see Fig. 29 (c). Wavelength shifting fibers trap the light via internal reflection and transport it to photon detectors that convert it into electrical signals: $\sigma_E/E \sim 50\%/\sqrt{E} \oplus 0.03$.

In general the hadronic component (h) of a hadron shower produces a smaller signal than the EM component (e) so $e/h > 1$. Compensating hadron calorimeters seek to restore $e/h = 1$ to achieve better resolution and linearity e.g. using ^{238}U as absorber, where its fission releases additional neutrons (as was done in ZEUS and L3); or dual readout with different fibres (scintillating/Cherenkov)—discussed for use in future colliders.

The *Particle Flow* technique is at borderline between tracking, calorimetry and particle ID. In a typical jet 60% of the energy comes from charged hadrons; 30% is from photons (mainly from π^0); and 10% is from neutral hadrons (n and K^0_L). The traditional approach to jet reconstruction is to measure all of the jet energy in the calorimeters, as shown in Fig. 30 (a), in which case $\sim 70\%$ of the energy is measured in the HCAL, and its relatively poor resolution limits the jet resolution: $\sigma_E/E \sim 60\%/\sqrt{E}$. In the Particle Flow approach charged particles are well measured in the tracker, photons in the ECAL, and

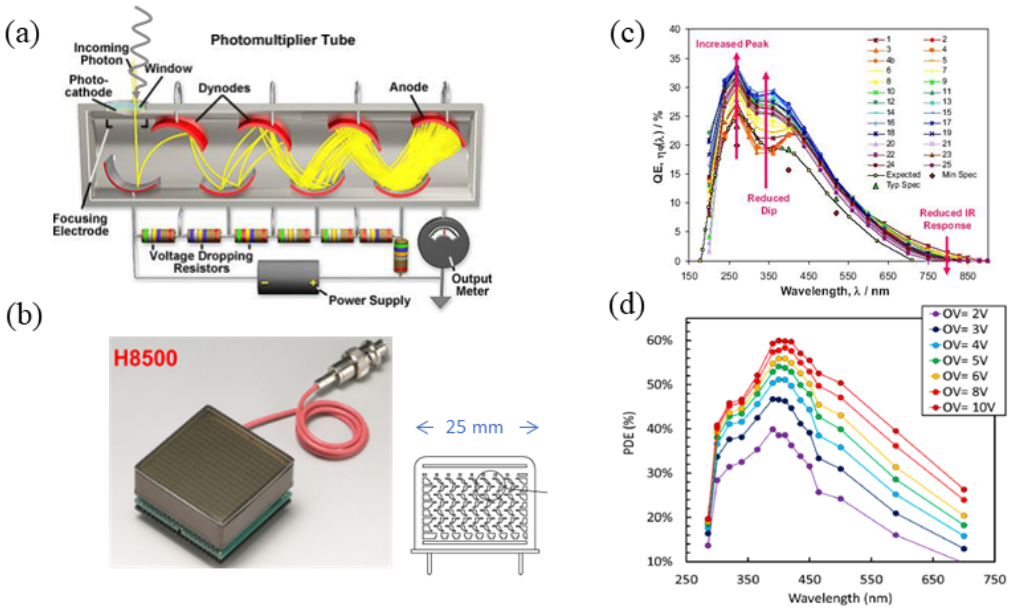

Fig. 31: (a) Schematic cross-section of a photomultimplier, showing the electron amplification at the dynodes [36]; (b) a multi-anode photomultiplier with (insert) its internal structure [37]; (c) quantum efficiency of a production series of vacuum photodetectors [38]; (d) photon detection efficiency of a SiPM for different values of one of the operating voltages, vs wavelength [39].

neutral hadrons (only) in the HCAL, as shown in Fig. 30 (b). As a result, only $\sim 10\%$ of the jet energy is taken from the HCAL, and $\sigma_E/E \sim 30\%/\sqrt{E}$ can be achieved. The main remaining contribution to the jet energy resolution comes from the confusion of contributions, from overlapping showers, etc. For the particle flow approach it is important to have high granularity calorimeters to help the (complicated) pattern recognition, as illustrated in Fig. 30 (c). This is the approach being studied for detectors at a future Higgs Factory, that I will return to in the 4^{th} lecture. A similar technology (Si-W) has been adopted for the CMS forward calorimeter upgrade (HGCAL) for HL-LHC—with 6 million channels.

Photon detection is necessary for many detectors performing calorimetry or particle identification. The requirements include high efficiency, good spatial granularity, and single-photon sensitivity (for RICH detectors). An incident photon is converted to an electron by the photoelectric effect in a photocathode, typically formed out of alkali metals e.g. Sb-Na-K-Cs. The photoelectron signal needs to be amplified to give a measurable electronic pulse. This is achieved in traditional photomultiplier (PM) by a dynode chain, with the charge multiplied at each dynode, as illustrated in Fig. 31 (a): e.g. if the number of electrons triples at each stage of a 12 dynode chain, the gain $= 3^{12} \sim 10^6$. The multianode PM is a marvel of miniaturization, with up to 64 pixels in a single tube, each $\sim 2 \times 2\,\text{mm}^2$; its dynodes are formed from a stack of metal foils, as shown in Fig. 31 (b). The quantum efficiency of a photocathode is the probability that an incident photon produces a photoelectron. Its peak value is typically 20–30%, as shown in Fig. 31 (c). This needs to be multiplied by the collection efficiency: the efficiency for detecting the photoelectron (which is typically 80–90%). The photocathode type is chosen according to the desired spectral sensitivity (mostly near to visible light with wavelength of a few hundred nm, i.e. $E_\gamma =$ a few eV).[22]

[22] Remember: $E = hc/\lambda$, $\lambda\,[\text{nm}] \approx 1240/E$ [eV].

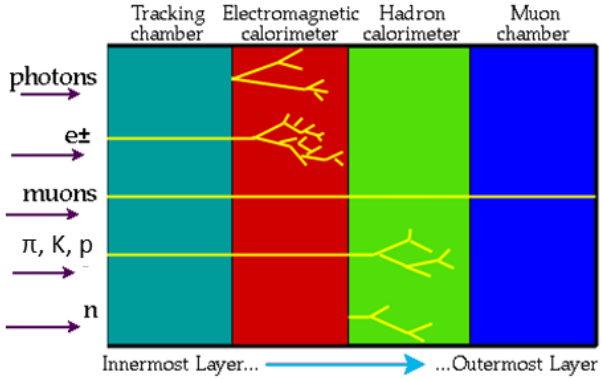

Fig. 32: The identification of different particle types in the layers of an experiment.

Other photon detectors have been developed that are faster than traditional photomultipliers. Time-of-flight detectors need fast timing precision at the picosecond (10^{-12} s) level; 1 ps $\approx$ 0.3 mm for a relativistic particle, so this requires small feature sizes. MCP (micro-channel plate) photon detectors use electron multiplication in small ($\sim 10\,\mu$m) glass pores, as used in image intensifiers, and a timing precision of ~ 10 ps is achieved. Fully solid-state photon detectors known as silicon PMs (SiPM) are a very active field of development: they use a p-n junction in Geiger mode (above the breakdown voltage), giving large gain, a binary signal, and long recovery time—an array of ~ 100 such elements are combined to make up a single pixel. Its advantages include being very compact, and having high photon detection efficiency (see Fig. 31 (d)); disadvantages include high noise, and susceptibility to neutron damage.

2.3 Particle identification

In an experiment, detectors are arranged in successive layers, moving out from the interaction point, as illustrated in Fig. 32. The tracking detectors are located closest to the beam pipe to minimize multiple scattering of tracks before they are measured, and they detect charged particles. They are followed by the electromagnetic calorimeter, where (e, γ) produce showers; then the hadronic calorimeter, where $(\pi, \mathrm{K}, \mathrm{p}, \mathrm{n})$ produce showers; and finally muon detectors. Neutrinos escape undetected, leading to missing energy. Enough information is provided by the combination of these detectors to separate all of the particle types, except the charged hadrons $(\pi, \mathrm{K}, \mathrm{p})$—for this, specialized detectors are required.

I will now briefly review how the different particle types are identified, returning to the event display that was shown in the 1$^{\mathrm{st}}$ lecture from the ALEPH experiment at LEP, where the different detectors can now be recognized. These "simple" events illustrate how different particle types can be identified, as shown in Fig. 33. Electrons and photons give similar showers in the ECAL, and are distinguished by the existence (or not) of an associated track. For electrons, E (energy in the ECAL) and p (momentum from the tracker) should be equal: $E/p = 1$—which is not the case for other particles.

Muons act like heavier versions of the electron, with mass 105.7 MeV. They decay to electrons, $\mu^- \to e^- \overline{\nu}_e \nu_\mu$, with (proper) lifetime $\tau_\mu = 2.2\,\mu$s, the mean of their exponential decay distribution. The distance they travel (on average) before they decay: $d = \beta\gamma c\tau_\mu$, where velocity $\beta = v/c$, boost $\gamma = E/m = 1/\sqrt{(1-\beta^2)}$. A 10 GeV muon flies ~ 60 km before decay $\gg$ detector size, and so they are effectively stable. Since the mass is large, Bremsstrahlung radiation is small, and as a lepton it

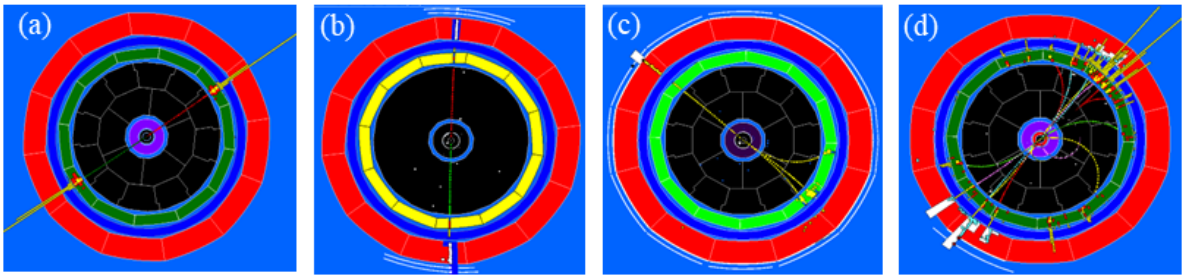

Fig. 33: Event displays of $e^+e^- \to Z \to f\overline{f}$ events, where the final state particles f are (a) electrons; (b) muons; (c) tau leptons; (d) quarks.

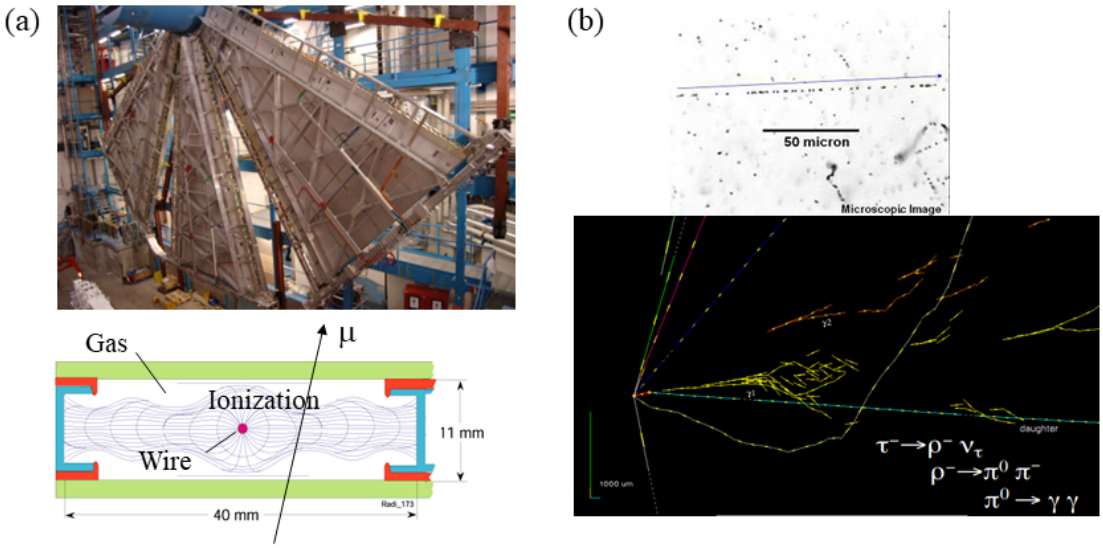

Fig. 34: (a) Muon chambers of the ATLAS end-cap (above), and a cross-section through a drift chamber from CMS (below); (b) track reconstruction in an emulsion detector after development, where the ionisation deposits are visible as microscopic dots (above), and display of an event in OPERA where a neutrino has produced a τ (below) [40].

does not feel the strong interaction, so they are the most penetrating charged particles. Since they are sited on the outside of an experiment, muon detectors tend to dominate their appearance, see Fig. 34 (a). Tracking for muons covers an area of $\sim 10{,}000\,\mathrm{m}^2$ in these LHC detectors! [23] They must be inexpensive, low granularity, but precise enough for momentum measurement, e.g. wire chambers with long drift volume.

The tau lepton is heavier still, $m_\tau = 1.78\,\mathrm{GeV}$. It is heavy enough that can decay to many final states: $\tau^- \to \mu^-\overline{\nu}_\mu\nu_\tau$, $\pi^-\nu_\tau$, $\pi^-\pi^0\nu_\tau$, $\pi^-\pi^-\pi^+\nu_\tau$, ... Its lifetime $\tau_\tau = 0.29\,\mathrm{ps}$, so a 10 GeV tau flies $\sim 0.5\,\mathrm{mm}$. This is typically too short to be seen *directly* in the detectors. Instead the decay products are seen: low multiplicity, "few prong" decays. Accurate vertex detectors can detect that they do not come exactly from the interaction point (i.e. measure their impact parameter).

Neutrinos are neutral (i.e. produce no track) and only feel the weak interaction, so they pass though matter easily. Their interaction length $\lambda_{\mathrm{int}} = A/(\rho\,\sigma\,N_{\mathrm{A}})$ [6], with cross-section $\sigma \sim 10^{-38}\,\mathrm{cm}^2 \times E$

[23] For more details see the lecture of George Mikenberg.

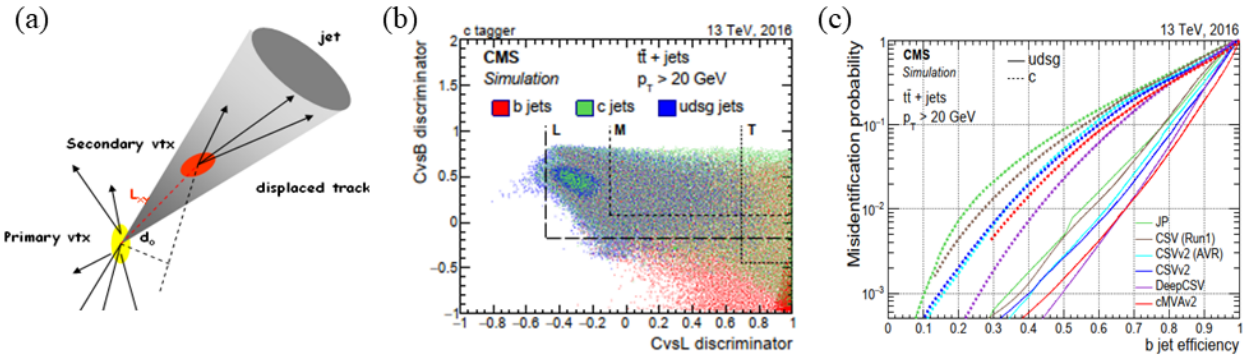

Fig. 35: (a) Reconstructing a b-quark decay by tagging offset tracks in a jet; (b) distribution of discriminating variables to select c vs b-quark or light-quark events, with the pattern expected from the different jets indicated by coloured points; (c) misidentification probability vs b-jet efficiency for a number of different tagging algorithms [41].

[GeV], so a 10 GeV neutrino can pass through over a million km of rock![24] Neutrinos are usually detected in HEP experiments through missing energy (applying energy conservation to rest of the event, in the transverse plane E_{T}). Nevertheless their interactions can be directly detected if you produce enough of them, and the detector is sufficiently massive. The neutrino flavour $(\nu_{\mathrm{e}}, \nu_{\mu}, \nu_{\tau})$ can be determined from their charged-current interaction: $\nu_{\mu} N \to \mu^{-} X$, etc. The OPERA experiment searched for ν_{τ} created by neutrino oscillation from a ν_{μ} beam (sent 730 km from CERN to LNGS in Italy), with an instrumented target mass of over 100 kton. The tau decays were seen as track kinks in a high precision emulsion detector, interleaved with lead sheets to provide the high mass of the target, see Fig. 34 (b).

Quarks feel the strong interaction, mediated by gluons. As discussed earlier, they are not seen (as bare partons) in the detector, due to the confinement property of QCD. Instead, they *hadronise* into hadrons—mostly mesons ($q\bar{q}$) or baryons (qqq). The lightest meson is the pion $\pi\,(\mathrm{u\bar{d}})$, the most abundant charged particle at the LHC. At high energy $\gg m_q$ the initial quark (or gluon) produces a "jet" of hadrons. Gluon and quark jets are difficult to distinguish: gluon jets tend to be wider, and have a softer particle spectrum. Jets are reconstructed by summing up the particles assigned to the jet. This is traditionally performed with a conical cut around the direction of a "seed" particle, or by iteratively adding up pairs of particles e.g. with lowest invariant mass. Different quark flavours can be separated (at least statistically) by looking for displaced tracks from b- and c-hadron decays ($\tau \sim 10^{-12}$ s), as illustrated in Fig. 35. The decay length $L = \gamma\beta c\tau \sim 1$ cm, leading to decay tracks being offset from the production vertex by $d_0 \sim 100\,\mu$m, so b-tagging requires precision vertexing. The jet properties can be used to approximate the quark or gluon. I will return to the discussion of jets in the next lecture.

Reconstructing particle decays

The sub-detectors of an experiment are designed to detect the products of the pp interactions, i.e. the "stable" charged particles $(\mathrm{e}, \mu, \pi, \mathrm{K}, \mathrm{p})$ and neutrals $(\gamma, \nu, \mathrm{n})$. "Stable" means that they live long enough to travel through the tracker.[25] These are then used to reconstruct the short-lived unstable particles, e.g.

[24] For more details see the lectures of Renata Zukanovich Funchal.
[25] Some π or K decay to $\mu\nu$ before reaching calorimeter, leading to a kink in the track.

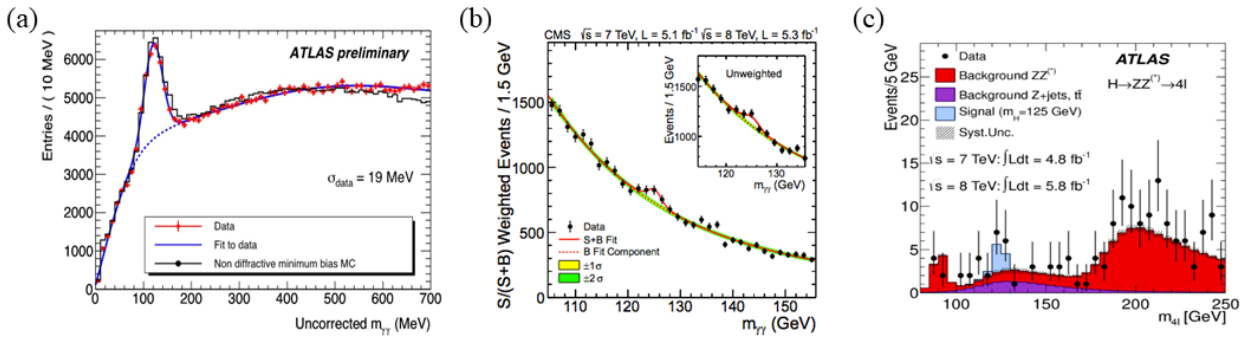

Fig. 36: Bump hunting: (a) $\pi^0 \to \gamma\gamma$ [42]; (b) $\mathrm{H} \to \gamma\gamma$ [43]; (c) $\mathrm{H} \to \mathrm{ZZ}^* \to 4\ell$ [44].

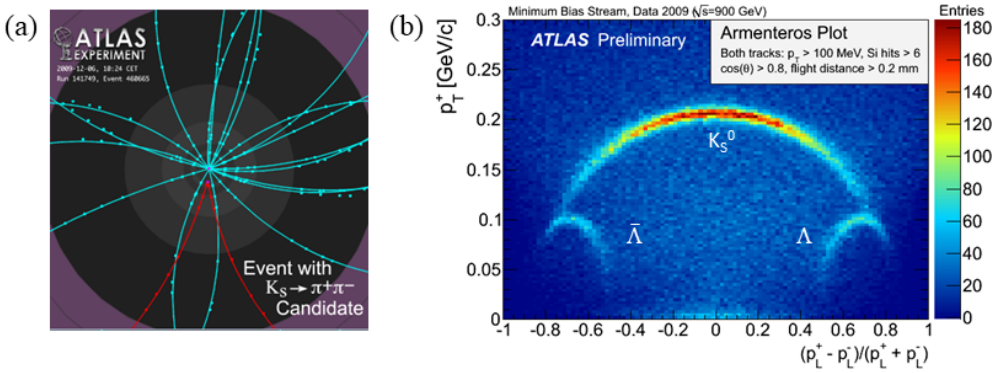

Fig. 37: (a) Event display with a V^0 in ATLAS (decay tracks in red); (b) reconstructing V^0 decays from the kinematic properties of the daughter tracks [42].

$\pi^0 \to \gamma\gamma$, $\rho^0 \to \pi^+\pi^-$, $\mathrm{K}^0_\mathrm{S} \to \pi^+\pi^-$, $\Lambda \to p\pi^-$, etc. From relativistic kinematics, the relation between energy E, momentum p, and (rest) mass m is: $E^2 = p^2 + m^2$. [26] The invariant mass of two particles from a decay is given by: $M^2 = m_1^2 + m_2^2 + 2(E_1E_2 - p_1p_2\cos\theta)$, so to reconstruct the parent mass M one needs precise knowledge of momenta and opening angle θ between the decay products, as well as their particle type, which determines their mass.

A typical example of the reconstruction of a particle decay is shown in Fig. 36 (a), for $\pi^0 \to \gamma\gamma$, one of the first (well-known) composite particles that was reconstructed in the LHC experiments, where $m(\pi^0) = 135\,\mathrm{MeV}$. This technique can also be used to search for more interesting signals, as shown in Fig. 36 (b), showing the first glimpse of the Higgs boson in the channel $\mathrm{H} \to \gamma\gamma$, at $m_\mathrm{H} = 125\,\mathrm{GeV}$, i.e. a mass about 1000 times higher than that of the π^0. The significance of a signal $S = N_\mathrm{S}/\sqrt{N_\mathrm{B}}$ (for high statistics, in a simplistic approach),[27] where N_S is the number of signal events and N_B the background events under the peak. If $S > 5$ then the signal is more than $5\times$ the error on the background, and one can claim discovery (the Gaussian probability that background fluctuates up by $> 5\,\sigma$ $\approx 10^{-7}$). This threshold was crossed for the Higgs boson search in July 2012, combining the $\gamma\gamma$ and ZZ^* decay mode (shown in Fig. 36 (c)). The announcement was made that "ATLAS and CMS observe a new particle compatible with the Higgs Boson". While the Noble prize went to Englert and Higgs (the two surviving initiators of the BEH mechanism), ATLAS and CMS received an honourable mention for the discovery, in the Nobel citation.

[26] The full expression is $E^2 = p^2c^2 + m^2c^4$, but factors of c are often dropped.
[27] For a more sophisticated treatment see the lectures of Harrison Prosper.

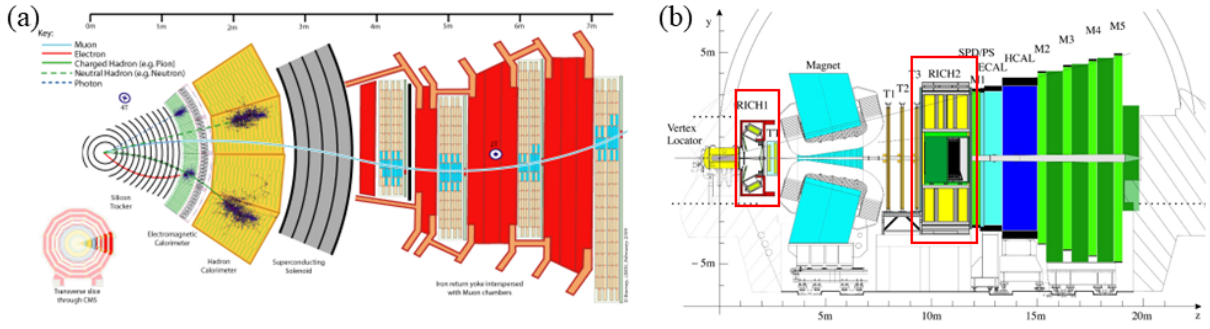

Fig. 38: (a) Slice through the detectors of a general-purpose experiment (CMS); (b) compare the layout of LHCb, where the additional sub-detectors (RICH) are highlighted.

Table 2: Hadrons that live long enough to be seen in the detector.

Particle	Mass $[\mathrm{MeV}/c^2]$	Quark content	Main decay	Lifetime	$c\tau$ [cm]
$\pi^{\pm}$	140	$\mathrm{u\bar{d}}$	$\mu\nu_\mu$	2.6×10^{-8} s	780
$\mathrm{K}^{\pm}$	494	$\mathrm{u\bar{s}}$	$\mu\nu_\mu$, $\pi\pi^0$	1.2×10^{-8} s	370
K^0_S	498	$\mathrm{d\bar{s}}$	$\pi\pi$	0.9×10^{-10} s	2.7
K^0_L	498	$\mathrm{d\bar{s}}$	$\pi\pi\pi$, $\pi\ell\nu$	5×10^{-8} s	1550
p	938	uud	stable	$> 10^{25}$ years	∞
n	940	udd	$\mathrm{pe}\nu_\mathrm{e}$	890 s	2.7×10^{13}
Λ	1116	uds	$\mathrm{p}\pi$	2.6×10^{-10} s	7.9

Hadron Identification

Instead of making do with jet reconstruction, sometimes the physics under study requires the identification of individual hadrons. There are *hundreds* of them, all listed in the PDG [6] (~ 1000 pages long). However, most are unstable and decay into a few longer-lived particles, listed in Table 2. Neutral hadrons K^0_S and Λ are collectively known as V^0s, due to their characteristic two-prong decay vertex, see Fig. 37. V^0s can be reconstructed from the kinematics of their positively and negatively charged decay products, without needing to identify the p or π. K^0_L and neutrons are detected as showers in the hadronic calorimeter without an associated charged track.

The set of sub-detectors used in a typical "general-purpose" experiment have now been discussed. One task that such detectors do not do very well is to identify different charged hadrons $(\pi, \mathrm{K}, \mathrm{p})$. This is the speciality of the dedicated experiments (LHCb and ALICE). LHCb is the dedicated detector for flavour physics at the LHC. It looks like a slice out of a general-purpose experiment, as shown in Fig. 38, apart from two extra detectors—for identifying charged hadrons. Production of high mass objects (like W, Z or Higgs bosons) requires a large momentum fraction x for each parton in the pp collision, leading to them being centrally produced. Hence the general-purpose experiments ATLAS & CMS are designed to cover the central rapidity region $|\eta| < 3$. B hadrons have a mass of ~ 5 GeV and therefore tend to be produced with asymmetric x values of the partons, leading to them being boosted along the beam direction, as seen in Fig. 39 (a). LHCb therefore covers the forward region $(2 < \eta < 5)$ with a single-

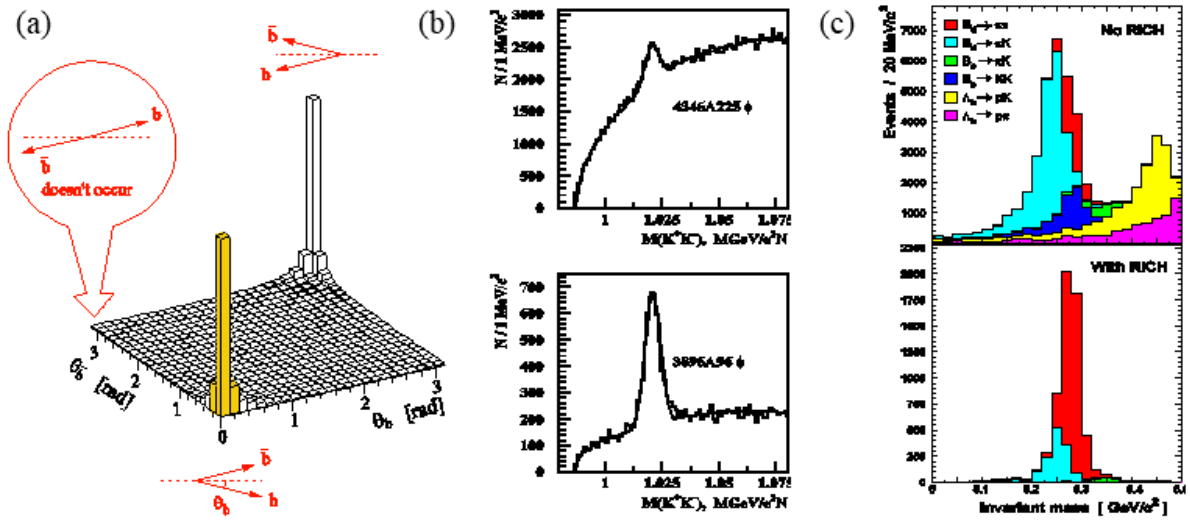

Fig. 39: (a) Correlation between production angle of b and $\overline{\mathrm{b}}$ quarks at the LHC: the acceptance of LHCb is shaded yellow; (b) improvement in signal to background ratio when using a RICH detector to select $\phi \to \mathrm{K}^+\mathrm{K}^-$ decays [45]; (c) importance of particle identification in separating two-body B decays, such as $\mathrm{B}^0 \to \pi^+\pi^-$ (shaded red), without use of RICH (above) and with RICH (below) [46].

arm spectrometer, and triggers on lower p_{T}. The charged hadrons $(\pi, \mathrm{K}, \mathrm{p})$ are all effectively stable, and have similar interactions, giving the same signature of a track and hadronic shower in the general-purpose experiments. However, identifying them can be crucial, in particular for the study of hadronic decays: e.g. $\phi \to \mathrm{K}^+\mathrm{K}^-$ shown in Fig. 39 (b). Making all two-track combinations in an event and calculating their invariant mass leads to a large combinatoric background (most tracks are pions, from other sources), while identifying the two tracks as kaons significantly improves the signal-to-background ratio. Flavour physics can help understand the matter-antimatter asymmetry: CP violation differentiates matter from antimatter, e.g: $\mathcal{B}(\mathrm{B}^0 \to \mathrm{K}^+\pi^-) > \mathcal{B}(\overline{\mathrm{B}}^0 \to \mathrm{K}^-\pi^+)$. Separating such two-body B decays requires charged hadron identification, as illustrated in Fig. 39 (c).

Since the interactions of charged hadrons are similar, the most direct way to distinguish them is to determine their (rest) mass. Their momentum is measured by the tracking system, so this is equivalent to determining their velocity, since $p = \gamma m v$, and hence $m = p/\gamma v = p/\gamma\beta c$. Four main processes are used, that depend on the velocity of a particle: [28]

1. Interaction with matter: recall that the main source of energy loss is via ionization ($\boldsymbol{dE/dx}$), that depends on velocity;
2. Perhaps the most direct method: measure the time-of-flight (**TOF**) of the particles over a fixed distance;
3. If the local speed of light changes compared to the velocity of the particle it will radiate photons, detected as **Transition Radiation**;
4. If a particle travels at greater than the local speed of light, it will radiate **Cherenkov Radiation**.

[28] These techniques all provide signals for charged leptons (e, μ) as well as $(\pi, \mathrm{K}, \mathrm{p})$. But $m_\mu \approx m_\pi$, so they are typically not well separated—dedicated muon detectors do a better job, and the EM calorimeter for electrons.

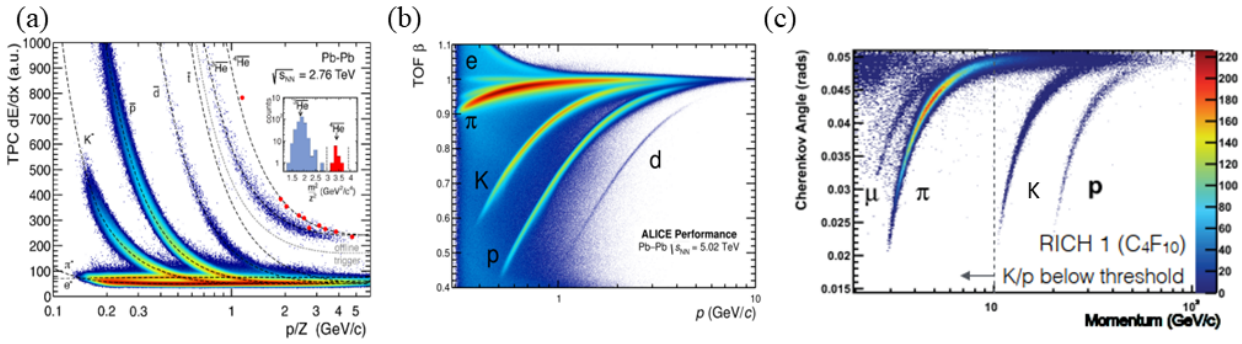

Fig. 40: Particle identification performance, from (a) dE/dx in the ALICE TPC; (b) time-of-flight in the ALICE TOF detector [47]; (c) Cherenkov radiation in the LHCb RICH1 [48].

Energy loss via ionization, dE/dx, is described by the Bethe-Bloch formula shown earlier in Eq. 3, with universal velocity dependence. This can be used to identify particles, particularly at low momentum where dE/dx varies rapidly, see Fig. 40 (a). The advantage of this technique is that it uses detectors needed anyway for tracking (but now requiring the accurate measurement of the charge deposited); disadvantages include that separation tends to be poor at high momentum, and the dE/dx curves cross over for different particle types.

Identification via time-of-flight is a simple concept: measure the time difference Δt between two detector planes separated by distance d, then $\beta = d/c\Delta t$. However, at high energy particle speeds are relativistic, closely approaching to c. At 10 GeV, the time for a K to travel 12 m is 40.05 ns, whereas for a π it would be 40.00 ns, so the difference is only 50 ps. Modern detectors and readout electronics have resolution $\sigma(t) \sim 10$ ns, fast enough for the LHC (bunch crossings 25 ns apart) but $\sigma(t) < 1$ ns is needed to do useful TOF: it can provide good ID at low momentum, but very precise timing is required for $p > 5$ GeV. The traditional approach is to use scintillator hodoscopes. ALICE uses Multi-gap RPCs with $\sigma(t) \approx 60$ ps, see Fig. 40 (b).

The local speed of light in a medium with refractive index n is $c_{\rm m} = c/n$. If a particle's relative velocity $v/c_{\rm m}$ changes, it will radiate photons:

- Change of direction v (in magnetic field) $\rightarrow$ **Synchrotron** radiation;
- Change of $|v|$ (passing through matter) $\rightarrow$ **Bremsstrahlung** radiation;
- Change of refractive index n of medium $\rightarrow$ **Transition** radiation.

Transition radiation is emitted whenever a relativistic charged particle traverses the border between two media with different dielectric constant ε ($n \sim \sqrt{\varepsilon}$). The energy emitted is proportional to the boost γ of the particle, so this is particularly useful for electron ID or for hadrons at high energy. The ATLAS Transition Radiation Tracker also acts as a central tracker, made up of $\sim$300,000 straw tubes.

From Special Relativity, nothing can go faster than the speed of light c in vacuum. However, due to the refractive index of a material, a particle can go faster than the *local* speed of light in the medium $c_{\rm m} = c/n$. This is analogous to the bow-wave of a boat travelling over water or the sonic boom of an airplane travelling faster than the speed of sound. The resulting Cherenkov light is produced

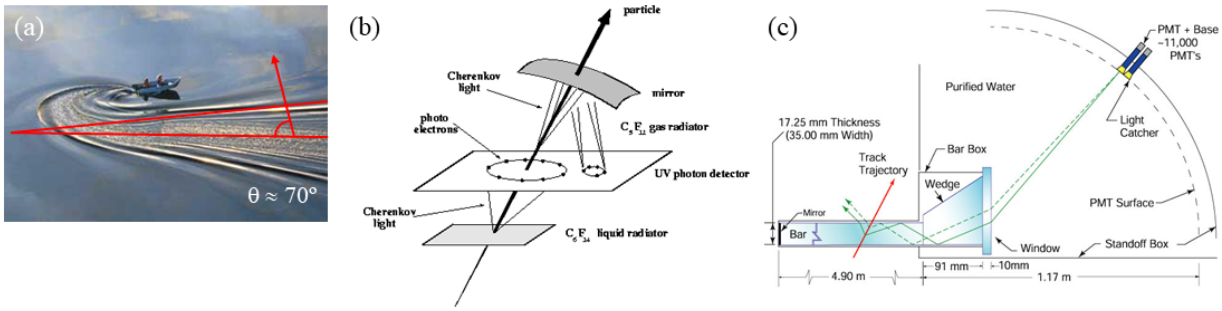

Fig. 41: (a) Bow-wave of a boat on a lake; (b) schematic design of a RICH detector [49]; (c) the DIRC detector of BaBar, where Cherenkov light is reflected within a quartz bar [50].

evenly distributed over photon energies, so when transformed to a wavelength distribution it peaks at low wavelengths—it is responsible for the bluish light that emerges from a nuclear reactor core. Consider a boat bobbing up and down on a lake, producing waves: while it moves slower than the waves, there is no coherent wave-front. If it moves faster than the waves, a coherent wave-front is formed, and as it increases in speed the angle θ of the wave-front changes, with $\cos\theta = v_{\rm wave}/v_{\rm boat}$. Using this construction, you can determine (roughly) the boat speed in Fig. 41 (a): $\theta = 70°$, $v_{\rm wave} = 2$ m/s on water, so $v_{\rm boat} = v_{\rm wave}/\cos\theta \approx 6$ m/s. Cherenkov light is produced when a charged particle ($v_{\rm boat} = \beta c$) goes faster than the speed of light ($v_{\rm wave} = c/n$), giving $\cos\theta_{\rm C} = 1/\beta n$, where $\theta_{\rm C}$ is the "Cherenkov angle". There is a threshold for light production at $\beta = 1/n$. The light is produced in three dimensions, so the wavefront forms a cone of light around the particle direction. By measuring the opening angle of the cone, the particle velocity can be determined.

In a Ring-Imaging Cherenkov (RICH) detector the Cherenkov light is focused onto a photodetector plane, usually with a spherical mirror, producing a ring image of single photons, illustrated in Fig. 41 (b). The LHCb RICH system combines the use of different gaseous radiator materials: fluorocarbons C_4F_{10} and CF_4 to cover different momentum ranges, see Fig. 40 (c). Alternative geometries have been developed for Cherenkov detectors using solid radiators: silica quartz (SiO_2) in the form of polished bars, or aerogel (the lightest solid in the world). They can result in much more compact detectors than gaseous RICH systems, and are suitable for the low momentum particles at a B Factory. Snell's law of refraction: $n_1 \sin\theta_1 = n_2 \sin\theta_2$, implies that for $n_1 = 1.45$ (quartz) and $n_2 \approx 1.0$ (air), total internal reflection will occur if $\theta_1 > \sin^{-1}(1/1.45) \approx 44°$; this is used to transport the Cherenkov light to photon detectors located at the end of a quartz bar, in a DIRC detector. Originally developed for BaBar (at SLAC) as shown in Fig. 41 (c), a similar technique is now used in the TOP detector of Belle II (KEK).

2.4 Data taking

The data produced as digital signals from the sub-detectors' readout electronics have to be collected and "built" into complete events: this is data acquisition, with typically ~ 1 MB/event. The data are stored for later "offline" analysis using computers: the speed of such storage is limited, so typically only ~ 1000 events/s can be recorded to storage, compared to interaction rate at LHC of $\sim 10^9$ events/s. Therefore $\sim 10^6$ events have to be rejected for each one stored, and this is implemented using a *trigger* system. 1 MB $\times$ 1 kHz $\times 10^7$ s (the canonical length associated to a year of collider operation) = 10^{10} MB/year i.e. 10 petabytes (PB) of data—which would fill around ten million CDs. The boundaries of trigger rate

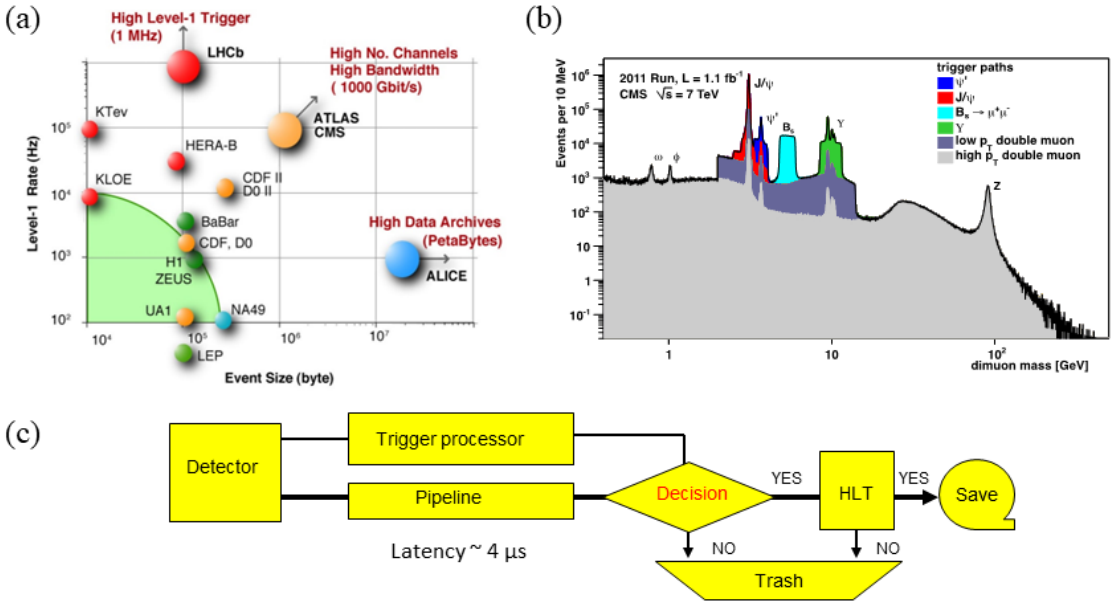

Fig. 42: (a) Plot of the Level-1 trigger rate vs event size, with the parameters of various experiments indicated [18]; (b) dimuon mass spectrum from CMS, showing the influence of the various trigger paths (coloured) used to select specific decays [51]; (c) flow diagram of data taken from a detector, passing through the trigger system.

and data volume are being pushed by the LHC experiments, as illustrated in Fig. 42 (a).[29]

Most interesting physics occurs at low rates compared to the 1 GHz input rate at the LHC (e.g. 10 Hz top quark production, and less than a Hz for searches). We want to keep most of the interesting events while rejecting others, keeping within the allowed bandwidth, see Fig. 42 (b). This is the role of the trigger. The selection is usually done in stages: Level-1: 1 GHz $\rightarrow$ 100 kHz; High-Level Trigger: 100 kHz $\rightarrow$ 1 kHz. The trigger decision takes a few μs $\gg$ 25 ns bunch crossing rate, so a massive amount of data is stored in electronic pipelines while special trigger processors perform calculations using part of the data, as illustrated in Fig. 42 (c). Events rejected by the trigger are lost forever, so one needs to take great care! Trigger thresholds are set on the electronic signals from detectors (e.g. ADC counts), and have to be calibrated in terms of efficiency versus the physics quantity of interest. A "menu" of many triggers run in parallel, finding a suitable compromise between efficiency and bandwidth. The first trigger level typically looks for signatures like high p_{T} leptons (e, μ) in dedicated electronics i.e. "hardware". Data are then read out to High-Level Triggers (HLT) for more complex selections, running on a dedicated CPU farm (with $\sim$ 1000 processors).

LHCb is now running *without* a hardware trigger: the full detector is readout at 40 MHz, and all triggering is done in software (HLT) in GPU and CPU farms, see Fig. 43. This is possible due to their relatively small event size, but is a trend for the future. It requires analysis done in real time to provide the alignment and calibration of the detectors. Reconstruction of the data involves pattern recognition (e.g. to find tracks from the hits) and fitting (e.g. to measure the momentum of a track), which takes a lot of computing power.

[29] Details are beyond the scope of these lectures.

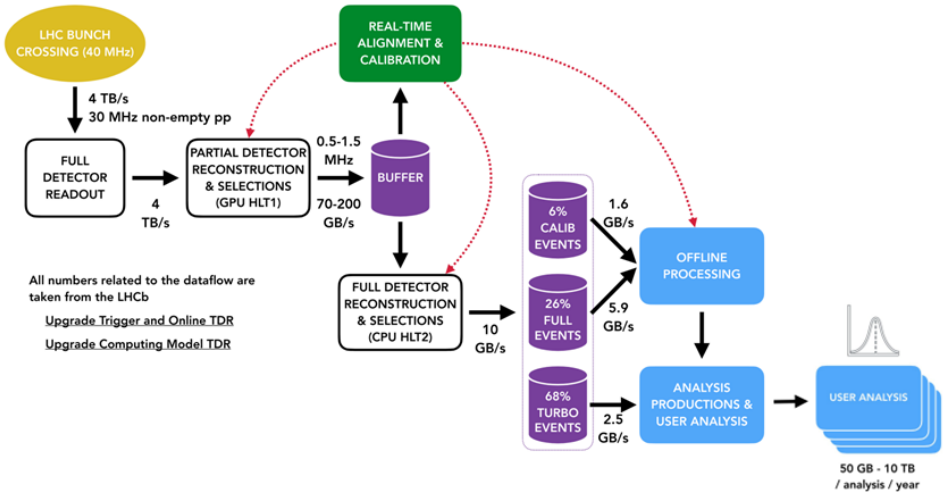

Fig. 43: The data flow for the "Real Time Analysis" approach of LHCb, where the triggering is performed entirely in software [52].

Simulated data are widely used to help design physics analyses, estimate efficiencies, emulate the trigger, compare results to theoretical expectations etc., see Fig. 44 (a). They can be treated in analysis like real events. Theoretical expressions are used for the underlying physics, with models for those features such as hadronization that cannot be calculated from first principles, and the Monte Carlo method (based on random numbers) for evaluating integrals. General-purpose event generators (e.g. HERWIG, PYTHIA, SHERPA): include $1 \to 2$, $2 \to 2$, and $2 \to 3$ fundamental processes, hadronization and the underlying event. Matrix Element generators (e.g. ALPGEN, MADGRAPH, MC@NLO) include expressions for multi-particle final states. In "Full" simulation, the passage of particles through the detector simulated in detail using the GEANT software package, which is time consuming, so "Fast" simulations are often developed where the detector response uses parameterized resolution.

User analysis relies on distributed computing and storage all over the world using the Worldwide LHC Computing Grid (WLCG), analysing reconstructed data, see Fig. 44 (b). The data evolves through various file-types during this process, from RAW data to "Data Summary Tape" (DST) or reduced-size mDST, nDST formats. The World Wide Web was invented at CERN, to help with data-intensive work. A large volume of data is transferred to computer centres around the world, requiring significant CPU power for their analysis, as illustrated in Fig. 44 (c, d).

2.5 Summary of the second lecture

Detector techniques used in the LHC experiments have been reviewed. The overall layout of detectors depends on the choice of magnetic field. Tracking detectors detect the ionization deposited by charged particles: traditionally using gas-based detectors, but more recently dominated by silicon. Along with the magnetic field, they determine charge and momentum. Calorimeters are important to measure the energy of particles, both charged and neutral. Particle identification is essential to reconstruct what happened in events: e.g. using muon detectors, energy loss and missing-energy signatures. Separating charged hadrons requires specialized detectors like the RICH. Modern experiments produce a mountain of data, like a multi-megapixel camera taking millions of photos a second. Triggering selects events of interest,

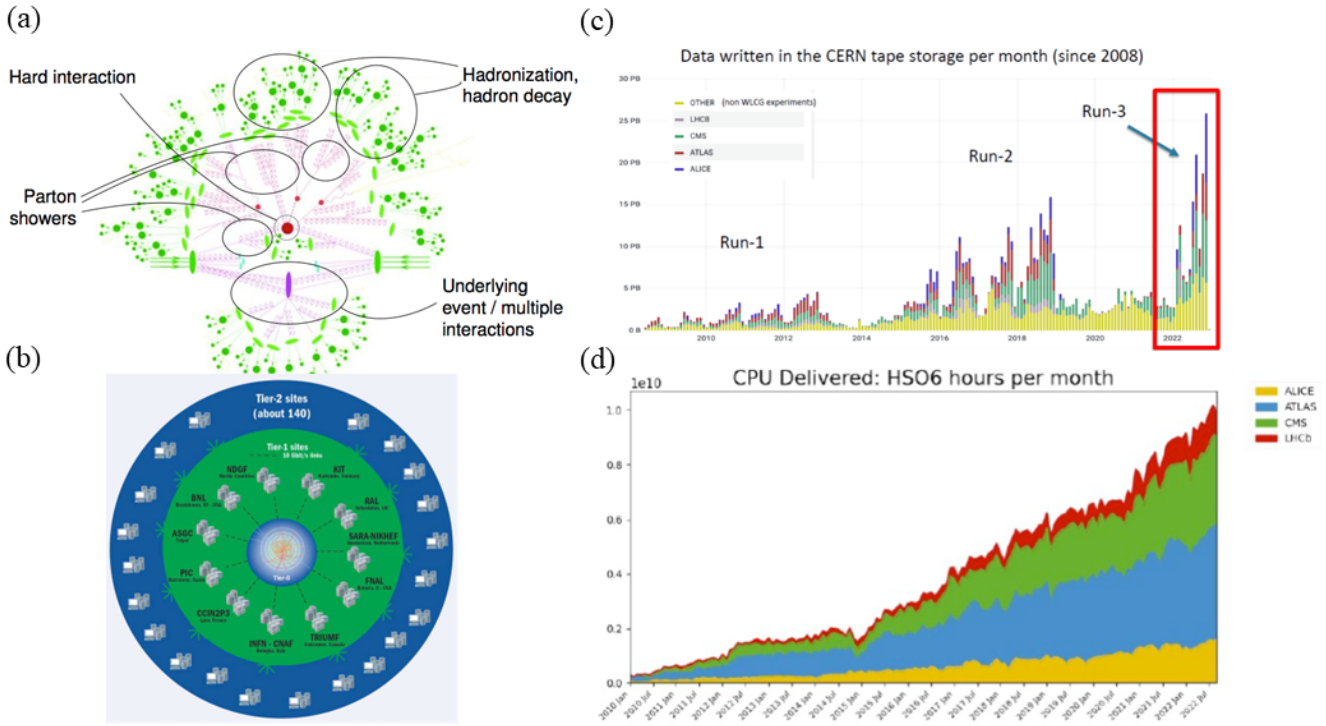

Fig. 44: (a) Ingredients for simulating an event at the LHC [22]; (b) schematic illustration of the tiered structure of distributing computing of the WLCG; (c) data recorded during the recent runs of the LHC; (d) integrated CPU power delivered to the LHC experiments through the WLCG, *vs* time [53].

data acquisition builds the full events and sends them to storage, and offline computing is used to analyze them. In the next lecture, selected physics highlights from the analysis of all this data from the LHC experiments will be presented (including the latest knowledge of the Higgs boson).

3 LHC physics highlights

It is only possible to include a limited selection of highlights, so I have selected them according to my personal taste—many more results are available from the websites of the experiments: e.g. for ATLAS [42], CMS [54], LHCb [46], and ALICE [55]. Proton-proton collisions at high energy in the LHC enable a wide variety of physics processes to be studied. Cross-sections (measuring probability of a given final state being produced) vary over 12 orders of magnitude (!) as was shown earlier in Fig. 12 (c). This enables a rich physics programme, and makes model-independent searches possible. But the collision rate is overwhelmed by mundane processes, so background discrimination and modelling are crucial. In this lecture I will go "down the SM ladder" of the processes in order of roughly decreasing cross-section, as sketched in Fig. 45.

First a few words on how cross-sections are measured:

$$\sigma = \frac{N_{\text{obs}} - N_{\text{bkg}}}{\varepsilon \cdot \int \mathcal{L}\, dt} \quad , \tag{6}$$

where N_{obs} is the number of observed candidates (fitted or counted), N_{bkg} is the number of background candidates (measured from data or calculated from theory), ε is the efficiency/acceptance, and $\mathcal{L}$ is the

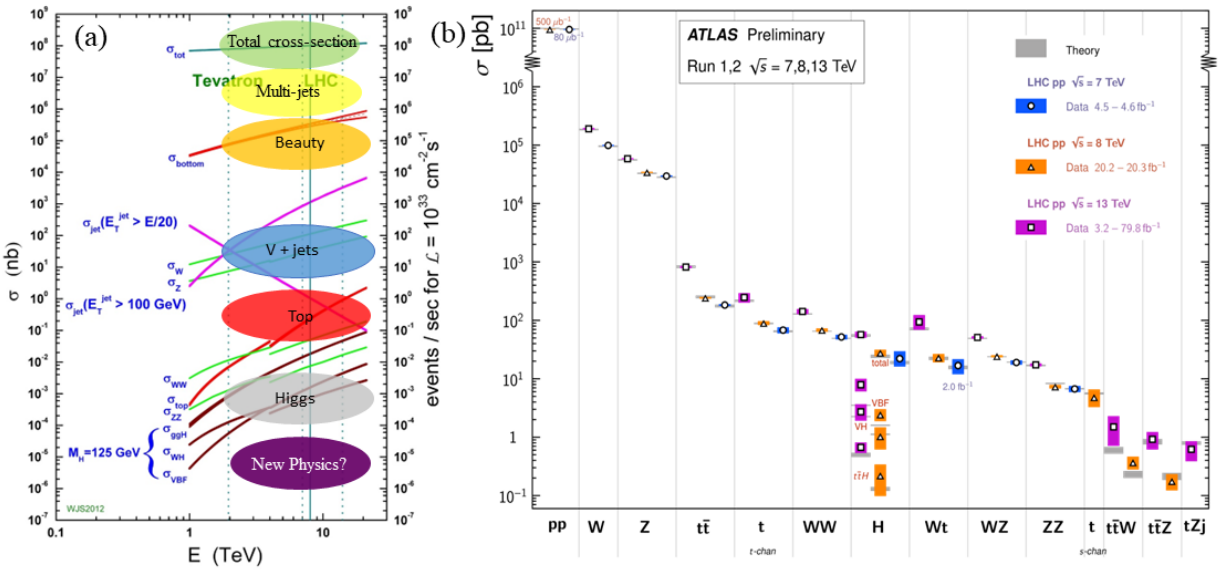

Fig. 45: (a) The cross-section of different selected physics processes at the LHC, discussed in the text; (b) measured cross-sections compared to the predictions from the Standard Model [56].

luminosity. The relative uncertainty on the cross-section is given by [22]:

$$\left(\frac{\delta\sigma}{\sigma}\right)^2 = \frac{\delta N_{\text{obs}}^2 + \delta N_{\text{bkg}}^2}{(N_{\text{obs}} - N_{\text{bkg}})^2} + \left(\frac{\delta\mathcal{L}}{\mathcal{L}}\right)^2 + \left(\frac{\delta\varepsilon}{\varepsilon}\right)^2 \quad . \tag{7}$$

"Errors" quoted for measurements are the uncertainties on their central value: either statistical from the fit to the data, quoted as $\pm 1\,\sigma$ (RMS), that scale with $1/\sqrt{N}$; or systematic from uncertainties in the other parameters that affect the result, such as the luminosity—estimating the latter is a difficult art.[30] Care is needed when measuring differential cross-sections: resolution effects can bias distributions, particularly when they have a steeply falling shape.

Measuring cross-sections requires knowledge of the *integrated* luminosity. The instantaneous luminosity can be determined via manipulating the beams in a special run, known as a van de Meer scan: the offset between the two counter-rotating beam positions is adjusted in steps to determine the beam profile, as shown in Fig. 46 (a), and the bunch charges are measured. That information needs to be transferred via signals in other detectors, so that the luminosity can be monitored throughout the run; $\sim 1\%$ precision has been achieved in this way on the luminosity measurement in the LHC experiments. The profiles of the beams can also be seen in beam–gas collisions, e.g. using the LHCb VELO, see Fig. 46 (b). The luminosity delivered can be levelled by adjusting the beam offset, e.g. to limit pileup or to provide lower luminosity for LHCb or ALICE—those experiments can then run simultaneously with ATLAS and CMS, but at different luminosities according to their needs.

The main challenge for most measurements is background, events from other processes which look like signal events: instrumental (fake) background in the detector, where a different type of object fakes the one present in the signal decay, or physics (irreducible) background, a different physics process with same final state as the signal. One approach for estimating the background contribution to the signal

[30] For more details see the lectures of Harrison Prosper.

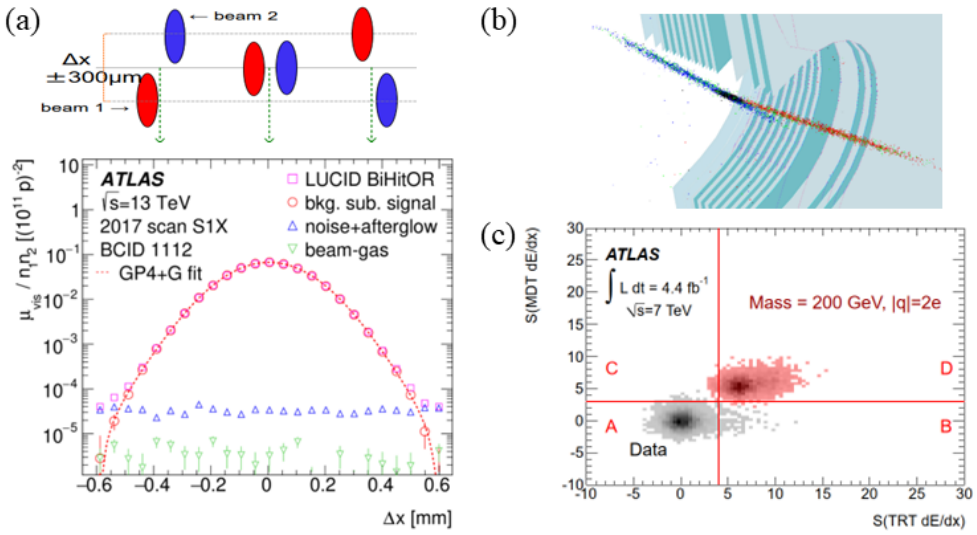

Fig. 46: (a) Measurement of the luminosity in a van de Meer scan, showing the offset of the two beams (indicated by red and blue bunches, above) and the corresponding variation in event rate as a function of the offset (below) [57]; (b) reconstructed vertices of beam-gas interactions in the LHCb VELO, shown in 3D—the vertices from the two counter-rotating beams are indicated in red and blue respectively [58]; (d) estimation of background using the ABCD method, where the grey points show the distribution of data and the red points the expectation from a simulated signal, in the plane of two selection cuts [59].

region is the so-called "ABCD" method illustrated in Fig. 46 (c): regions are defined by dividing the plane of two selection variables using cuts; region D is defined as the signal region, A, B and C as control regions. The expected number of candidates from the background in the signal region D is estimated from the numbers of observed data candidates in the other regions: $N^{\mathrm{D}}_{\mathrm{data}} = (N^{\mathrm{B}}_{\mathrm{data}} \times N^{\mathrm{C}}_{\mathrm{data}})/N^{\mathrm{A}}_{\mathrm{data}}$.

3.1 Strong interactions

Hadron collisions are swamped by multi-jet processes. To discover new physics, we need a quantitative understanding of QCD processes in rate and shape. In itself, the study of multi-jet final states is a test of perturbative QCD, and it can also serve as a window to new physics such as compositeness or excited quarks. Only small datasets are needed, as statistics are not a problem.

Let me first discuss the *total* cross-section. This is a very basic measurement: the total interaction probability when two protons hit each other. One can make use of the Optical Theorem from quantum mechanics: that the imaginary part of the amplitude between states a and b is given by the product of the amplitudes from a and b to all available intermediate states f, integrated over their phase space, as shown graphically in Fig. 47 (a). The total cross-section is equal to the imaginary part of the forward scattering amplitude, $\sigma_{\mathrm{tot}} \propto 4\pi\,\Im(f_{\mathrm{el}})_{t\to 0}$. This requires measurement of the differential elastic cross-section as a function of the Mandelstam variable t [3]:

$$\sigma^2_{\mathrm{tot}} = \frac{1}{L}\frac{16\pi}{1+\rho^2}\frac{dN_{\mathrm{el}}}{dt}\bigg|_{t\to 0}, \quad \text{where } \rho = \frac{\Re(f_{\mathrm{el}})}{\Im(f_{\mathrm{el}})}\bigg|_{t\to 0} \tag{8}$$

is taken from model extrapolation. Elastically scattered protons will escape from the general-purpose experiments inside the beam-pipe, so a dedicated "forward physics" detector is required, such as TOTEM

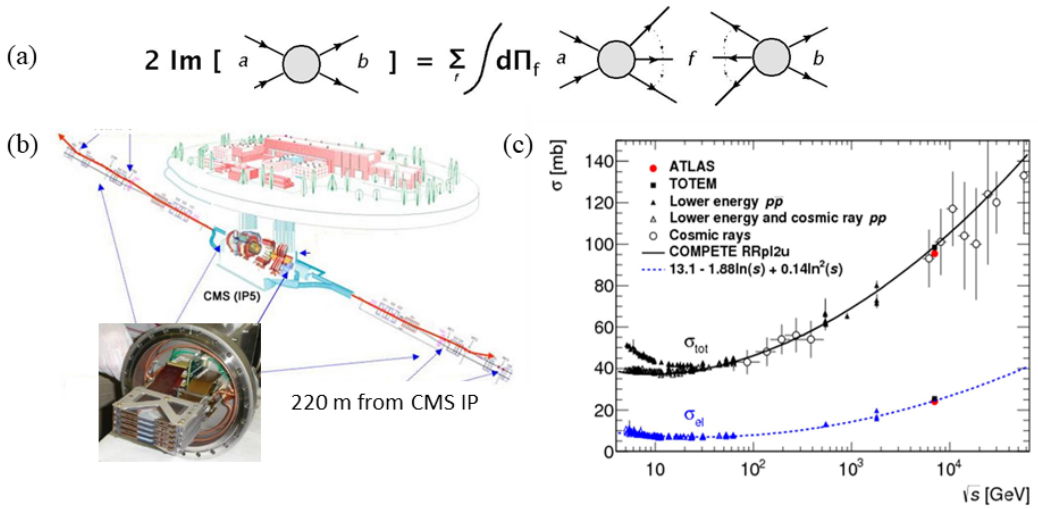

Fig. 47: (a) Graphical illustration of the Optical Theorem, relating the total cross-section to the forward scattering amplitude; (b) photograph of one of the tracking detectors of TOTEM, and their location along the beam-line near to CMS; (c) measurements of the total and elastic cross-sections vs centre-of-mass energy, showing the recent results from ATLAS and TOTEM [60].

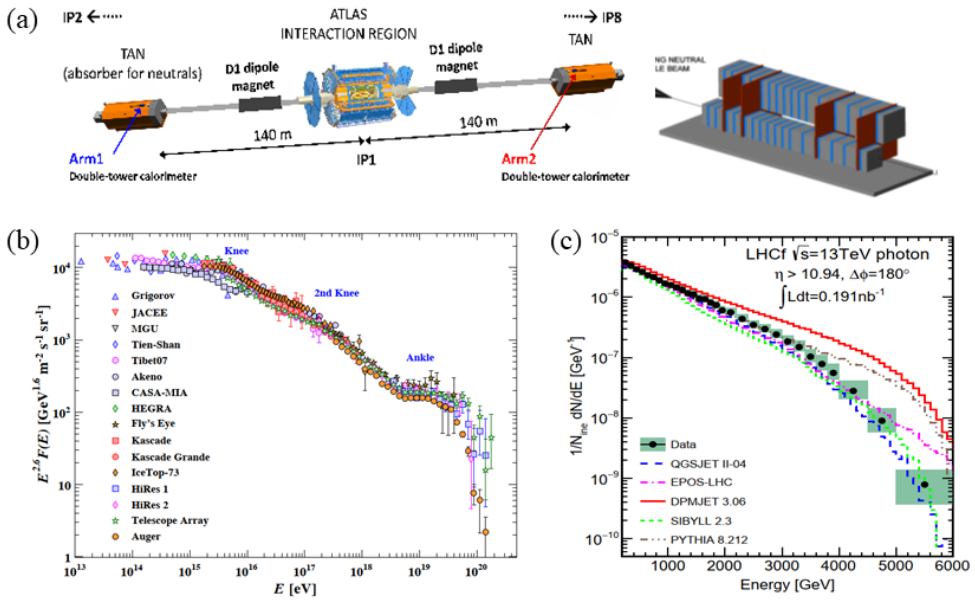

Fig. 48: (a) Schematic view of the LHCf calorimeters, and location along the beam-line near ATLAS; (b) energy spectrum of cosmic rays [6]; (c) photon spectrum in LHCf, compared to models [61].

shown in Fig. 47 (b). Silicon tracking detectors are mounted in "Roman Pots" very close to the beam to measure elastically scattered protons (retractable during beam manipulation, following a similar principle to the LHCb VELO). The result is shown in Fig. 47 (c), in agreement with the expectation.

Another forward-physics experiment is LHCf, close to the ATLAS IP, using a zero-degree calorimeter to study neutral production relevant to cosmic rays. 13 TeV pp collisions correspond to 10^{17} eV cosmic rays impinging on the atmosphere (i.e. undergoing fixed-target collisions), above the "knee" in the CR spectrum (see Fig. 48). LHCf data helps tune the simulation of CR air showers.[31]

[31] For more details see the lecture of Miguel Mostafa.

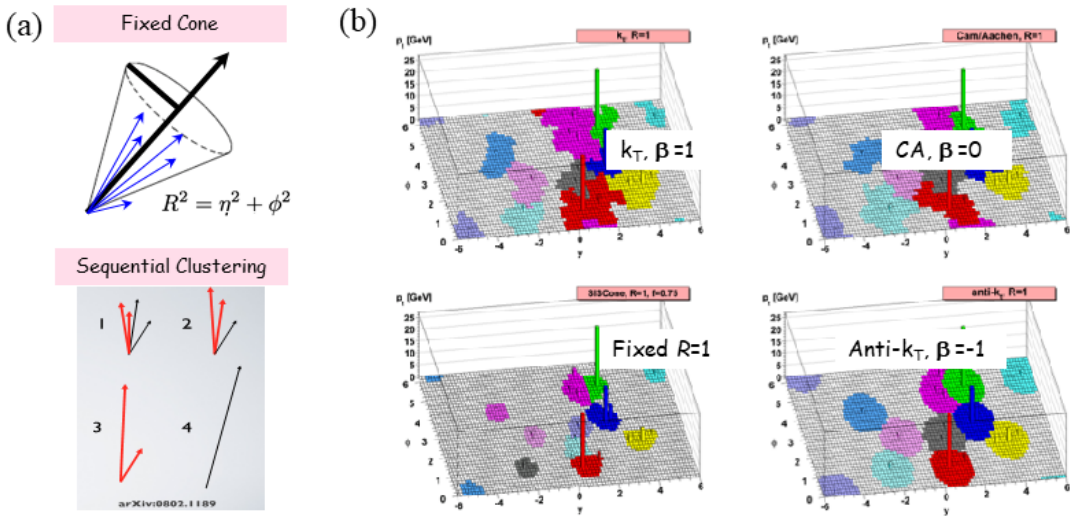

Fig. 49: (a) Illustration of jet-finding algroithms, using a fixed cone (above) or sequential clustering (below); (b) application of the different algorithms discussed in the text to the same parton-level event, showing the different jet boundaries found (coloured) in the space of azimuthal angle vs rapidity [62].

Jet measurements

Jets are collimated sprays of stable charged and neutral particles, as introduced earlier. They can be reconstructed using different algorithms, illustrated in Fig. 49:

- **Fixed Cone:** with variations in the choice of seed and cone size ($R = 0.3$ ... 1);
- **Sequential Clustering:** pairwise examination of input 4-vectors; merging is determined by proximity in space and transverse momentum between particles i, j and the beam-axis b. Defining $d_{ij} = \min(p_{\mathrm{T}i}^{2\beta}, p_{\mathrm{T}j}^{2\beta})\,\Delta R_{ij}^2/R^2$ and $d_{ib} = p_{\mathrm{T}i}^{2\beta}$, if $d_{ij} < d_{ib}$ the particles are combined, otherwise i is taken as a jet. The exponent β takes different values for different variants of the algorithm: $(-1, 0, +1)$ for (Anti-k_{T}, CA, k_{T}) respectively.

Typical characteristics of the different variants are that for the k_{T} algorithm d_{ij} is dominated by the soft component, the jet areas fluctuate significantly and are susceptible to the underlying event and pileup, but it is good for sub-structure studies; for CA, d_{ij} is independent of p_{T}, the areas fluctuate somewhat and it is somewhat susceptible to the underlying event and pileup, but it is best for sub-structure studies; while for the Anti-k_{T} algorithm d_{ij} is dominated by the hard component, the areas fluctuate little, it is only slightly susceptible to the underlying event and pileup, but it is worse for sub-structure studies [63]. Jets can be defined at different levels in an event, as shown in Fig. 50 (a):

- **Parton jets** made of quarks and gluons (after hard scattering, before hadronization);
- **Particle jets** composed of final-state colourless particles (after hadronization);
- **Detector jets** reconstructed from measured energy depositions and tracks.

The Jet Energy Scale (JES) and Resolution (JER) are important ingredients for precision studies. Energy scale calibration restores the jet energy to that of jets reconstructed at the particle level, correcting for detector imperfections, pileup, etc., as shown in Fig. 50 (b), achieving a few percent precision on the JES, and an example of the JER is shown in Fig. 50 (c).

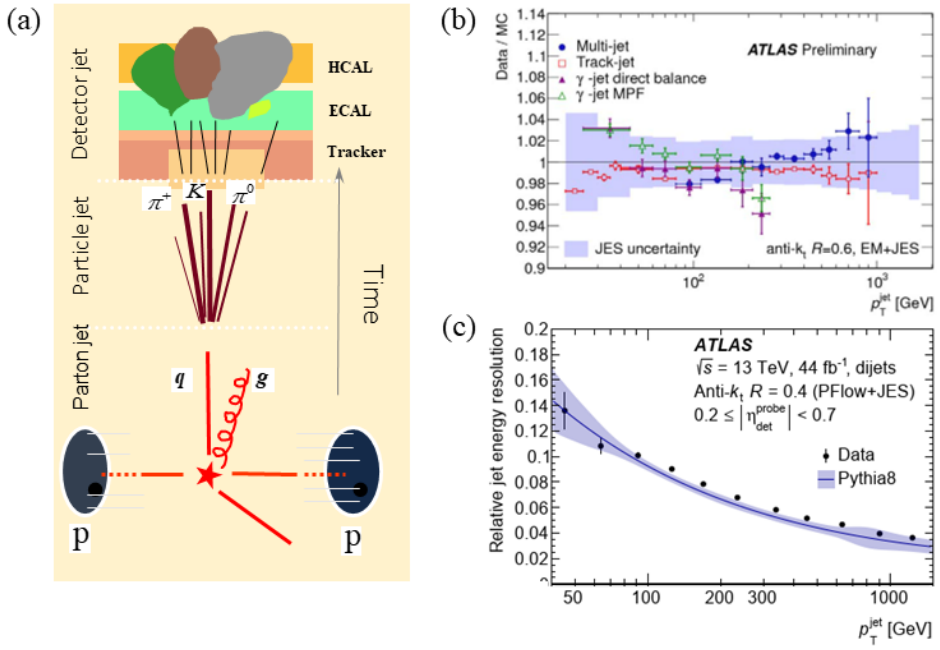

Fig. 50: (a) Different possible jet definitions, as a function of time from the interaction; (b) uncertainty on the Jet Energy Scale, as a ratio of data to Monte Carlo simulation [64]; (c) the Jet Energy Resolution, vs the transverse momentum of the jet [65].

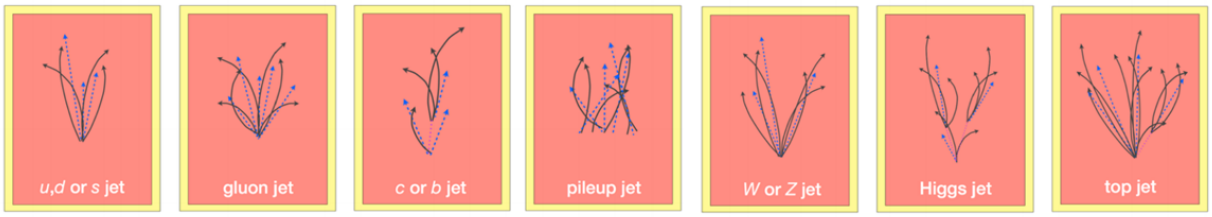

Fig. 51: Sketches of jet topologies corresponding to different underlying processes [22].

Qualitatively, different quarks or gluons produce different jet topologies: the different radiation patterns and lifetimes can be discriminated via the topologies, as illustrated in Fig. 51. Jets can also be formed from hadronic decays of high-p_{T} heavy particles. By studying the patterns, information can be gained about the process in the event, or can be used to identify new physics signatures.

Inclusive jet cross-sections have been studied doubly-differential in p_{T} and y, as shown in Fig. 52 (a):

$$\frac{d^2\sigma}{dp_{\mathrm{T}}\,dy} = \frac{1}{\varepsilon\mathcal{L}_{\mathrm{int}}}\frac{N_{\mathrm{jets}}}{\Delta p_{\mathrm{T}}\,(2\Delta|y|)} \quad . \tag{9}$$

The dominant systematic uncertainties are from JES and JER (ranging from 2–30%, largest at low p_{T} and in high rapidity regions). Next-to-Leading-Order (NLO) predictions agree well with data, and the fits allow improved constraints to be made on the parton distribution functions (PDFs). The dijet mass spectrum also shows good agreement with the expectations from QCD, as shown in Fig. 52 (b). If deviations were seen at large p_{T} they could hint at substructure inside the quarks (as in Rutherford scattering) or other new physics.

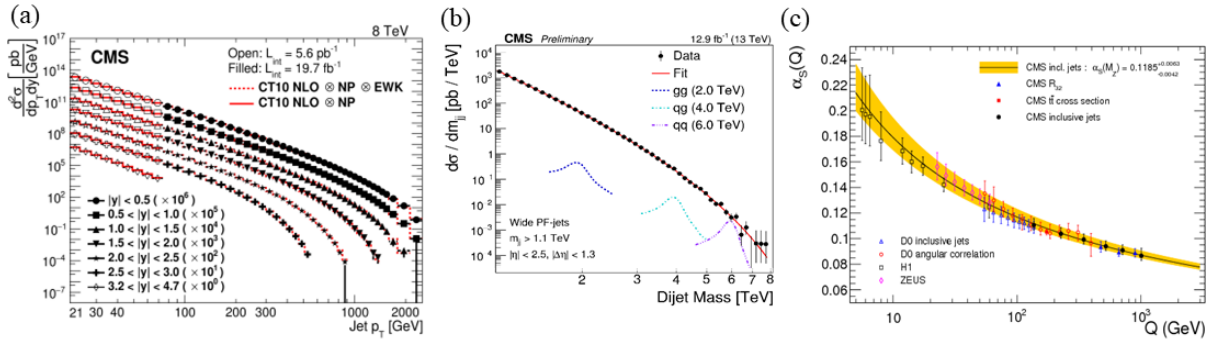

Fig. 52: Inclusive jet cross-sections for (a) single jets vs p_{T} for different regions in y [66], and (b) pairs of jets vs the dijet mass [67]; (c) the extracted value of the strong coupling constant vs the energy scale Q from measurements of inclusive jets from CMS, compared to values from earlier experiments [68].

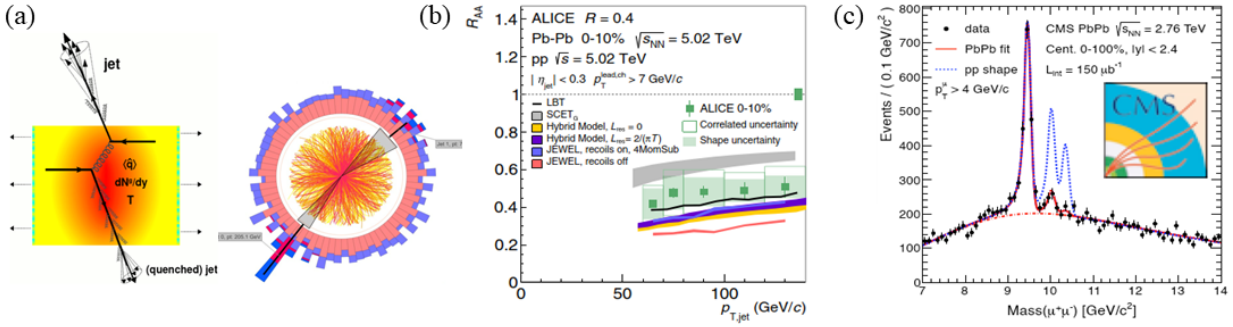

Fig. 53: (a) The process by which jets are quenched, by interaction of their parent parton with the QGP medium (left, shaded region), and illustration of how the effect of jet quenching is seen in an experiment (right); (b) ratio between jets in Pb-Pb and pp collisions (suitably normalized) from ALICE [69]; (c) suppression of the excited Υ states in Pb-Pb compared to pp collisions, from CMS [70].

The strong coupling constant α_{s} can be extracted from the inclusive jet measurements by varying its value in the theoretical prediction (for a given PDF set) and comparing to the data to find the best fit. The "running" of α_{s} to lower values as the energy increases is clearly seen, as expected in QCD, see Fig. 52 (c)—the energy scale Q is taken here to be the jet p_{T}.

Quark-gluon plasma

A deconfined state of strongly interacting matter described by QCD is expected in heavy-ion collisions at high energy at the LHC.[32] Numerous observables including jet quenching, as well anisotropic flow, J/ψ and Υ ($\mathrm{b\bar{b}}$) suppression provide evidence that the hot QCD state produced in such collisions is a quark-gluon plasma, see Fig. 53. Jet quenching refers to the suppression of jets due to their parent parton losing energy in the medium: larger jet quenching is seen for gluon jets compared to quark jets.

Top quark physics

The top quark is the most massive of the known elementary particles. Within the Standard Model it can be produced singly or in pairs, and has a very short lifetime: 5×10^{-25} s, so it decays *before* hadronisation, providing an unique opportunity to study the bare quark. Top physics lies at the boundary between strong and EW physics. The top-Higgs Yukawa coupling is large, $\lambda_t \approx 1$, so it plays a special role in electroweak symmetry breaking and is a window to new physics that might couple preferentially

[32] For more details see the lectures of Maelena Tejeda-Yeomans.

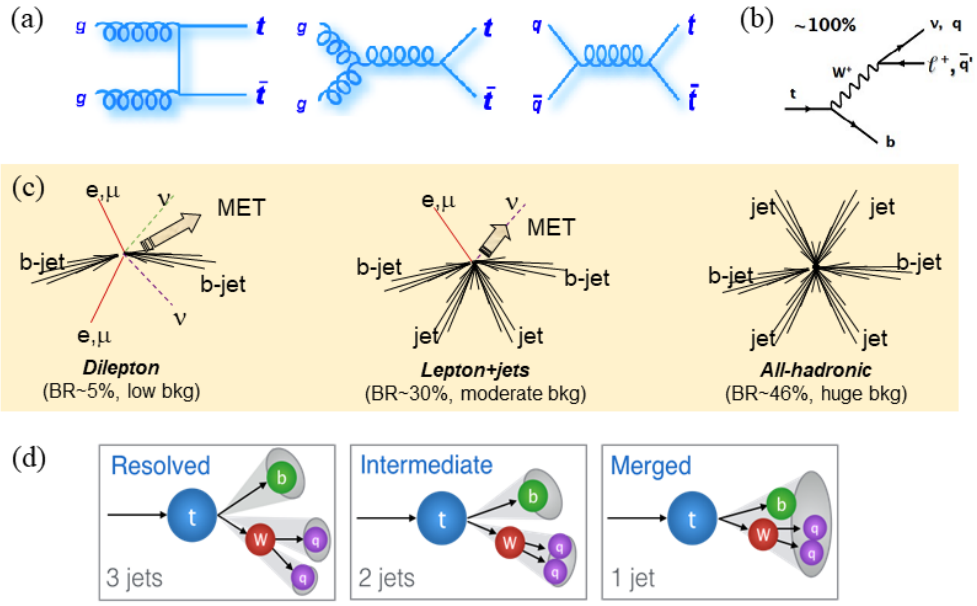

Fig. 54: (a) The main production diagrams of top pairs; (b) top quark decay; (c) sketch of the event types for different top pair decays; (d) the merging of jets in top decay as the p_{T} increases [22].

to top. Precision measurements allow for stringent tests of the Standard Model. The next heaviest quark, the b (bottom or beauty), is produced more copiously (as indicated in Fig. 45 (a)) but *does* hadronise—it will be discussed later.

The main top production mechanism at the LHC is pair production via the strong interaction, as shown in Fig. 54 (a). Within the SM the top quark decays into $\mathrm{b}+\mathrm{W} \sim 100\%$ of the time, see Fig. 54 (b). The W boson can decay into two quarks or into a charged lepton plus neutrino; a $\mathrm{t\bar{t}}$ event should therefore have either: 6 quarks; 4 quarks, 1 charged lepton and 1 neutrino; or 2 quarks, 2 charged leptons and 2 neutrinos, as sketched in Fig. 54 (c). In all cases, two b-quark jets are present in the event.

Identifying $\mathrm{t\bar{t}}$ events is traditionally done by associating one object to each final state decay product, and combining the objects to reconstruct each top decay. The combinatorics can become unwieldy, however: there are 6 or more jets in the all-hadronic decay mode! If the top quarks are boosted, the decay products are collimated, and may be reconstructed in same jet, see Fig. 54 (d). These merged decays can be used in other cases as well, reconstructing W, Z, and Higgs boson decays. A large amount of acceptance can be gained for hadronic channels by using such substructure, which typically account for over half of the decays. A "jet mass" can be computed by adding up constituent particle 4-vectors and calculating their invariant mass, as shown in Fig. 55. A radius parameter $R = 0.8$ is chosen for for heavy object reconstruction in the analysis shown there, where the top signal can be distinguished from the QCD background, with merged W/Z at $p_{\mathrm{T}} \sim 200\,\mathrm{GeV}$ and merged top at $p_{\mathrm{T}} \sim 400\,\mathrm{GeV}$.

Advanced techniques such as jet grooming algorithms can improve the discrimination between QCD and top quark jets, by removing soft and wide-angle radiation from within the jet (see Fig. 56). One can also look inside the jet for the expected substructure: top decays have three sub-jets, while W/Z/H decays have two. A quantity called N-subjettiness is used, a measure of how consistent a jet is

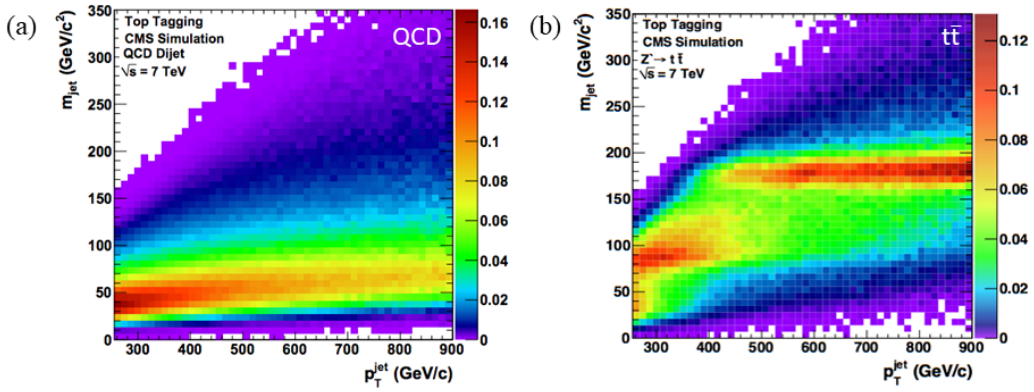

Fig. 55: Reconstructed jet mass vs p_{T} for (a) QCD background and (b) top pair events, in simulation [22].

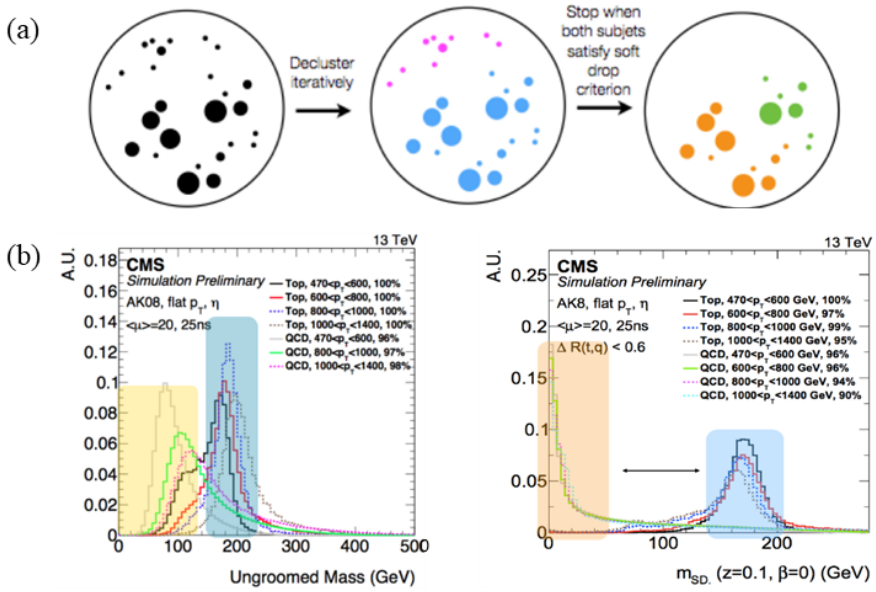

Fig. 56: (a) Jet grooming (the Soft Drop algorithm); (b) impact of jet grooming on the reconstruction of top decays, where the separation of signal (blue) from background (yellow) is increased, comparing when grooming is not (left) or is applied (right) [71].

with the hypothesized number of sub-jets.

The measurement of the top-pair cross-section at 13.6 TeV was one of the first new results from Run 3, see Fig. 57 (a). It is a combination of five channels: $\mathrm{e}\mu$, ee, $\mu\mu$, e+jets, μ+jets. The measurement is in agreement with predictions at next-to-next-to-leading order (NNLO) in perturbative QCD, including resummation of the next-to-next-to-leading-logarithmic (NNLL) soft gluon terms using the TOP++ v2.0 program [72].

Single-top production is a probe of the $\mathrm{W} \to \mathrm{t\bar{b}}$ interaction, with no assumption on the number of quark families or unitarity of the CKM matrix. The different production mechanisms are shown in Fig. 57 (b): the t-channel is dominant, then Wt (which both require a b quark from the sea) and finally the s-channel (which requires an antiquark). All agree with the predictions.

The mass of the top quark is a fundamental parameter of the Standard Model, that affects theory predictions for exploring Higgs-boson properties and in the search for new physics. The top quark is

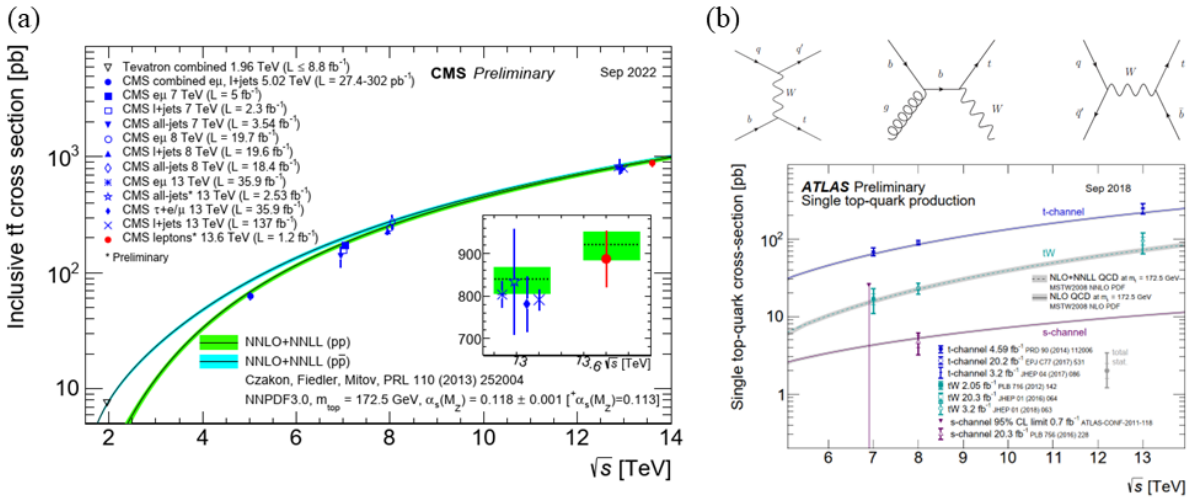

Fig. 57: (a) Measured $\mathrm{t\bar{t}}$ cross-section *vs* collision energy, including latest Run 3 result at highest energy [72]; (b) diagrams for single-top production (above) and measured cross-sections (below) [73].

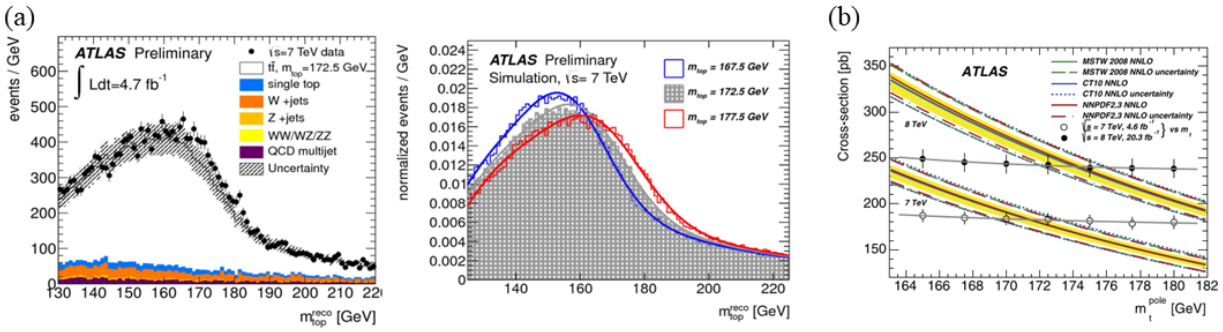

Fig. 58: (a) Reconstructed top mass in the lepton-jet channel (left) and templates for different top masses (middle) [74]; (b) Predicted $\mathrm{t\bar{t}}$ production cross-sections at $\sqrt{s} = 7$ and 8 TeV for different PDF sets, as a function of m_{pole}; cross-section measurements from the ATLAS dilepton analysis are overlaid, with their dependence on the assumed value of the mass [75].

colour charged and does not exist as an asymptotic state: the value of m_{t} extracted from the experiments depends on the theoretical definition of the mass, which varies according to the renormalisation scheme adopted: the *pole* or *running* mass. Relating the mass extracted based on Monte Carlo simulation and the (theoretically well-defined) pole mass is subject to an uncertainty of $\sim 1\,\mathrm{GeV}$, comparable to the present experimental precision. An example is shown in Fig. 58 (a), with templates at different masses in the lepton-jet final state channel. Alternative approaches have been investigated to measure the top mass, e.g. extracting it from the measured top cross-section as illustrated in Fig. 58 (b). All values are consistent, and the current world average is $m_{\mathrm{t}} = 173.34 \pm 0.76\,\mathrm{GeV}$ (i.e. 0.4% precision).

Top production is asymmetric: at the Tevatron ($\mathrm{p\bar{p}}$ collisions) the top quarks are emitted preferentially in the direction of incoming quark, and anti-top in the direction of incoming antiquark, leading to a forward-backward asymmetry, as illustrated in Fig. 59 (a). Inclusive asymmetries measured using $\sim 5\,\mathrm{fb}^{-1}$ at the Tevatron exceeded SM predictions by $\sim 2\,\sigma$, see Fig. 59 (b). At the LHC the initial state is symmetric (pp) but there is a related *charge* asymmetry due to the difference in rapidity distributions, sketched in Fig. 59 (c). The LHC results for this asymmetry are in agreement with the SM expectations, so the earlier discrepancy from the Tevatron has not been confirmed.

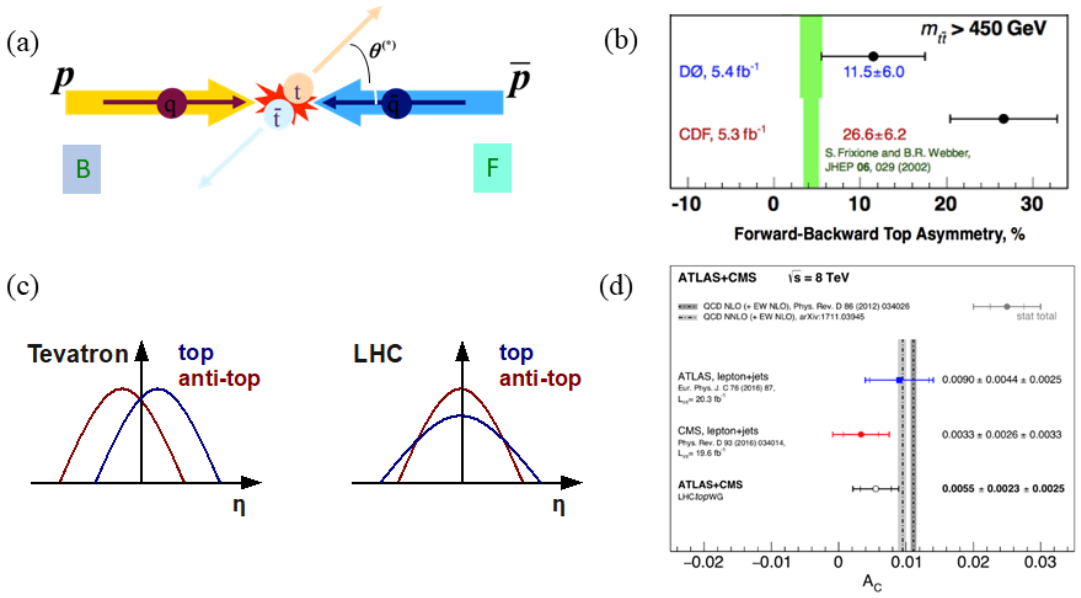

Fig. 59: (a) Sketch of the forward-backward asymmetry in top production at the Tevatron; (b) early measurements from the experiments at the Tevatron [22]; (c) comparison of asymmetries at the Tevatron and LHC; (d) results on the charge asymmetry A_C from the LHC [76].

3.2 Flavour physics

The top is the heaviest quark but does not hadronize; the next heaviest are beauty and charm, with a rich hadron spectrum and interesting weak decays, the realm of "flavour physics". The cross-section for $b\bar{b}$ production at 14 TeV: $\sigma_{b\bar{b}} \sim 500\,\mu$b, and that for charm is even higher, so they have an enormous production rate at LHC: $\sim 10^{12}\,b\bar{b}$ pairs per year (i.e. much higher statistics than the earlier B factories). $\sigma_{b\bar{b}} < 1\%$ of the inelastic cross-section, so there is significant background from non-b events that needs to be rejected. In addition, all b-hadron species are produced: the $B^0, B^+, B_s, B_c, \Lambda_b$, etc. LHCb is the main flavour physics experiment at the LHC—ATLAS and CMS also participate but mostly via lepton triggers, and with poorer hadron identification. LHCb runs at lower luminosity, to limit pileup for precision vertexing. The proper time of the B decay needs to be measured, as sketched in Fig. 60 (a): $t = m_B L/pc$, and hence the decay length L (~ 1 cm in LHCb). For much of the physics one also needs to tag the *production* state of the B, i.e. whether it was produced as a B or $\overline{B}$: for this one can use the charge of leptons or kaons from the decay of the *other* b hadron in the event.

The strong and electromagnetic interactions conserve C, P and T, for example in pion decay via the electromagnetic interaction: $\pi^0 \to \gamma\gamma$ but not $\gamma\gamma\gamma$; the initial state has $C(\pi^0) = +1$, and for the final state $C(\gamma\gamma) = (-1)^2 = +1$ while $C(\gamma\gamma\gamma) = (-1)^3 = -1$. On the other hand the weak interaction violates parity, as was first seen in the classic experiment of Wu, Fig. 60 (b). Neutrinos are left-handed, while antineutrinos are right-handed, so perhaps the weak interaction conserves the combined operation, CP? e.g. $\Gamma(\pi^+ \to \mu^+\nu_L) = \Gamma(\pi^- \to \mu^-\overline{\nu}_R)$, see Fig. 60 (c). The weak interaction did indeed appear to conserve CP, until the experiment of Christenson et al. (in 1964) detected rare decays of the K^0_L to the "wrong" CP state: $K^0_L \to \pi^+\pi^-\pi^0$ (CP $= -1$, $\mathcal{B} = 34\%$); $K^0_L \to \pi^+\pi^-$ (CP $= +1$, $\mathcal{B} = 2 \times 10^{-3}$), i.e. CP violation was observed. CP violation unambiguously differentiates matter from antimatter, e.g. $\mathcal{B}(K^0_L \to \pi^- e^+ \nu) = 19.46\% > \mathcal{B}(K^0_L \to \pi^+ e^- \overline{\nu}) = 19.33\%$ [6]. In the Standard Model, CP violation

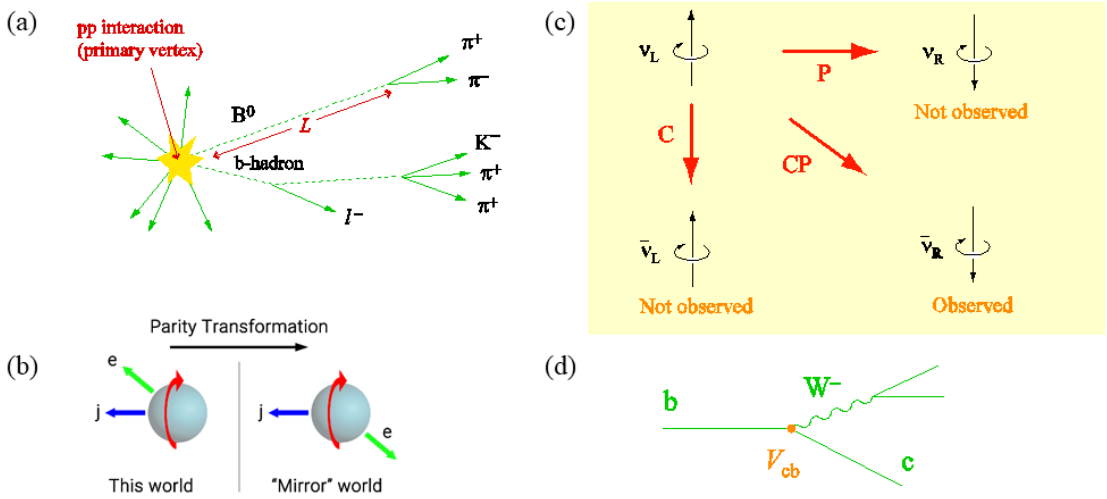

Fig. 60: (a) Sketch of the tracks close to the primary (production) vertex in a $\mathrm{b\bar{b}}$ event; (b) polarised cobalt-60 atoms undergoing β decay in the experiment of Wu, where a difference was seen in the rates under the parity transformation [77]; (c) neutrinos transforming under C and P operations; (d) diagram for b-quark decay, indicating the weak coupling at the decay vertex (here for a $\mathrm{b} \to \mathrm{c}$ decay).

arises from quark mixing. The weak charged current is given by: $(u, c, t)(1-\gamma_5)\gamma_\mu(d', s', b')$, where the weak eigenstates are a "rotated" combination of the flavour states:[33]

$$\begin{pmatrix} d' \\ s' \\ b' \end{pmatrix} = \begin{pmatrix} V_{\mathrm{ud}} & V_{\mathrm{us}} & V_{\mathrm{ub}} \\ V_{\mathrm{cd}} & V_{\mathrm{cs}} & V_{\mathrm{cb}} \\ V_{\mathrm{td}} & V_{\mathrm{ts}} & V_{\mathrm{tb}} \end{pmatrix} \begin{pmatrix} d \\ s \\ b \end{pmatrix} \quad . \tag{10}$$

V is the unitary CKM (Cabibbo-Kobayashi-Maskawa) matrix. Its elements give the weak couplings between quark flavours, as illustrated in Fig. 60 (d). Unitarity of the CKM matrix implies relationships between its rows and columns: $\sum V_{ij}V_{ik}^* = 0$ $(j \neq k)$. One of these relationships has terms of similar size: $V_{\mathrm{ud}}V_{\mathrm{ub}}^* + V_{\mathrm{cd}}V_{\mathrm{cb}}^* + V_{\mathrm{td}}V_{\mathrm{tb}}^* = 0$, corresponding to a triangle relationship in the complex plane, shown in Fig. 61 (a). The (3×3) CKM matrix has 4 independent parameters: 3 angles and one non-trivial phase which gives rise to CP violation—this is only present with ≥ 3 generations, and at present is the only known source of CP violation in the Standard Model. The CKM matrix is observed to have a hierarchy of elements, and was parameterized by Wolfenstein [78] expanding in powers of the Cabibbo angle[34]: $\lambda = \sin\theta_{\mathrm{C}} \approx 0.22$. The parameters (λ, A, ρ, η) are shown in Fig. 61 (b); $A \approx 0.8$ is measured, leaving ρ and η to be determined, i.e. the coordinates of the apex of the Unitarity Triangle; $\eta \neq 0$ implies CP violation. The matrix has a rather diagonal form for the quarks, unlike the equivalent (PMNS) mixing matrix for neutrinos.

Flavour physics observables have sensitivity to new particles at high mass scales via their virtual effects in *loop* diagrams, including the "penguin" (first order) and "box" (second order) diagrams shown in Fig. 62 (a). Decays without loops (known as "tree" diagrams) are expected to be less affected. Pen-

[33] For more details see the lectures of Matthias Neubert.
[34] Not to be confused with the Cherenkov angle, despite sharing the same symbol.

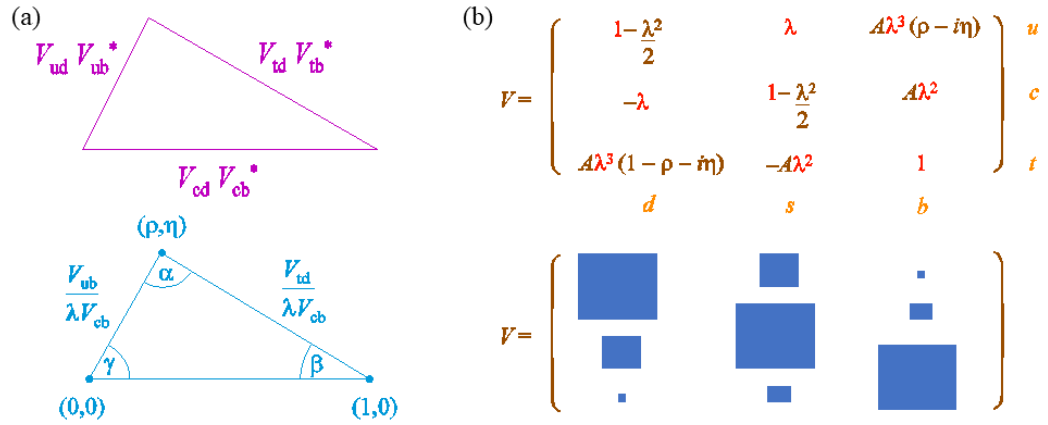

Fig. 61: (a) Unitarity relation between CKM matric elements (above) and after rescaling the sides by $V_{\rm cd}V_{\rm cb}^*$ to give the "Unitarity Triangle" (below); (b) the CKM matrix elements, expanding in powers of λ (above), and with boxes indicating their relative size (below).

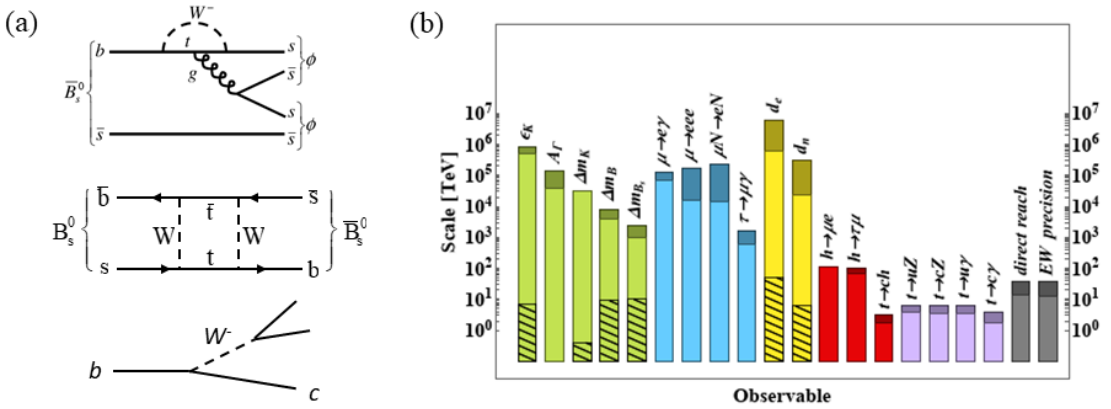

Fig. 62: (a) Examples of different types of loop diagrams: penguin (above) and box (middle), along with a tree diagram (below); (b) the power of indirect measurements, plotted as the sensitivity to the scale of new physics for a variety of observables [79].

guins[35] contribute to Flavour Changing Neutral Current (FCNC) decays like $\mathrm{B_s} \to \mu\mu$, which are not possible at tree-level in the SM. The box diagram is interesting as it allows a particle to transform into its antiparticle: the quantum mechanical effect of oscillation between neutral states (also seen for neutrinos and neutrons). As illustrated in Fig. 62 (b), such "indirect" measurements can be very powerful.

The pattern of oscillation of neutral mesons between their particle and antiparticle states, mediated by the box diagram, is shown in Fig. 63 (a): they depend on the mass difference Δm and width difference $\Delta\Gamma$ between their weak eigenstates e.g. $\Delta m \propto |V_{\rm td}|^2$ for the $\mathrm{B^0}$; often expressed in terms of dimensionless parameters, the frequency $x = \Delta m/\Gamma$, and the width difference $y = \Delta\Gamma/2\Gamma$. Oscillations have now been observed for all of the species, and the pattern observed is consistent with SM expectations. The spectacular measurement of the rapid $\mathrm{B_s^0}$–$\overline{\mathrm{B}}_\mathrm{s}^0$ oscillations in LHCb via the $\mathrm{B_s^0} \to \mathrm{D_s^-}\pi^+$ channel is shown in Fig. 63 (b), giving the world's best precision on the frequency:

[35] Named by John Ellis, who also lectured at this school—so the students could ask him why he chose that name, as well as photograph him with real penguins.

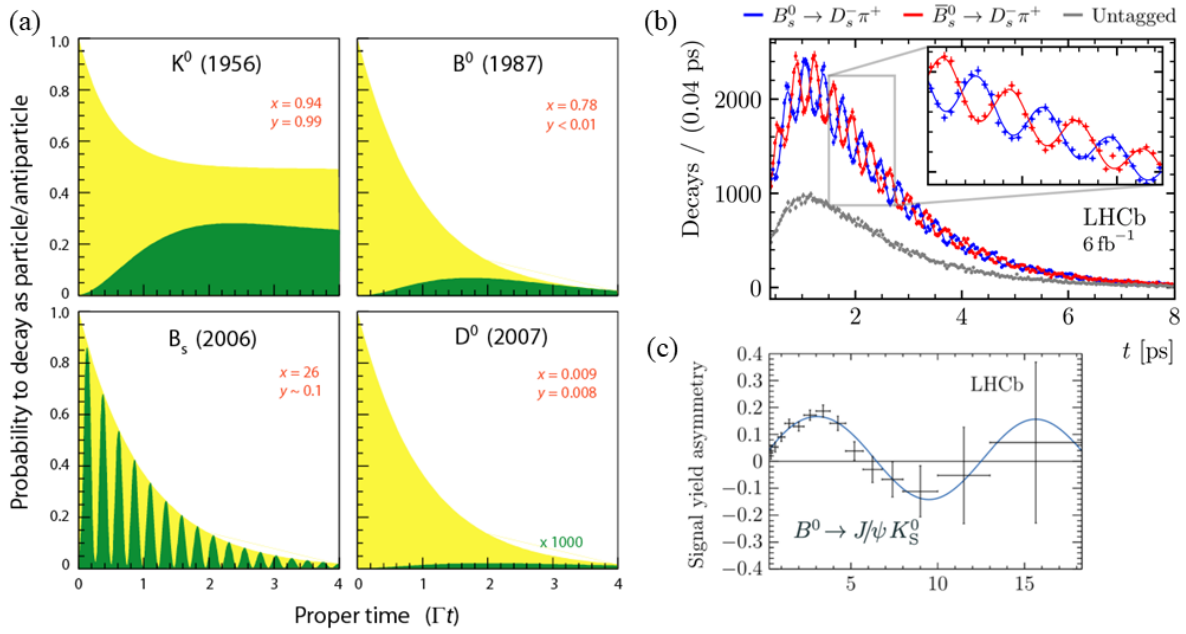

Fig. 63: (a) The pattern of oscillation between particle and antiparticle expected for the various neutral mesons; measurement of oscillations for (b) $\mathrm{B_s^0}$ [80] and (c) $\mathrm{B^0}$ [82].

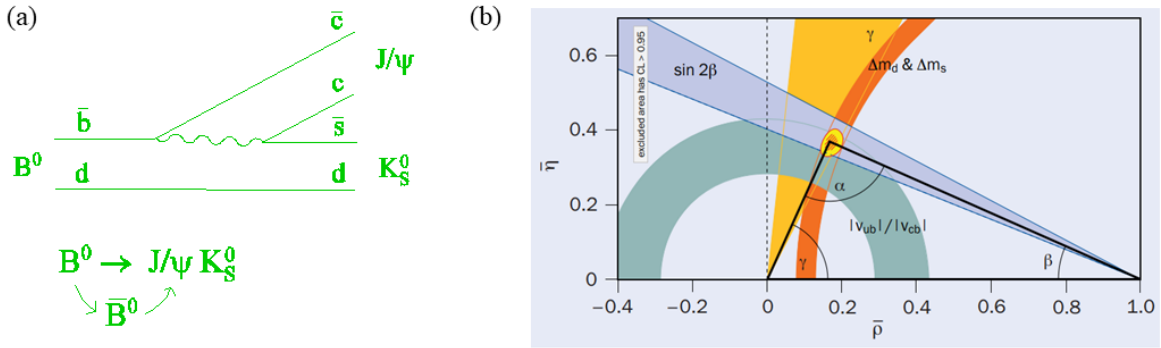

Fig. 64: (a) Diagram for the $\mathrm{B^0}$ decay to the CP eigenstate $\mathrm{J/\psi\,K_S^0}$ (above) and its possible alternative path via mixing (below); (b) current constraints on the apex of the Unitarity Triangle [84].

$\Delta m_\mathrm{s} = 17.7683 \pm 0.0051 \pm 0.0032\,\mathrm{ps}^{-1}$ [80]. The frequency can be predicted [81]:

$$\Delta m_q = \frac{G_\mathrm{F}^2}{6\pi^2}\,\eta\, m_{\mathrm{B}_q} B_{\mathrm{B}_q} F_{\mathrm{B}_q}^2 M_\mathrm{W}^2 S_0(m_\mathrm{t})\,|V_{tq}|^2 \quad , \tag{11}$$

where non-perturbative hadronic factors such as B_{B_q} can be estimated by solving QCD on a discrete space-time lattice, using Lattice gauge theory. For $\mathrm{B^0}$ mixing this gave first clear (indirect) evidence that the top quark mass was heavy [83]. $\mathrm{D^0}$ mixing has also been measured in LHCb via $\mathrm{K_S^0\,\pi^+\pi^-}$ decays, giving small values for the x and y parameters $\mathcal{O}(10^{-3})$ in agreement with the SM expectation, and $\mathrm{B^0}$ mixing via $\mathrm{J/\psi\,K_S^0}$, see Fig. 63 (c).

Many of the measurements made of hadrons containing the b quark can be presented as constraints on the Unitarity Triangle. In addition, CP violation measures the relative *phases* of the matrix elements, and hence measures the angles (α, β, γ) of the triangle, depending on the decay. $\mathrm{B^0} \to \mathrm{J/\psi\,K_S^0}$ is a

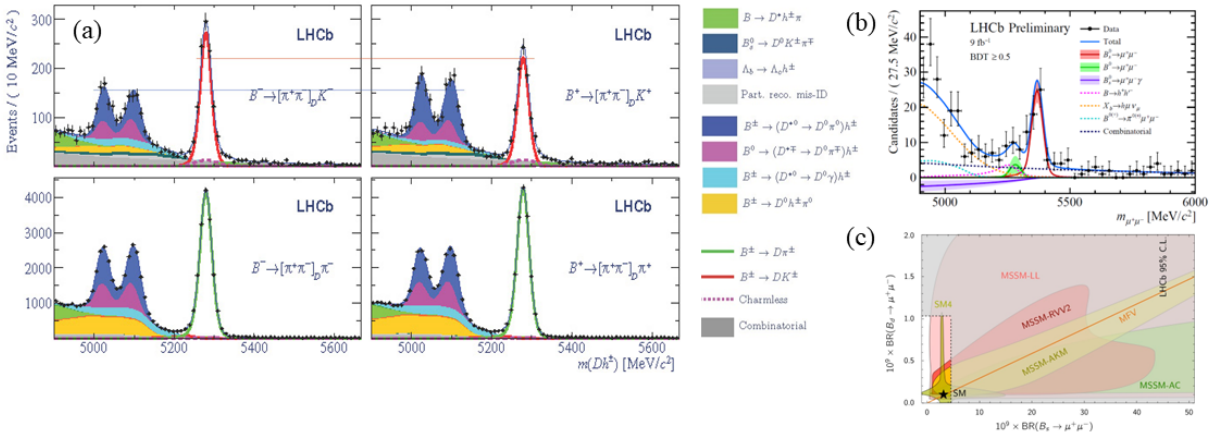

Fig. 65: (a) Analysis of $\mathrm{B} \to \mathrm{D}h$ decays showing clear CP violation [85]; (b) signal for the very rare decay $\mathrm{B}_\mathrm{s}^0 \to \mu^+\mu^-$ [86]; (c) constraints on the parameter space for new physics models, as a result of the measurements of B^0 and $\mathrm{B}_\mathrm{s}^0 \to \mu^+\mu^-$ [87].

decay to a CP eigenstate, and can occur "via mixing" with a different phase, as shown in Fig. 64 (a). This depends on the phase of B^0–$\overline{\mathrm{B}}^0$ oscillation: $\arg(V_\mathrm{td})$ = angle β. As seen Fig. 64 (b) the measurement of β is in triumphant agreement with the other constraints on the apex of the triangle. The results from almost all flavour measurements are consistent,[36] and the Standard Model description of CP violation appears to be correct (at least to the level tested).

An example of a measurement showing clear CP violation is given in Fig. 65 (a): $\mathrm{B} \to \mathrm{DK}$, that depends on the CP-angle γ, where the height of the two (red) signal peaks are clearly different in the two charge-conjugate final states. Many different channels have been studied, and all are consistent with the CKM picture. CP violation has also been seen in charm decays for the first time: this is expected to be small in Standard Model, $\mathcal{O}(10^{-3})$, and the observed value is consistent with expectations.

Rare decays of b and c hadrons are also a fertile ground to search for new physics: e.g. the decay $\mathrm{B}_\mathrm{s}^0 \to \mu^+\mu^-$ is very strongly suppressed, but precisely predicted in the Standard Model, $\mathcal{B}(\mathrm{B}_\mathrm{s}^0 \to \mu^+\mu^-) = (3.7 \pm 0.2) \times 10^{-9}$, so it is an excellent place to search for new physics contributions, which could modify the branching ratio. As shown in Fig. 65 (b, c) the decay has been measured, in agreement with the expectation, and a large range of the parameter space for new physics has been constrained.

3.3 Electroweak physics

Study of vector boson production allows precision measurement of Standard Model parameters, tests of perturbative QCD, and input to PDF fits. There are also irreducible background to many searches where signal events decay to W or Z's: top, Higgs and BSM. Leptonic decays provide clean samples, as shown in Fig. 66, with adequate statistics for performance measurements. The signature for a W decay is a high p_T isolated lepton with large missing E_T, while for the Z it is two oppositely charged, same flavour, high p_T leptons. Employing a "tag and probe" method, the clean $\mathrm{Z} \to \mathrm{e}^+\mathrm{e}^-$ or $\mu^+\mu^-$ sample can be used to measure lepton selection efficiencies (trigger, ID, isolation). The *tag* lepton is required to pass tight selection requirements to ensure the sample purity, allowing the *probe* lepton to be unbiased with respect

[36] The exceptions, the so-called "flavour anomalies", will be discussed in the 4$^{\mathrm{th}}$ lecture.

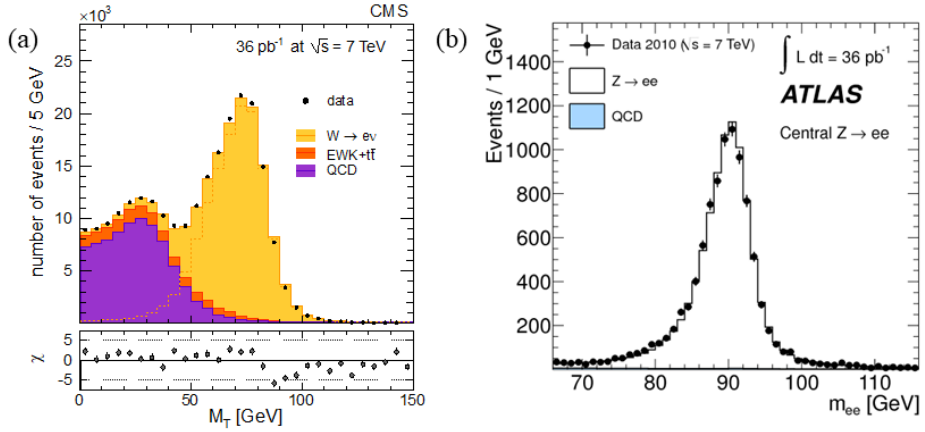

Fig. 66: Vector boson signals (a) $\mathrm{W} \to \ell\nu$ [88]; (b) $\mathrm{Z} \to \ell\ell$ [89].

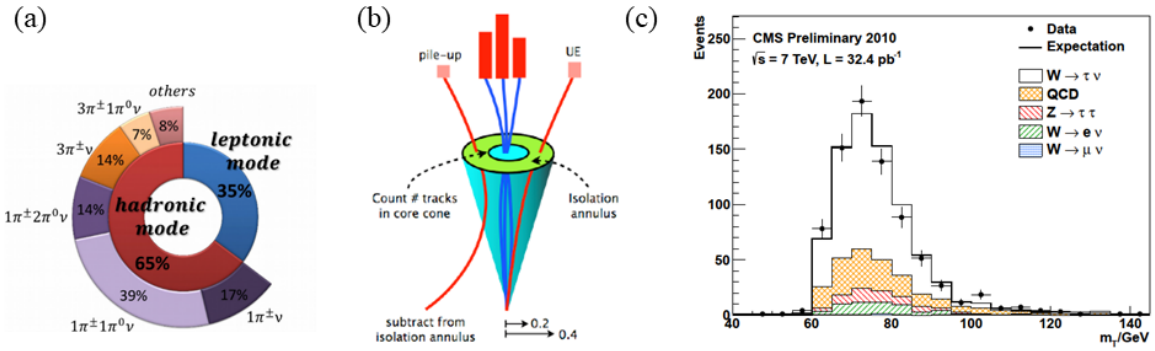

Fig. 67: (a) Decay modes of the tau; (b) reconstructing tau decays with an isolation criterion; (c) signal for $\mathrm{W} \to \tau\nu$ [90].

to the selection that is being studied, and one counts how often the probe lepton passes the requirement under study. If the statistics are high enough, this method can be applied in bins of the relevant variables. The same method can be applied to data and simulation to extract a data-to-MC correction factor for use in analysis. Other resonances like $\mathrm{J}/\psi \to \mu^+\mu^-$ can also be used for this method.

Tau leptons are an important probe for new physics processes at the LHC, such as searches for light Higgs bosons, Supersymmetry or extra dimensions. Taus decay to either an electron, muon or into a system of hadrons, as shown in Fig. 67 (a): hadronic decay modes (τ_{had}) are characterized by a highly collimated jet of low particle multiplicity. The dominant source of tau leptons in the SM is from W decays; they can selected using isolation criteria, see Fig. 67 (b). The charge asymmetry of the signal shown in Fig. 67 (c) has been measured:

$$\frac{\mathcal{B}(\mathrm{W}^+ \to \tau^+\nu)}{\mathcal{B}(\mathrm{W}^- \to \tau^-\nu)} = 1.55 \pm 0.19\,^{+0.11}_{-0.13} \quad , \tag{12}$$

in agreement with the prediction 1.43 ± 0.04 at NNLO based on the various parton distribution functions.

The dominant processes for inclusive W-boson production in pp collisions are annihilation: $\mathrm{u\bar{d}} \to \mathrm{W}^+$ and $\mathrm{d\bar{u}} \to \mathrm{W}^-$ involving a valence quark from one proton and a sea antiquark from the other. Since the proton valence quarks are uud the cross-section is higher for $\mathrm{u\bar{d}}$ than for $\mathrm{d\bar{u}}$, leading to a clear charge

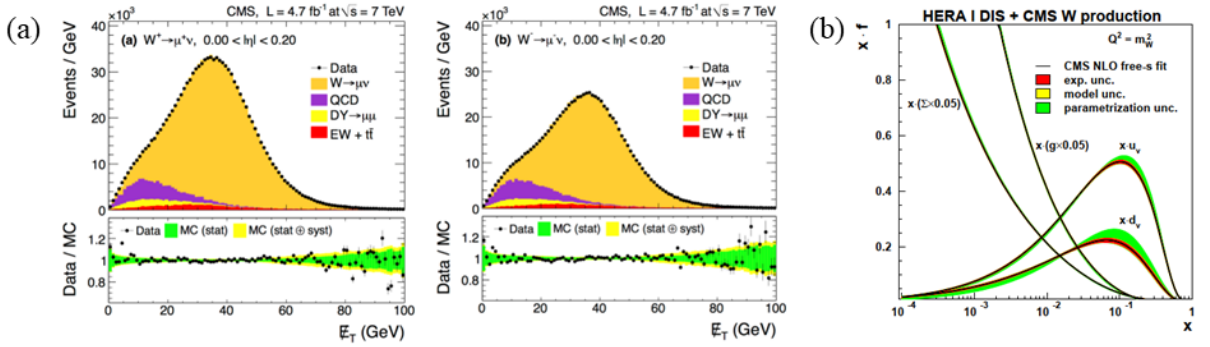

Fig. 68: (a) Missing transverse energy distributions in the analysis of $W^+ \to \mu^+\nu$ (left) and $W^- \to \mu^-\nu$ (right) decays; (b) improved constraints on the proton PDFs from this analysis [91].

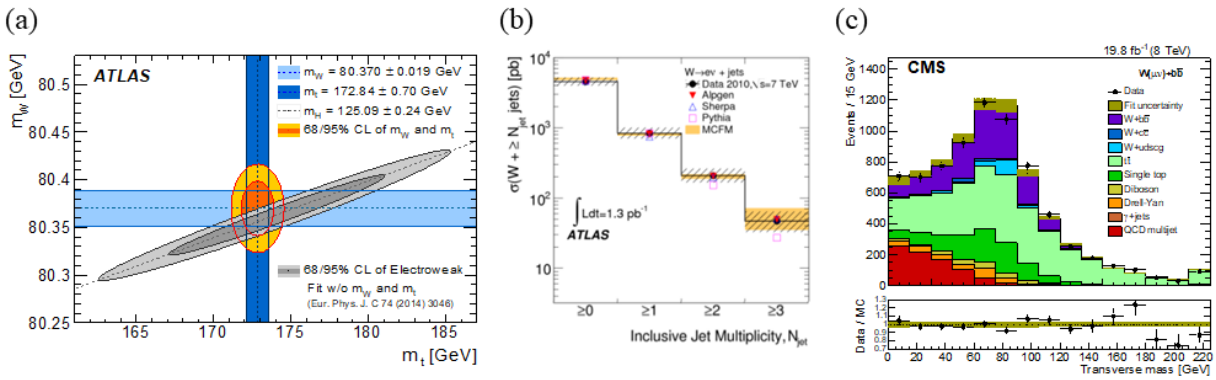

Fig. 69: (a) Measurements of m_{W} *vs* m_{t}, with the constraints from the Electroweak fit superimposed [92]; (b) inclusive jet multiplicity, for events with a $\mathrm{W} \to \mathrm{e}\nu$ decay [93]; (c) transverse mass distribution for events with $\mathrm{b\bar{b}} + \mathrm{W} \to \mu\nu$ [94].

asymmetry in the production, visible in Fig. 68 (a), with value $1.421 \pm 0.006 \pm 0.032$. Such studies can be used to improve knowledge of parton distribution functions (PDF), see Fig. 68 (b). The W decay distributions are also sensitive to the W *mass*. The target is for an uncertainty of $\mathcal{O}(10\,\mathrm{MeV})$ on a mass of $\sim 80\,\mathrm{GeV}$, i.e. 0.01% precision. Statistics are not the issue, but rather the systematic uncertainties from modelling the missing neutrino, and the PDFs. ATLAS were the first to publish a W-mass measurement at the LHC, using 8M $\mathrm{W} \to \mu\nu$ plus 6M $\mathrm{W} \to \mathrm{e}\nu$ decays. The W mass was obtained from template fits to $p_{\mathrm{T}}(\ell)$ and transverse mass m_{T}, with $\mathrm{Z} \to \ell\ell$ used for lepton energy and W recoil calibration. The result: $m_{\mathrm{W}} = 80370 \pm 7(\mathrm{stat}) \pm 11(\mathrm{exp.\ syst}) \pm 14(\mathrm{model\ syst})\,\mathrm{MeV}$ [92]. The mass of the W, top quark and Higgs boson are related via radiative corrections, as was discussed in 1$^{\mathrm{st}}$ lecture: an update of the plot that was shown then (Fig. 9 (b)) with the latest results is given in Fig. 69 (a), which becomes a precision test of the SM.

W + jets production has been studied, with events selected with one high p_{T} isolated lepton and at least one jet, see Fig. 69 (b). These provide valuable input for the u, d and g PDFs of the proton. The data are well described by ME generators matched to parton shower and normalized to NLO pQCD. W + b/c samples, as in Fig. 69 (c), are valuable for understanding the background to Higgs searches. Multiboson events are also of interest: scattering of two vector bosons (VBS) $\mathrm{VV} \to \mathrm{VV}$ (with V = W or Z) is an important process to study the mechanism of electroweak symmetry breaking. VBS was one motivation for introducing the Higgs boson: the forward scattering cross-section would violate unitarity

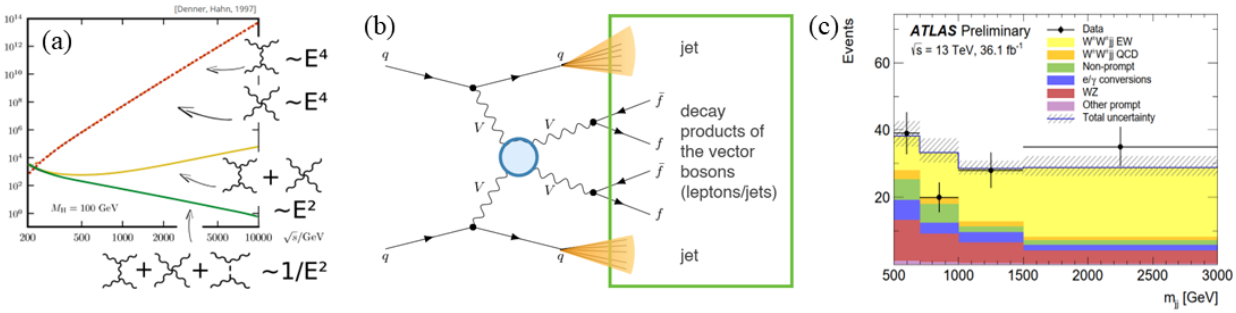

Fig. 70: (a) Illustration of the diagrams contributing to the VBS process, and how the cross-section would diverge with increasing energy if it were not for the contribution from the Higgs boson [95]; (b) the signature of VBS in an experiment, with two forward jets and the decay products of the two vector bosons; (c) signal for $\mathrm{W^+W^-}jj$ production [96].

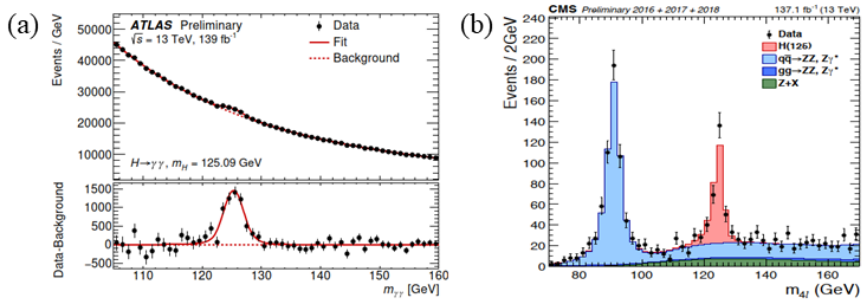

Fig. 71: The Higgs boson mass determination (a) $\mathrm{H} \to \gamma\gamma$ [97]; (b) $\mathrm{H} \to \mathrm{ZZ}^* \to 4\ell$ [98].

at high energy without the Higgs, as illustrated in Fig. 70. $\mathrm{W^+W^-}jj$ production has been seen with 6.9 σ significance, in agreement with the Standard Model expectation.

3.4 Higgs boson properties

As discussed earlier, the Higgs boson was finally discovered in 2012 after 50 years of searching, via the discovery channels $\mathrm{H} \to \gamma\gamma$ and $\mathrm{H} \to \mathrm{ZZ}^* \to 4\ell$. Precision measurements of the Higgs boson properties will provide a crucial test of the Standard Model. It represents a potential window to physics beyond the SM: it is the most recent discovery, and the mechanism feels a little *ad hoc*—the Higgs boson found may be the first sighting in a more complex sector. However, so far it does look pretty much like a SM Higgs, but several aspects still remain to be explored.

Recall that the mass of the Higgs boson is not predicted in Standard Model, it had to be measured. The discovery modes shown in Fig. 36 are also the ones with the highest sensitivity to the mass, which have now been updated with much higher statistics (see Fig. 71) giving $m_{\mathrm{H}} = 125.09 \pm 0.24\,\mathrm{GeV}$ (i.e. 0.2% precision). Precision measurements of Higgs and top masses take a central role in the question of the stability of the electroweak vacuum: top-quark radiative corrections can drive the Higgs-boson self-coupling (λ)[37] towards negative values, leading to an unstable vacuum, see Fig. 72 (a). New physics must appear by the energy scale (μ) at which this happens. From the current measured values, shown in Fig. 72 (b), the Universe is at the boundary of stability! It sits in a meta-stable region, but with a lifetime

[37] Another overused symbol, not to be confused with its use elsewhere to represent wavelength or in the Wolfenstein parameterization of quark mixing.

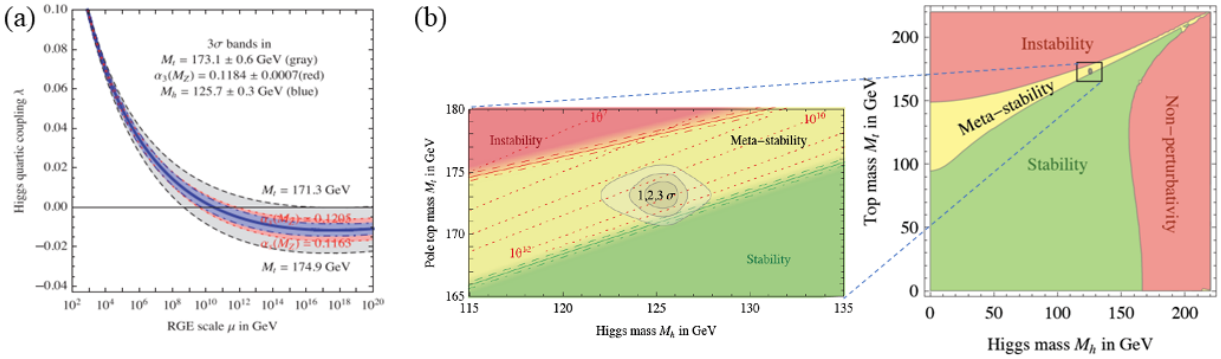

Fig. 72: (a) Evolution of the Higgs coupling to high energy scale; (b) stability of the vacuum vs the top-quark and Higgs masses, with a zoom around the measured values [99].

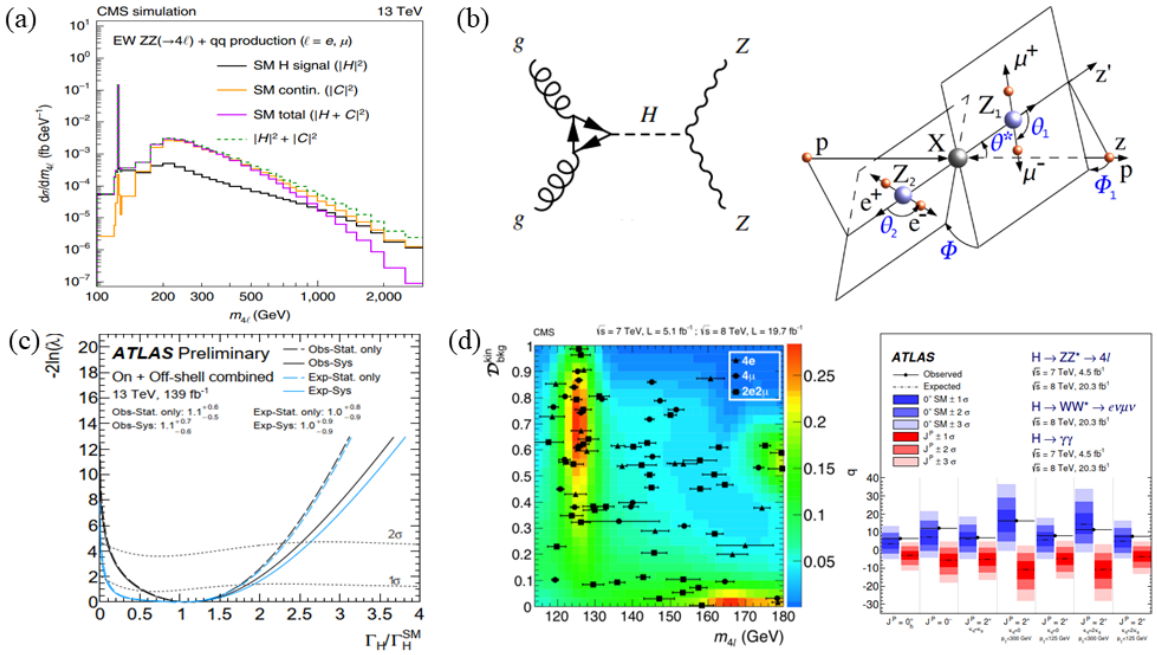

Fig. 73: (a) Simulated mass distribution for $H \to ZZ^* \to 4\ell$, showing the on-shell (peak at 125 GeV) and off-shell production [100]; (b) the gluon-fusion production diagram for $H \to ZZ$ (left) and definition of decay angles for analysis of $ZZ \to 4\ell$ (right); (c) measured likelihood as a function of Γ_H/Γ_H^{SM} [101]; (d) observed data are compared to discriminant distributions to calculate a likelihood for different spin states (left) and different hypotheses are tested (right, where the SM is blue and alternative spin hypotheses red) [103].

$\gg$ that of the Universe, so there is no immediate concern that the vacuum will collapse—and no clear evidence that new physics is needed until high scale.

A direct measurement of the *width* of the Higgs boson from the mass distribution is limited by the experimental resolution of ~ 1 GeV: the observed mass distributions are consistent with a natural width $\ll$ the resolution. In addition to the peak at 125 GeV from on-shell Higgs production, non-resonant (off-shell) production is expected at higher masses, as shown in Fig. 73 (a). Assuming no new particles enter the gluon-fusion diagram loop of Fig. 73 (b), Γ_H can be extracted from the ratio of Higgs boson events

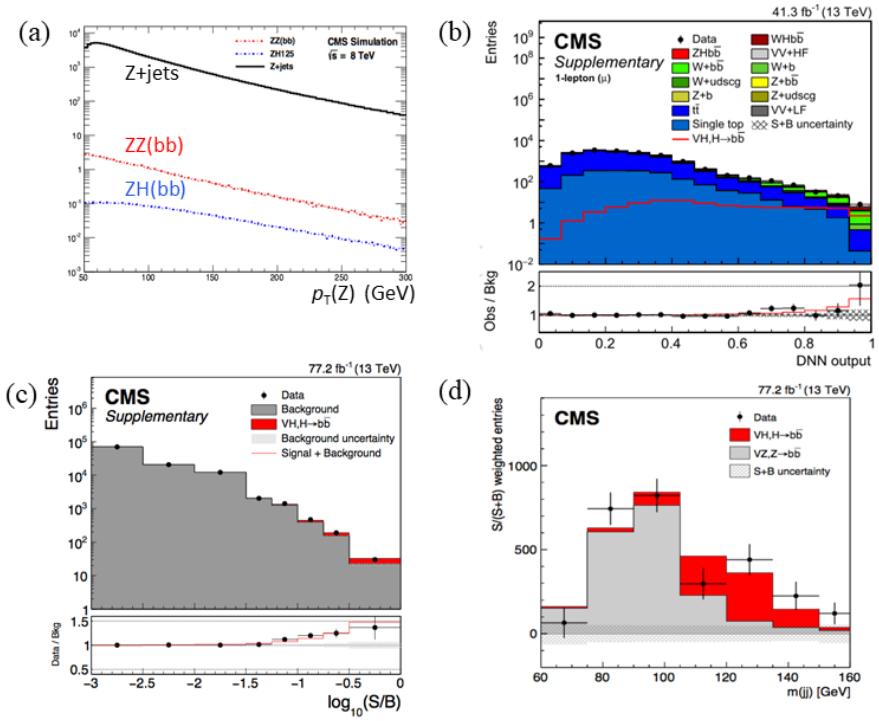

Fig. 74: VH(bb) analysis (a) $p_{\mathrm{T}}(\mathrm{Z})$ spectrum showing the dominant Z+jets background (note the logarithmic scale); (b) an example of the discrimination of signal using a neural network, here for the single-lepton (μ) channel; (c) combining all channels, plotted vs S/B; (d) final mass plot showing VZ (grey) and VH (red) contributions [104].

observed in the two regimes:

$$\sigma^{\text{on-shell}}_{\mathrm{gg}\to\mathrm{H}\to\mathrm{ZZ}} \propto \frac{g^2_{\mathrm{ggH}}\, g^2_{\mathrm{HZZ}}}{m_{\mathrm{H}}\,\Gamma_{\mathrm{H}}}\,, \quad \sigma^{\text{off-shell}}_{\mathrm{gg}\to\mathrm{H}\to\mathrm{ZZ}} \propto \frac{g^2_{\mathrm{ggH}}\, g^2_{\mathrm{HZZ}}}{m^2_{\mathrm{ZZ}}}\,. \tag{13}$$

Both ATLAS and CMS see $\sim 3\,\sigma$ evidence for off-shell production, and extract values for width consistent with the SM expectation of 4.1 MeV (at $m_{\mathrm{H}} = 125$ GeV), see Fig. 73 (c).[38]

Following its discovery, one of the key questions was to determine the quantum numbers J^{P} of the new particle: its spin ($J = 0$ for a scalar) and parity $\mathrm{P} = +1$ in the Standard Model. Since it decays to two photons, it is not spin-1 (from the Landau-Yang theorem [102]), so it is either spin-0 or spin-2 (it could also be higher spin, but that is strongly disfavored). Using the angular information in the $\mathrm{H} \to \mathrm{ZZ}^* \to 4\ell$ decays, the different spin-parity hypotheses can be tested, as illustrated in Fig. 73 (d). Alternatives to 0^+ are ruled out at > 99% CL.

Once m_{H} has been measured, the production and decay modes can all be calculated. At the LHC, the dominant prouction modes are gluon fusion (ggF, 83%), vector-boson fusion (VBF, 7%), associated production with a vector boson (VH, 7%), or with $\mathrm{t\bar{t}}$ (ttH, 3%). As an example, the search for VH(bb) is illustrated in Fig. 74, i.e. the decay $\mathrm{H} \to \mathrm{b\bar{b}}$—this has the largest branching ratio, but suffers from severe multi-jet QCD background, so searching for it with associated production with a vector boson (V = W or Z) helps control the background. There are three channels with 0, 1, and 2 leptons and two b-tagged

[38] Remember: lifetime $\propto$ inverse of width, $\tau = \hbar/\Gamma$. Although the Higgs width is small, its lifetime is still short: $\sim 10^{-22}$ s ($\hbar = 6.6 \times 10^{-16}$ eV · s).

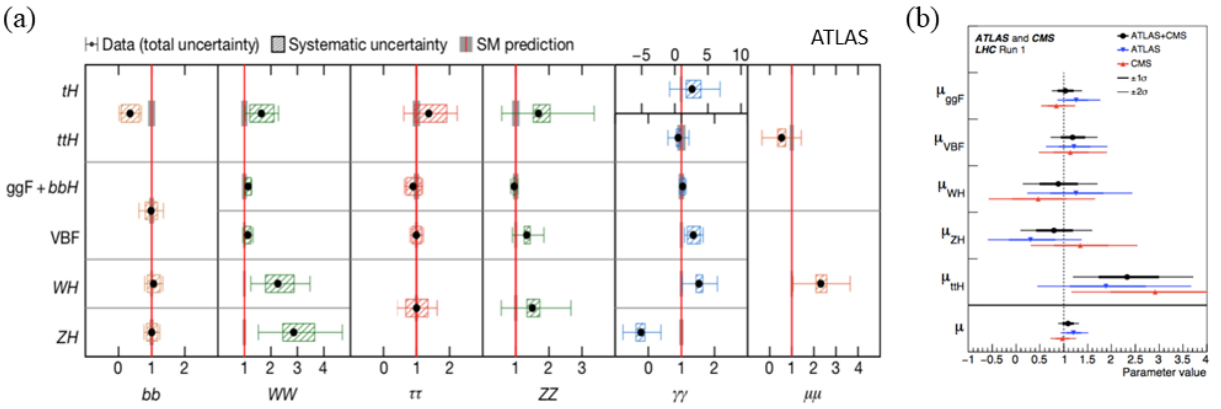

Fig. 75: (a) Summary of measured Higgs boson production and decay modes (arranged vertically and horizontally, respectively), compared to the SM predictions; (b) the μ values (ratio to the SM expectation) for the different production modes, and their overall combination giving $\mu^{\mathrm{LHC}} = 1.09\,^{+0.11}_{-0.10}$ [106].

jets, targeting Z($\nu\nu$)H, W($\ell\nu$)H and Z($\ell\ell$)H processes with $\mathrm{H} \to \mathrm{b\bar{b}}$. The W/Z is required to have large boost ($\sim 150\,\mathrm{GeV}$) so that the multi-jet QCD background is highly suppressed. Control regions are used to validate analysis variables and constrain background normalizations, and a simultaneous fit is made to the signal and control regions. Machine Learning in the form of a Neural Network discriminator is used to separate signal from background, via a multivariate analysis exploiting the most discriminating variables: $m_{\mathrm{b\bar{b}}}$, p_{T}(V), and b-tagging. It is validated with data/MC comparison, trained separately in each channel. The performance is optimized using blind analysis (i.e. masking the central value until the selection has been decided). All signal channels are combined and plotted as a function of signal/background per event. Overall the data are compatible with the S+B hypothesis, with a signal significance of $4.8\,\sigma$, $\mu = 1.01 \pm 0.23$ (where μ is the ratio of the observed cross-section to that expected in the Standard Model). Combined with the Run 1 data, $5.6\,\sigma$ is achieved ($5.5\,\sigma$ expected), $\mu = 1.04 \pm 0.20$, greater than the $5\,\sigma$ threshold, so the decay has been observed.[39]

Enormous effort has been invested in the study of all aspects of the Higgs boson: all of the production modes mentioned earlier have been seen, as expected in the Standard Model. For the decay modes, WW was seen early (in Run 1) then $\gamma\gamma$ (2017) and $\mathrm{b\bar{b}}$ (2018)—important as it measures the coupling to fermions rather than gauge bosons. So far only decays to third generation fermions have been seen clearly (since the Higgs boson couples to mass, they have highest branching ratios). For the second generation, evidence has been seen for $\mu\mu$ (to be confirmed), and $\mathrm{c\bar{c}}$ is under study but still far from reaching SM sensitivity.

The Higgs boson couplings are non-universal: it couples to particles with coupling strength proportional to their mass. All results seen so far are consistent with this prediction, and the SM in general, as shown in Fig. 76. There could be invisible decays of the Higgs boson: in the Standard Model this only occurs via $\mathrm{H} \to \mathrm{ZZ}^* \to 4\nu$ with a tiny branching ratio, $\mathcal{B} \sim 0.1\%$. However, it could be strongly enhanced if the Higgs couples to Dark Matter—after all, the evidence for DM is gravitational, and the Higgs couples to mass. Invisible decays are searched for using associated production (VBF or VH) with

[39] A similar analysis has been made by ATLAS [105], and as is usually the case the two experiments have similar performance (including their choice of colours for the final plot!).

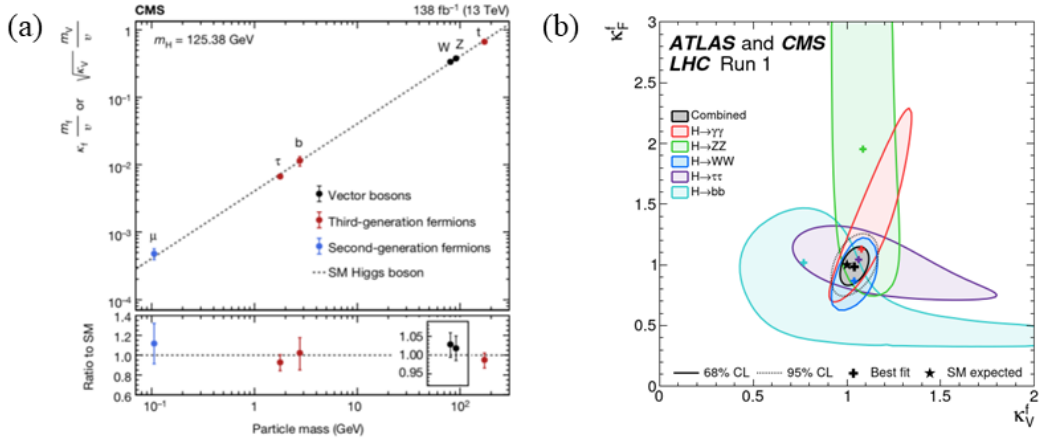

Fig. 76: (a) Higgs couplings as a function of particle mass [107]; (b) measured couplings in different channels, plotted as fermionic vs bosonic coupling strengths [6].

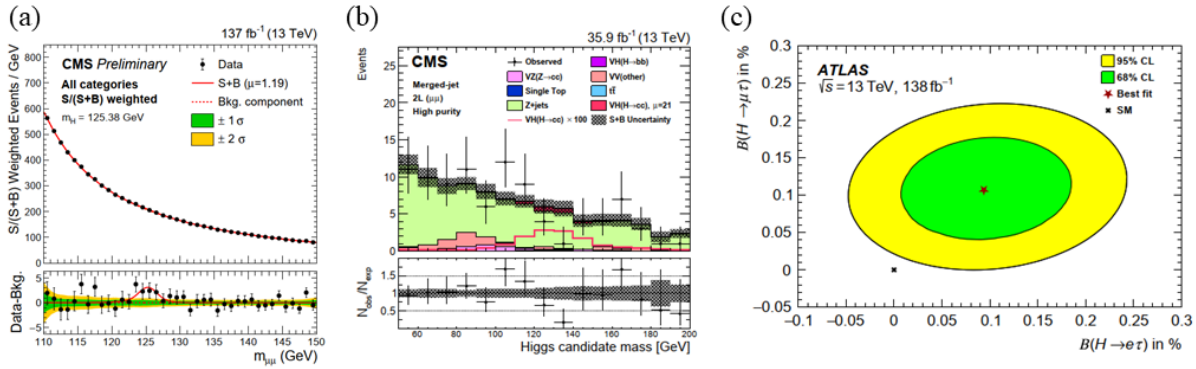

Fig. 77: (a) Search for $\mathrm{H} \to \mu\mu$ [109]; (b) search for $\mathrm{H} \to \mathrm{c\bar{c}}$ [110]; (c) search for $\mathrm{H} \to \mathrm{e}\mu$ plotted vs $\mathrm{H} \to \mu\tau$, showing a modest but interesting discrepancy with the SM, that is worth keeping an eye on [111].

large MET. The best limit so far is $\mathcal{B}(\mathrm{H} \to \mathrm{inv}) < 19\%$ at 95% CL [108].

As mentioned, second-generation couplings have been searched for: $\mathrm{H} \to \mu\mu$ has a branching ratio (in the SM) of 2.2×10^{-4}, and evidence now seen at $3\,\sigma$ significance, see Fig. 77 (a). $\mathrm{H} \to \mathrm{c\bar{c}}$ is very tough experimentally, as the $\mathrm{H} \to \mathrm{b\bar{b}}$ background must be suppressed. The current upper limit is at $70 \times$ the SM, see Fig. 77 (b). Lepton Flavour Violating decays such as $\mathrm{H} \to \mathrm{e}\mu$ or $\mu\tau$ have also been searched for, as shown in Fig. 77 (c). There is a still a lot to be understood about the Higgs mechanism. Searching for Higgs pair-production is vital step towards measuring the self-coupling of the Higgs boson, λ. Measurements of the trilinear Higgs interaction would provide constraints on the shape of the Higgs potential close to the minimum, and would allow the electroweak symmetry breaking mechanism of the SM to verified. HH production is also possible via a box diagram, without invoking the self-coupling, as shown in Fig. 78 (a), and the two diagrams interfere making this a rare process. Upper limits are currently about $7 \times$ higher than the expected signal strength in the Standard Model, see Fig. 78 (b).

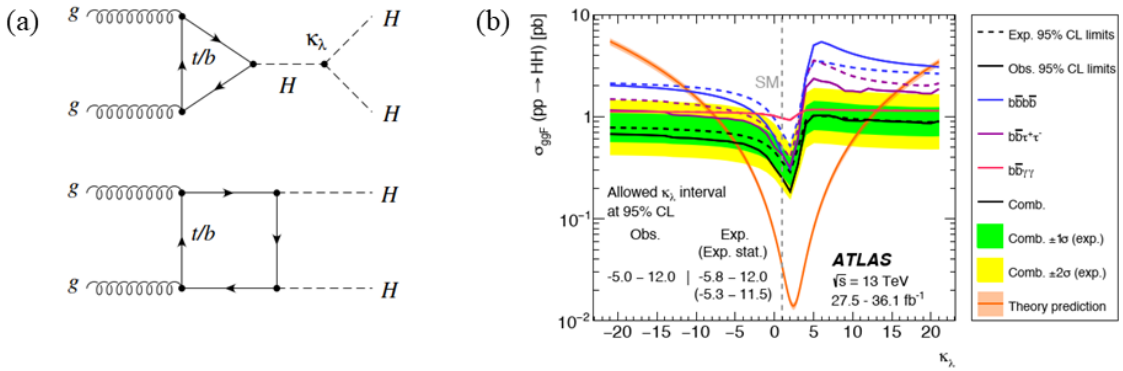

Fig. 78: (a) Diagrams contributing to HH production, via the trilinear coupling (above) and the box diagram (below); (b) sensitivity to the Higgs self-coupling λ as a function of the coupling modifier κ_λ, which would be 1 in the SM [112].

3.5 Summary of the third lecture

There is a very wide range of physics results from the LHC, from which only selected highlights could be presented. Concerning the strong interaction the total cross-section has been measured, jet production studied, as well as the Quark Gluon Plasma (at ALICE and elsewhere), and there are many results for top quarks. Striking results have been shown in flavour physics (mostly from LHCb), for particle-antiparticle oscillations, CP violation in beauty and charm decays, and the study of rare decays. Electroweak physics is mostly the province of the general-purpose experiments ATLAS & CMS, and illustrates the tendency towards precision measurements, e.g. for the W mass. The Higgs boson can currently *only* be studied at the LHC: its properties have started to be measured in detail, but more remain to be revealed—in particular its self-coupling and potential. Overall the Standard Model continues to be triumphant, with the measured cross-sections agreeing with predictions over 12 orders of magnitude, as was shown earlier in Fig. 45 (b). The last lecture will explore why are we not satisfied with this impressive status, and consider where new physics might be found.

4 Looking beyond

This final lecture looks beyond the Standard Model to consider where evidence for new physics might be seen, and also beyond the LHC towards future colliders. To recap some of the unanswered questions, which lead us to think that the Standard Model cannot be the full story:

- Why are there 3 generations of quarks & leptons?
- Are quarks & leptons fundamental, or made up of even more fundamental particles?
- What is the reason for the pattern of particle masses?
- What gives neutrinos their mass?
- Why do we observe matter and almost no antimatter, if there is symmetry between them?
- What is Dark Matter that can't be seen but has gravitational effects in the cosmos?
- How does gravity fit in?
- Why is the Higgs boson so light?

The Standard Model is likely not to be *wrong*, but a low-energy limit of a more complete theory—similar

Fig. 79: Quantum corrections to the Higgs boson mass.

to how Newtonian mechanics has been superseded by Special Relativity.

Considering the last of the points above, the Higgs mass is on the electroweak scale (125 GeV), but is unstable with respect to large predicted quantum corrections: $m_{\rm H}^2 = m_0^2 + \delta m_{\rm H}^2$, where the quantum corrections illustrated in Fig. 79 are given by:

$$\delta m_{\rm H}^2 = \frac{3\,G_{\rm F}}{4\sqrt{2}\pi^2}\,(2m_{\rm W}^2 + m_{\rm Z}^2 + m_{\rm H}^2 - 4m_{\rm t}^2 + ...)\,\Lambda^2 \quad . \tag{14}$$

Assuming new physics appears at scale Λ—unknown, but could be as high as the Planck scale[40]—the Higgs boson mass should be huge unless there is incredible fine-tuning in the cancellation between the quadratic radiative corrections and the bare mass m_0. Acceptable fine tuning is a matter of theoretical taste—if an explanation cannot be found, one may otherwise have to fall back on the anthropic principle: the hypothesis that copies of the Universe exist (the *Multiverse*) with differing parameters, and the parameters of our Universe are special because they must be suitable to sustain life, so that we can measure them. The drawback of this explanation is that it appears to be untestable.

4.1 Searches at the LHC

When the LHC was built, the front-runner for an explanation of the hierarchy problem was Supersymmetry—-the hypothesis that a symmetry exists related to particles' spin, between fermions and bosons: each SM boson would have a fermion "super-partner", and each fermion have a boson super-partner, as shown in Fig. 80 (a). Super-partners would then contribute with the opposite sign to the loop corrections to the Higgs mass providing cancellation of the divergent terms, see Fig. 80 (b). The Higgs sector would be extended to include 4 other scalar states, plus a whole zoo of new particles.

If Supersymmetry was exact, then the super-partners would have the same masses as the SM particles—and would already have been seen. So the symmetry must be broken, and many of the super-partners have higher mass to explain why they have not been seen. However, if this breaking is too great, the cancellation of the divergent terms becomes weaker and fine-tuning would still be required, so Supersymmetry was expected to show up at the TeV scale. It would not be the first time that the particle content has been doubled: that already happened when antiparticles were introduced, a symmetry based on electric charge—but they were found soon after their prediction. To avoid proton decay, as shown in Fig. 80 (c), an extra conservation rule is introduced (R-parity), opposite for SM particles and their super-partners: in this case the lightest supersymmetric particle (LSP) would be stable and becomes a candidate to explain Dark Matter (usually the neutralino, $\tilde{\chi}_1^0$). For a particle with baryon and lepton numbers B, L and spin s, $R = (-1)^{3B-3L+2s}$, giving $R = +1$ for SM particles, -1 for super-partners.

[40]The Planck scale is the energy $\sim 10^{19}$ GeV at which quantum effects of gravity become significant.

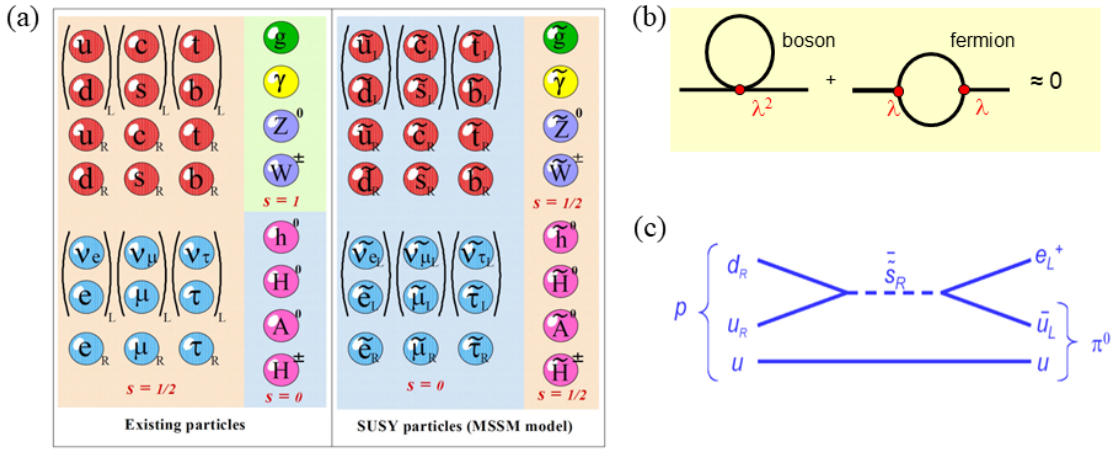

Fig. 80: (a) The increased particle content of Supersymmetry, where the super-partners of the SM particles (known as sparticles) are indicated with a ˜ over their symbol; (b) the cancellation of divergent terms; (c) a diagram that would allow proton decay.

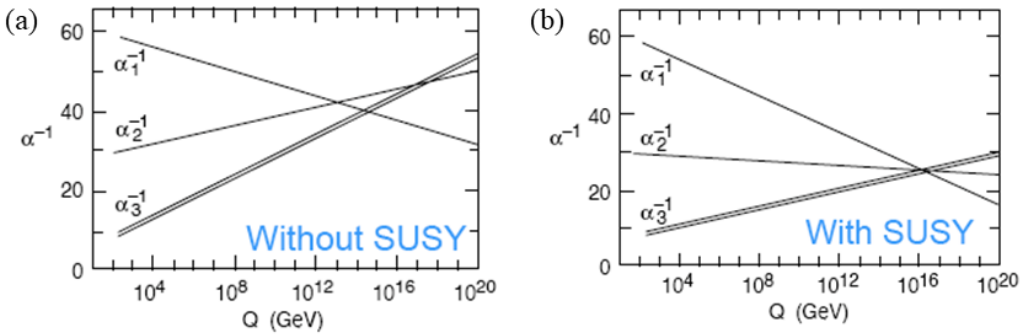

Fig. 81: Extrapolating the coupling "constants" to high energy scale (a) in the SM; (b) adding Supersymmetry [113].

Another argument made in favour of Supersymmetry concerns the coupling constants of the fundamental forces, that "run" with energy due to quantum corrections (as shown earlier for α_s). Evolving the coupling constants of the Standard Model measured at LEP to higher energy, they do not coincide: $\alpha_1, \alpha_2, \alpha_3$ are the coupling constants of the $\mathrm{SU(3)_C} \otimes \mathrm{SU(2)_L} \otimes \mathrm{U(1)}$ group corresponding to electromagnetic, weak and strong interactions. With the addition of Supersymmetry unification of the couplings becomes possible at a single Grand Unified Theory scale $\sim 10^{16}$ GeV, see Fig. 81.

Spectacular signatures were expected from Supersymmetry at the LHC, with the complicated decay chains giving multiple jets and missing transverse energy (MET) from the LSP, as illustrated in Fig. 82 (a). However, no significant signals have been seen, and limits have been set across the parameter space of super-partners, see Fig. 82 (b). Is Supersymmetry hiding? Most searches for it require the presence of substantial missing E_{T}, assumed to originate from the neutralinos that escape detection. But Supersymmetry could appear without MET:

– **Compressed** Supersymmetric spectra, i.e. a small mass difference between the LSP and top squark, and two LSP momenta balance;

– **Top "corridor"**: stop pair production can look identical to $\mathrm{t\bar{t}}$;

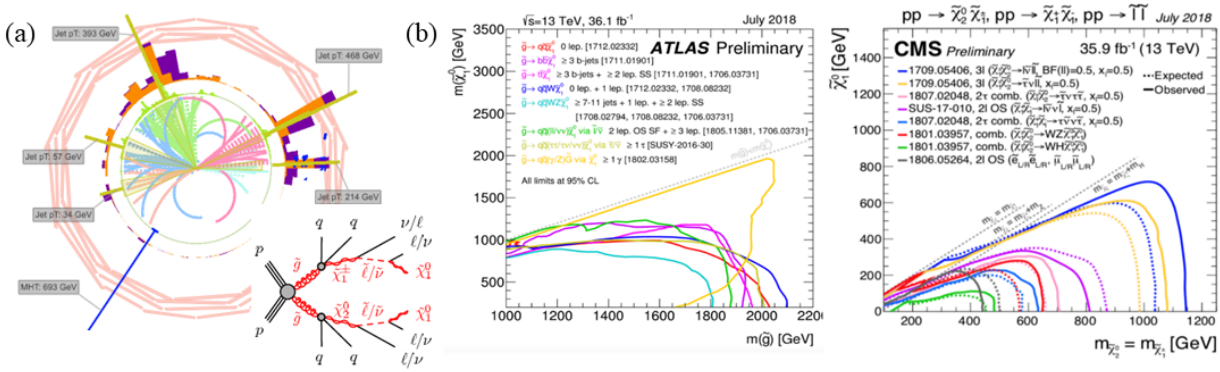

Fig. 82: (a) The signature of Supersymmetry in an experiment, with many jets + MET; (insert) a typical Supersymmetry decay chain; (b) examples of limits on supersymmetric particle parameter space.

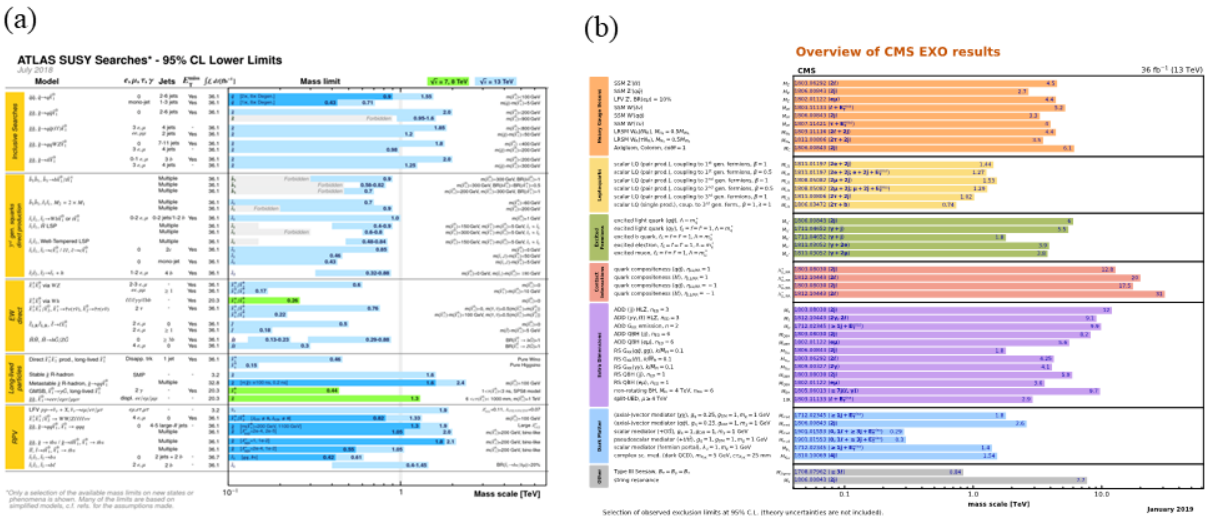

Fig. 83: Compilation of limits for (a) Supersymmetry; (b) other "exotic" BSM searches.

– **Stealth** Supersymmetry: decays through an approximately supersymmetric hidden sector can remove missing momentum from the signal;
– **R-parity violating** Supersymmetry: terms violate either Lepton or Baryon number conservation; together this could lead to rapid proton decay, so only a few couplings are allowed to be non-zero.

Many of these options contain no invisible particles, but rather extra leptons or extra jets, that may form resonances. So searches continue, but perhaps the new particle masses are too high for the LHC (or Supersymmetry is not the answer). An overview of current limits on Supersymmetry is shown in Fig. 83 (a).[41]

Searches for physics beyond the Standard Model (BSM) encompass a wide variety of ideas, including new gauge bosons, compositeness, ZZ/WW resonances, Technicolour, extra dimensions, microscopic Black Holes, Little Higgs, Hidden Valleys, etc. These exotic ideas often repeat similar signatures in the final state, such as leptons, missing energy, different configurations of jets and vector bosons, etc. This can encourage an experimentally-driven approach, where one searches for the signatures, keeping an open mind about the source of any non-Standard Model signals that might be discovered.

[41] Citations are given in the figures (if you can zoom in far enough).

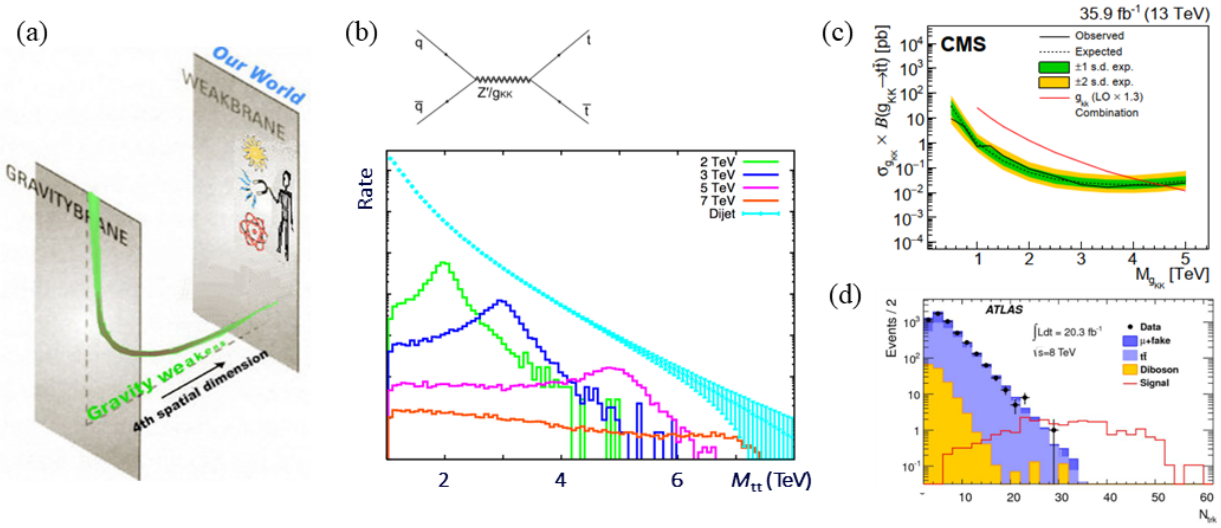

Fig. 84: (a) Adding an extra (warped) dimension, to account for the weakness of gravity in our world [114]; (b) search for a $\mathrm{t\bar{t}}$ resonance, where the signal peak position depends on the mediator mass; (c) resulting limit on the coupling of g_{KK} *vs* its mass [115]; (d) search for microscopic Black Holes, that would give a high track multiplicity [116].

Taking the example of extra dimensions: why are there four dimensions of space-time (x, y, z, t) in our world? Extending to additional dimensions is an alternative approach to solving the hierarchy problem, lowering the cut-off scale Λ to the TeV scale. Extra dimension(s) would need to be "rolled up" (compactified) to avoid being noticed. Randall-Sundrum models add a 5^{th} warped dimension, so that gravity can have a similar strength to the other forces (in the bulk) but is weak in our 4-dimensional world, see Fig. 84 (a). Such models can have new particles that are excitations of SM particles, e.g. a Kaluza-Klein excitation of the gluon (g_{KK}) which can decay preferentially to top-antitop pairs that would look like a resonance in the $M(\mathrm{t\bar{t}})$ spectrum.

Searches for $\mathrm{t\bar{t}}$ resonances have been made by the experiments. They are reconstructed from daughter top quarks via the $\mathrm{t} \to \mathrm{Wb}$ decay, e.g. using a boosted topology for hadronic decays, or the single lepton channel. Resonances are produced from colliding valence quarks and sea anti-quarks, and at high masses the resonance is smeared, as shown in Fig. 84 (b). As an example, requirements from a generic resonance search setting limits for explicit models, g_{KK} and Z′: exactly one high p_{T} electron or muon; no isolation requirement; at least two high p_{T} jets; large MET to reject multijet background; 1 top-tagged jet. An enriched W sample is used to measure top-tag misidentification, and $M(\mathrm{t\bar{t}})$ is used as the final observable. No signal was seen, so limits are set—the best limits at the time for $\mathrm{t\bar{t}}$ resonances, see Fig. 84 (c). Models with extra dimensions can also predict the formation microscopic Black Holes at LHC collisions, leading to very high multiplicity events, e.g. model of Arkani-Hamed, Dimopoulos and Dvali (ADD). No evidence has been found for them, e.g. see Fig. 84 (d), or for any other BSM signals so far, and an overview of current limits is shown in Fig. 83 (b).

If no mass bumps are found, i.e. the object being searched for has higher mass than that accessible at the LHC, one can still search for deviations in the *tails* of distributions by making precise measurements. This is the essence of the Effective Field Theory approach, illustrated in Fig. 85—becoming more important as no clear mass bumps of new particles have yet been seen. Deviations are parametrized by

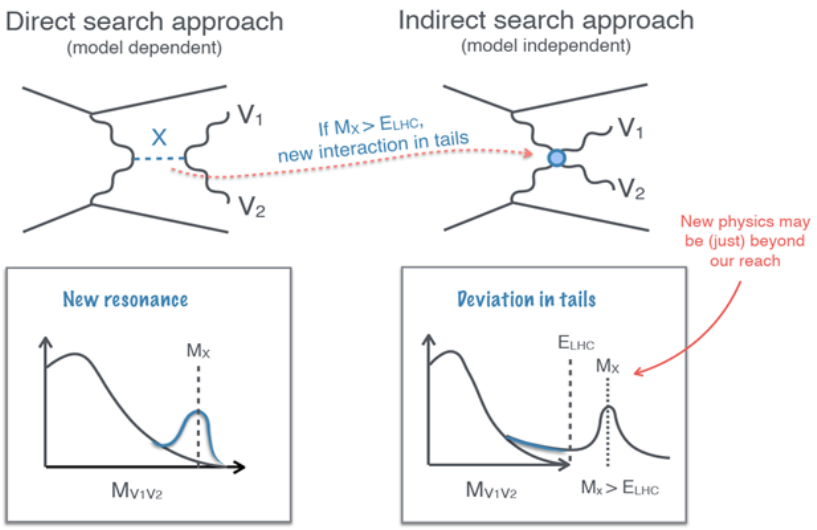

Fig. 85: Comparison of direct searches for a mass bump (left) and the EFT approach of searching for deviations in the tails of distributions (right), in the case of VBS [117].

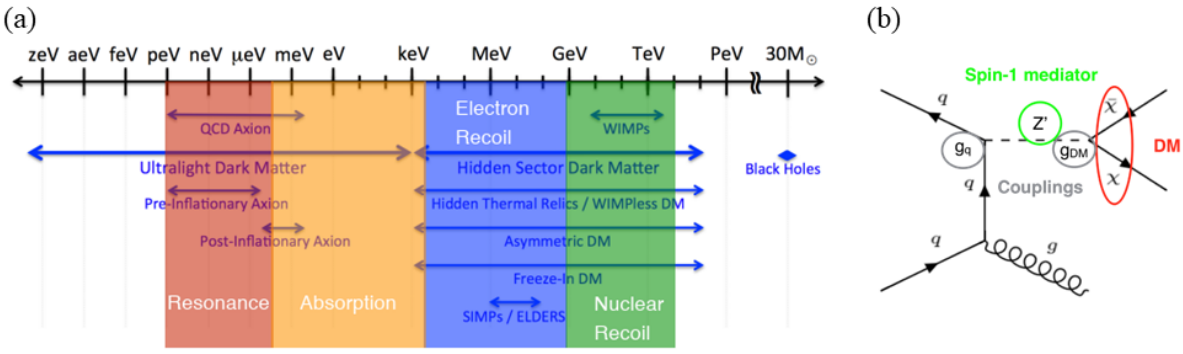

Fig. 86: (a) The many orders of magnitude in Dark Matter mass that need to be searched, with some relevant techniques superposed [118]; (b) example diagram coupling DM to SM particles via a mediator.

higher-order operators from SM fields: $\mathcal{L}_{\text{EFT}} = \mathcal{L}_{\text{SM}} + \sum c_i \mathcal{O}_i / \Lambda^2$.

The search for Dark Matter—assuming it is made of particles—is complicated by its unknown mass, resulting in an extremely wide range of masses to search, see Fig. 86 (a). If DM interacts with SM particles, it will do so through a mediator, as shown in Fig. 86 (b). Colliders offer a unique opportunity to study the mediator's properties (mass, spin). Simplified models describe dark matter without being constrained to a specific theory: $\sigma \propto g^2_{\text{SM}}\, g^2_{\text{DM}} / M^4_{\text{med}}$ [119]. Dark Matter is assumed to be weakly interacting, so it leaves no signal in the detectors. Instead one can identify DM production by looking for other particles recoiling against it, e.g. from initial-state radiation, as illustrated in Fig. 87 (a). Detailed understanding of the missing energy spectrum is crucial! Spurious detector signals can cause fake MET, so control regions are used to derive data-driven corrections to the background expectation.

An example of the results of a Dark Matter search is shown in Fig. 87 (b), for a monojet-W/Z search. No signal is seen, and limits are set—here on the DM mass vs mediator mass plane. A comparison (model-dependent) can be made to non-collider searches—direct detection at underground experiments—see Fig. 87 (c): the collider results are powerful in the low mass region.

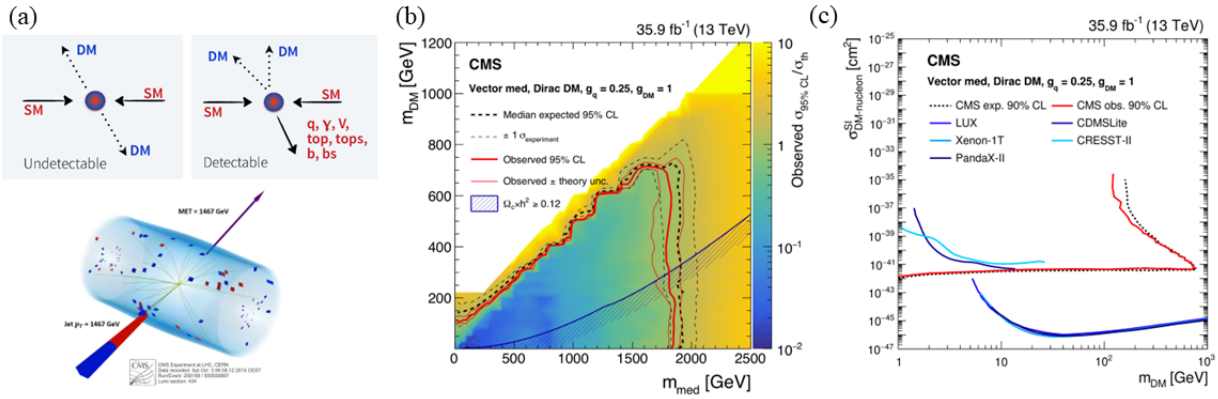

Fig. 87: (a) Searching for DM signatures, where recoil against SM particles is required for it to be visible, and (below) how such "monojets" appear in the experiment; (b) limits set on DM vs mediator mass; (c) comparison of limits on coupling vs mass with non-collider searches [120].

4.2 Hints of new physics?

Although no convincing BSM signal has been found in the searches, there has frequently been excitement when possible hints have been seen. A good example is the peak in the diphoton mass spectrum seen in the first 13 TeV data in 2015—like a heavy Higgs signal at a mass of around 750 GeV. The significance of the peak seen in ATLAS was 3.9 σ (local), 2.0 σ (global, i.e. accounting for the "look-elsewhere" effect), and a similar bump was seen by CMS, see Fig. 88! This would clearly have been new physics if it had been confirmed, and over 200 theory papers were published on its possible interpretation... but then the following year's data ruled it out—most likely it was a statistical fluctuation. While that excitement has passed, are there other hints that currently survive? I will discuss three so-called "anomalies".

(1) Flavour anomalies

The largest persisting indications of disagreement with the Standard Model that have been found so far at the LHC are known as the "flavour anomalies", seen by LHCb. The FCNC processes involving the transition $\mathrm{b} \to \mathrm{s}\ell^+\ell^-$ provide a rich set of observables to probe for new physics, as shown in Fig. 89 (a). There is a systematic failure of theory to describe the differential branching fractions at low momentum transfer q^2, or some of the angular distributions, see Fig. 89 (b).

Even more striking signals have been seen when comparing decay modes to electrons or muons. In the Standard Model gauge bosons have identical couplings with each of the three families of leptons, known as Lepton Universality. The decays $\mathrm{B}^+ \to \mathrm{K}^+\mu\mu$ and $\mathrm{B}^+ \to \mathrm{K}^+\mathrm{ee}$ are both decays of the form $\mathrm{b} \to \mathrm{s}\ell^+\ell^-$ and in the Standard Model they should occur with the same rate (apart from lepton mass effects, which are small here). Experimentally this is studied by making the double ratio with the resonant (via J/ψ) and non-resonant decays, as shown in Fig. 90 (a):

$$R_{\mathrm{K}} = \frac{\mathcal{B}(\mathrm{B}^+ \to \mathrm{K}^+\mu\mu)}{\mathcal{B}(\mathrm{B}^+ \to \mathrm{J}/\psi(\mu\mu)\mathrm{K}^+)} \Big/ \frac{\mathcal{B}(\mathrm{B}^+ \to \mathrm{K}^+\mathrm{ee})}{\mathcal{B}(\mathrm{B}^+ \to \mathrm{J}/\psi(\mathrm{ee})\mathrm{K}^+)} \quad . \tag{15}$$

Early results were surprisingly low, also for a similar channel with an excited kaon (K^*), see Fig. 90 (c).

A different hint of Lepton Universality violation has been seen in the decays $\mathrm{B}^0 \to \mathrm{D}^{(*)+}\ell\nu$, see Fig. 89 (c), this time comparing the modes with muons or tau leptons. Mass effects are larger here, so the

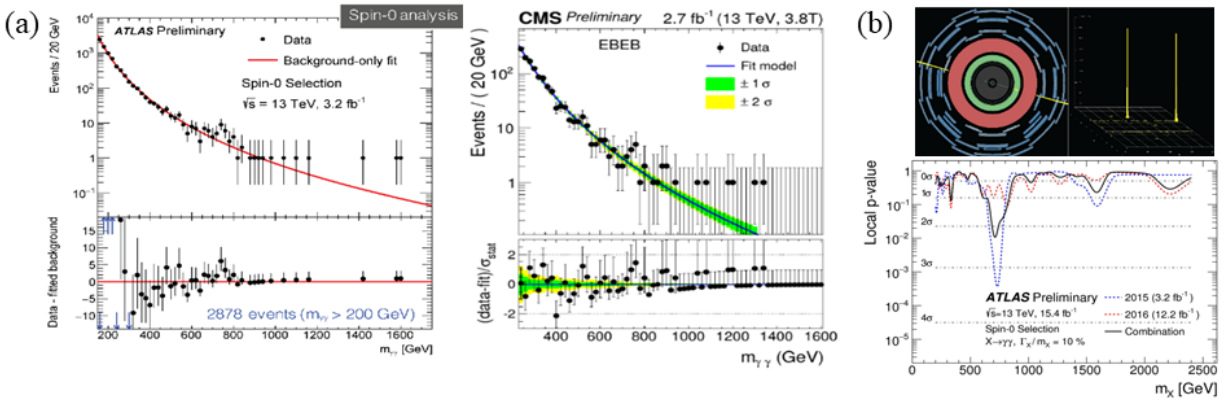

Fig. 88: Bumps seen in the $\gamma\gamma$ mass distribution in 2015 by ATLAS [121] (left) and CMS [122] (right); (b) event display showing the striking signature of such events (above) and evolution of the probability for a signal as the 2016 data was added (below) [123].

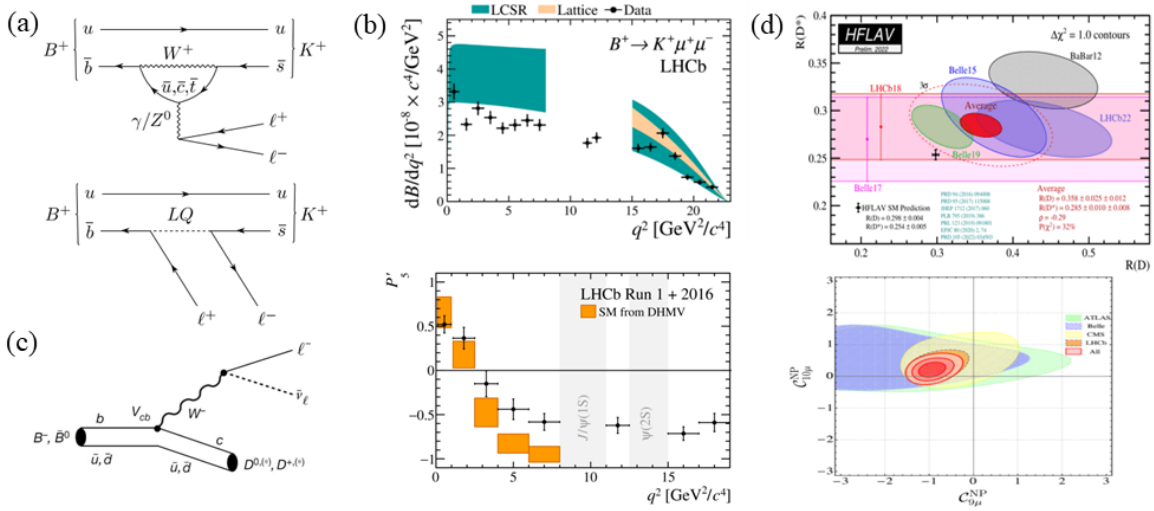

Fig. 89: (a) Diagrams for $\mathrm{b} \to \mathrm{s}\ell^+\ell^-$ decays in the SM (above) or for a model involving leptoquarks (below); (b) discrepancies seen in such decays vs the momentum transfer q^2 for the rate [124] (above) and one of the many angular distributions [125] (below); (c) tree diagram for $\mathrm{B}^0 \to \mathrm{D}^{(*)+}\ell\nu$; (d) combination of results on R_{D^*} vs R_{D} [126] (above) and of all anomalies vs coefficients for new physics [127] (below).

SM prediction is around 0.3. These are tree-level decays, so it would be surprising to see new physics. Similar ratios are constructed, known as R_{D} and R_{D^*}. The biggest discrepancy has been seen by BaBar, and combining all results as shown in Fig. 89 (d), the world average is 3.2 σ from the SM prediction.

Theorists have tried combining all such anomalies, finding *very* significant discrepancy with SM, as illustrated in Fig. 89 (d). However, the situation has evolved: in a recent publication LHCb has updated (and extended) its analyses of R_{K} and R_{K^*}, using improved analysis techniques. In addition to possible statistical fluctuations, a systematic correction was found due to underestimated hadronic misidentification background in the electron sample, giving the little green peaks under the signal visible in Fig. 90 (b)—highlighting the importance of systematic studies! The updated results are consistent with the Standard Model (see Fig. 90 (c)), so this element of the flavour anomalies has therefore gone away. The other flavour tensions with SM still remain to be understood, but the situation is less dramatic now.

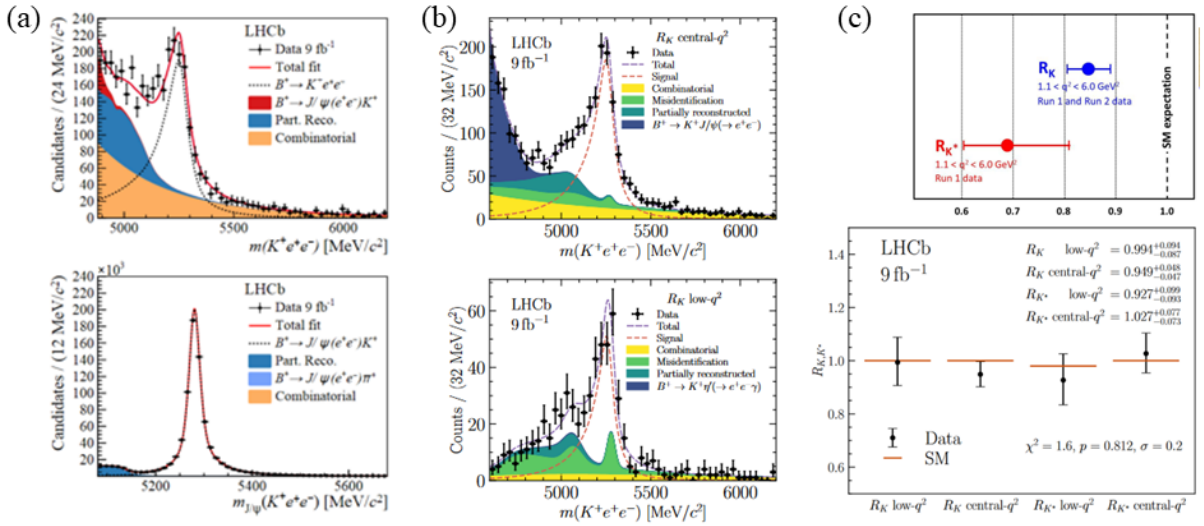

Fig. 90: (a) Signals for $\mathrm{B}^+ \to \mathrm{K}^+\mathrm{ee}$ (above) and $\mathrm{B}^+ \to \mathrm{J}/\psi(\mathrm{ee})\mathrm{K}^+$ (below)—the equivalent peaks in the $\mu\mu$ channels are much cleaner [128]; (b) updated signals for $\mathrm{B}^+ \to \mathrm{K}^+\mathrm{ee}$ in two regions of q^2; (c) early indication of discrepancy for $R_{\mathrm{K}^{(*)}}$ [129] (above) and from the updated analysis (below) [130].

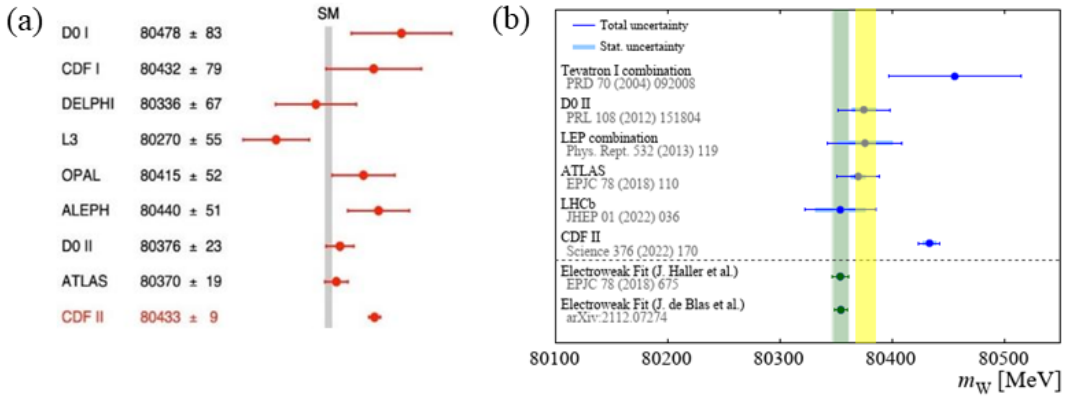

Fig. 91: W mass (a) comparison of the new result from CDF (at bottom) with earlier measurements; (b) the same data, including a recent LHCb result and superimposing the average of previous measurements (yellow band; citations for the results are given in the figure).

(2) W mass anomaly

A new CDF result for m_{W} was released last year, with 0.01% precision. It uses entire dataset collected from the Tevatron collider at Fermilab, based on 4.2 million W boson candidates (about four times the number used in the previous CDF analysis, published in 2012). The result shows an impressive discrepancy with the SM expectation from EW fits, at level of $7\,\sigma$, see Fig. 91. However, the result is also in significant tension with the average of previous measurements from LEP, LHCb, ATLAS, and D0. Misunderstanding of the proton structure or QCD corrections could manifest differently depending on the centre-of-mass energy, $\mathrm{p\overline{p}}$ *vs* pp collisions, or different analysis choices, so it would be prudent to wait and see if this anomaly persists once the consistency between the experiments has been clarified.

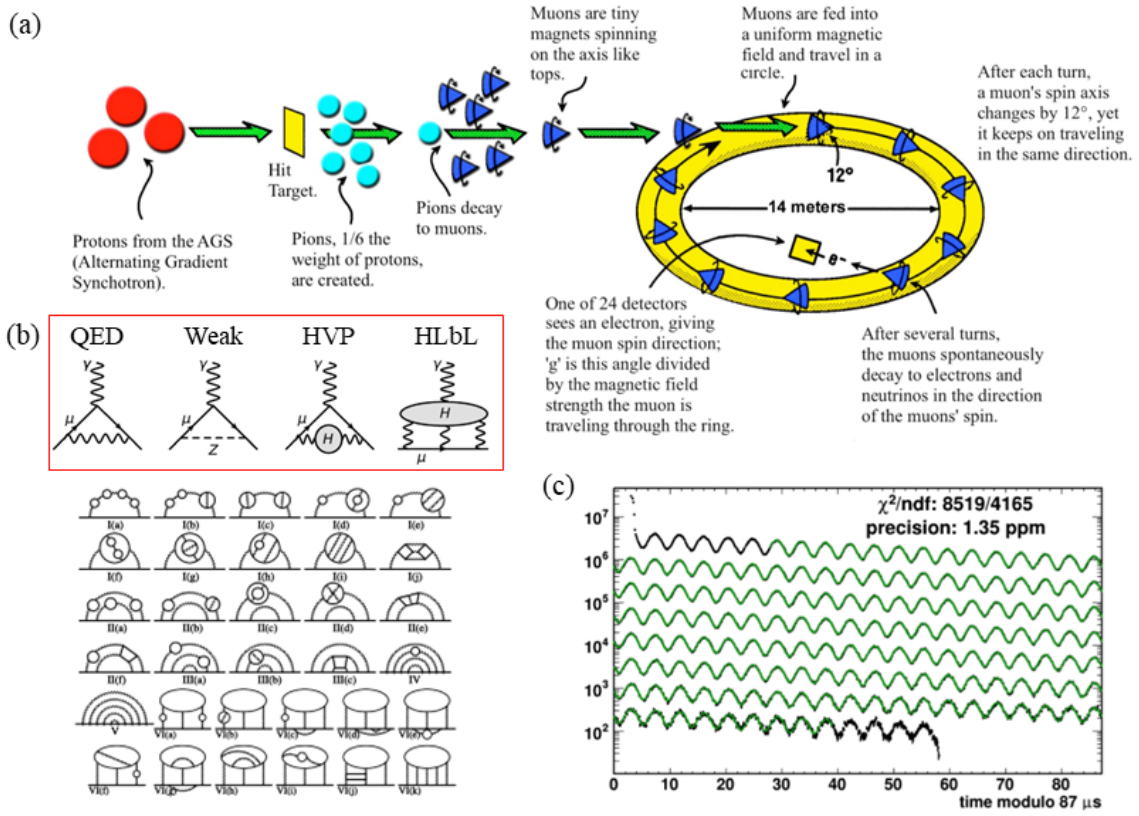

Fig. 92: (a) Sketch of the principle of the muon $g-2$ experiment; (b) the four contributions to the muon anomalous magnetic moment (in box) and examples (here 5-loop) of diagrams calculated for the QED contribution [132] (below); (c) oscillations of the muons' spin, seen in their decay rate to detected electrons [131].

(3) $g-2$ anomaly

An elementary particle with intrinsic angular momentum (spin, $\boldsymbol{s}$) and charge q has magnetic moment:

$$\boldsymbol{\mu} = g\frac{q}{2m}\,\boldsymbol{s} \quad , \tag{16}$$

where g is the gyromagnetic ratio and m is the mass of the particle. Dirac predicted $g=2$ at tree-level, but this receives corrections from virtual particles in loop diagrams, increasing the value. The resulting "anomalous magnetic moment" of the different leptons ℓ is given by $a_\ell = (g_\ell - 2)/2$. Their measurement are long-standing precision tests of the Standard Model:[42]

- **electron**: $a_\mathrm{e} = 0.001\,159\,652\,180\,7 \pm 3$ measured to 0.24 ppb!
  SM: $0.001\,159\,652\,182\,0 \pm 7$ —prediction agrees, a triumph for QED!
- **muon**: $a_\mu = 0.001\,165\,920\,6 \pm 4$ measured to 0.37 ppm,
  SM: $0.001\,165\,918\,1 \pm 4$ —prediction is close but doesn't quite agree!
- **tau**: $a_\tau = -0.018 \pm 0.017$ —difficult to measure due to its short lifetime,
  SM: $0.001\,177\,21 \pm 5$.

[42] The errors quoted here are the uncertainties on the *last digit* of the measured values, except for a_τ.

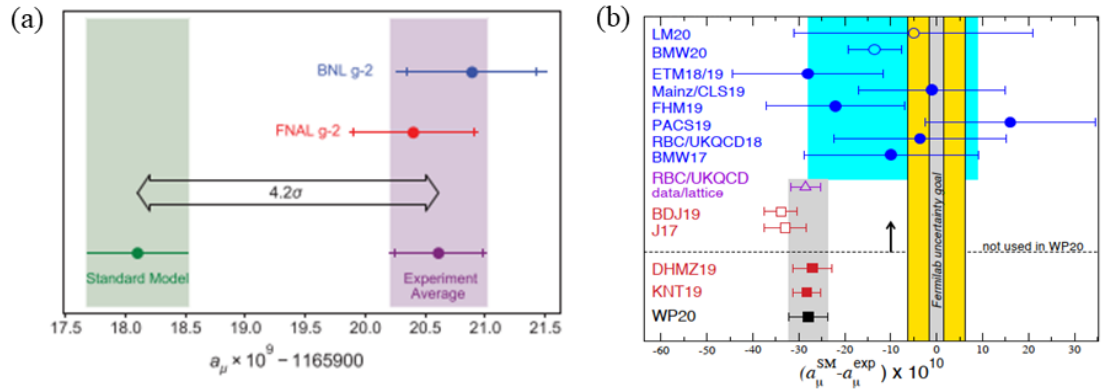

Fig. 93: (a) Comparison of the most recent experimental values and the SM prediction for a_μ [133]; (b) new calculations of the HVP contribution to a_μ, that were not included in the SM prediction shown in (a) (referred to in this plot as as "WP20") [134].

There are many contributions to the prediction of a_μ, classified as QED, Weak, Hadronic Vacuum Polarization, and Hadronic Light-by-Light (see the box in Fig. 92 (b)). Their relative contributions to the overall value are as follows (in parentheses, in units of 10^{-12}) followed by their contributions to the uncertainty on the prediction: QED (116584719) 0.001 ppm, Weak (154) 0.01 ppm, HVP (6845) 0.37 ppm, HLbL (92) 0.15 ppm. Although the QED contribution is the largest, it is extremely well known, and an example of a few of the many diagrams that have been calculated are shown in Fig. 92 (b)—an amazing amount of work!

The first result was published by a new Fermilab experiment last year for the measurement of the muon $g-2$, using the technique sketched in Fig. 92 (a),[43] involving the measurement of many oscillations of the muons' spin, as shown in Fig. 92 (c). It is in excellent agreement with the previous experiment (at BNL), and confirms the discrepancy with the SM prediction, currently at $4.2\,\sigma$ significance, see Fig. 93 (a). However, there are new calculations of the most uncertain part of the prediction (HVP) from Lattice QCD, see Fig. 93 (b), which would reduce the discrepancy—the theory community are working to understand this tension between predictions, to consolidate the comparison with experiment.

4.3 Widening the search

No convincing hints of physics beyond the Standard Model have been seen so far at the LHC—but could we be missing the evidence for new particle decays?[44]

Long-lived particles (LLP)

Most searches share a similar basic reconstruction of tracks, requiring them to originate from close to the IP: even the b-quarks only travel a few mm before decaying. A wide variety of lifetimes is seen for SM particles, as shown in Fig. 94 (a)—perhaps this is also the case for the Dark Sector? Requiring the track to originate near to the IP could miss BSM particles with long lifetimes, for which there are plenty of theoretical predictions: Split Supersymmetry, Gravitino Dark Matter, Hidden Valley, etc. Such SM extensions predict particles that travel $\sim$metres with lifetime of hundreds of ns, or that lose so much

[43] Note that strictly speaking this is a storage ring, rather than collider, experiment.
[44] This field of study is a breeding ground for three-letter acronyms: FIPs, HIPs and LLPs...

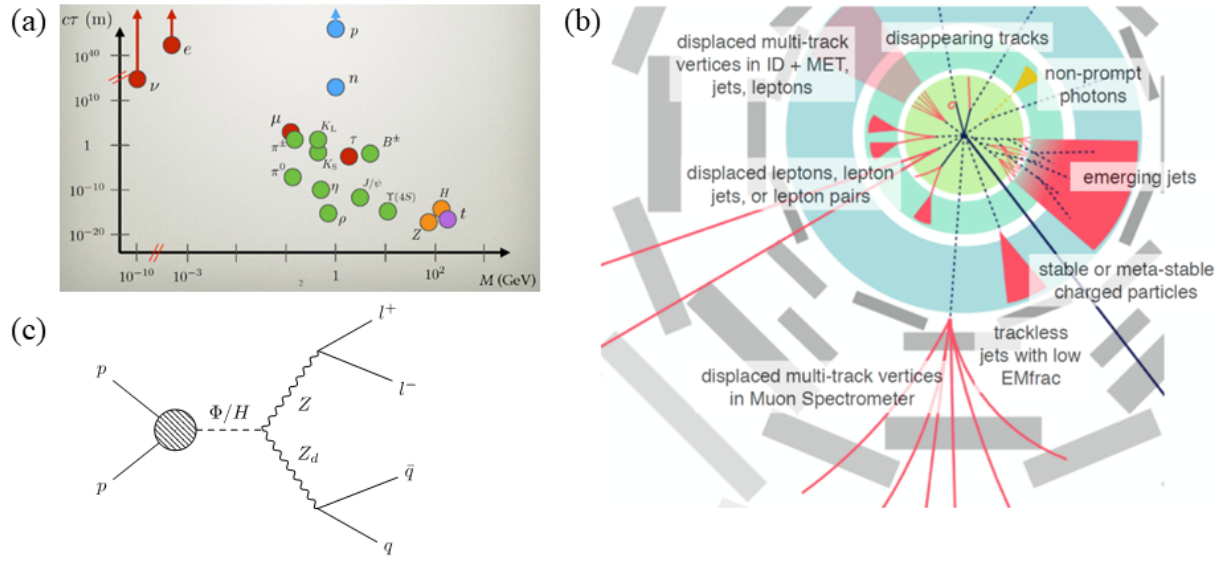

Fig. 94: (a) Lifetime vs mass for particles in the SM; (b) the many possible signatures of long-lived particles [135]; (c) diagram for a decay in a dark-sector model with additional dark gauge symmetry, giving an LLP candidate, Z_d.

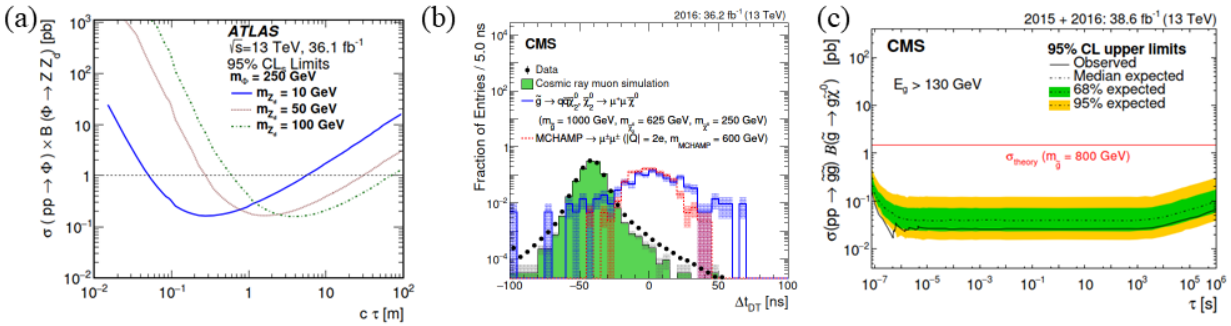

Fig. 95: (a) Limit on cross-section $\times$ branching ratio vs $c\times$ lifetime in the Z_d LLP search [136]; (b) search for stopping LLPs showing the muon-pair time difference, where the out-of-time background from cosmic rays is visible; (c) resulting limit for the stopping LLP search vs lifetime [137].

energy that they would stop somewhere in the detector and decay later. The challenge for experiments is that they need to change triggering strategy and object reconstruction to be sensitive for such decays! They can look for energy deposits in the calorimeter with no track pointing to it; large energy loss dE/dx; time of flight less than the speed of light, etc., i.e. signature-driven searches, see Fig. 94 (b).

An example is the search for a Z + single neutral LLP, a popular scenario in dark-sector models with additional $U(1)_d$ dark gauge symmetry, see Fig. 94 (c). The experimental signature is that the Z_d decays within the Hadron calorimeter, jets give little deposits in the ECAL and there are no charged tracks pointing to the PV. This corresponds to decay lengths for the Z_d between a few cm and tens of metres. The Z_d jet selection requires no track with $p_T > 1$ GeV and uses jet timing. No excess was observed, so limits have been set as shown in Fig. 95 (a).

Heavy (~ 100 GeV) LLPs will lose kinetic energy and stop while traversing the detector. If these stopped LLPs have lifetimes greater than tens of ns their decays will be reconstructed as separate events from the beam crossing where they were produced—most easily identified when there are no proton

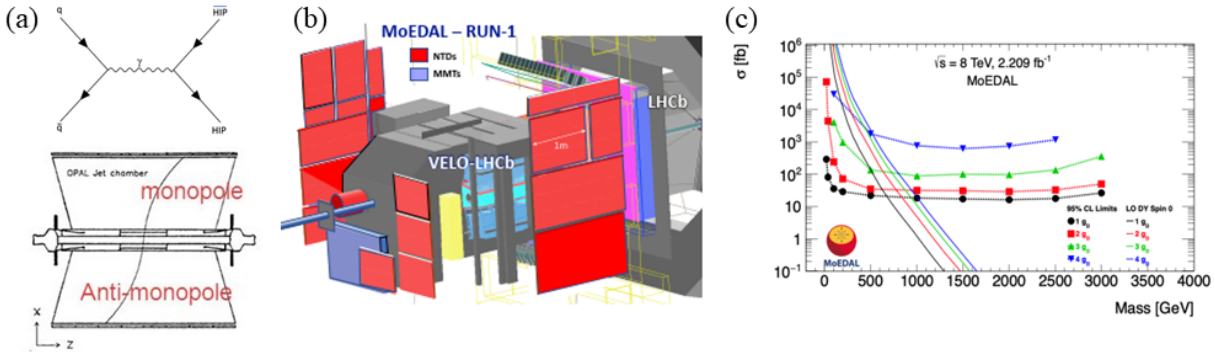

Fig. 96: (a) Diagram for pair-production of highly ionising particles (above) and simulation of magnetic monopoles in a solenoidal collider experiment (below); (b) the NTDs of MoEDAL (shaded red) surrounding the LHCb IP; (c) limits on highly ionising particle production *vs* mass [138].

bunches in the detector. A search is made for out-of-time (with respect to the bunch crossing) deposits in the HCAL or muon pairs in the muon detector. Backgrounds are from cosmic rays, beam-halo and detector noise, as shown in Fig. 95 (b). Limits are set on the lifetime from 100 ns to 10 *days*, see Fig. 95 (c).

Highly ionizing particles (HIP)

Magnetic monopoles are a prime example of this type. They would make Maxwell's equations more symmetric, but aren't found in normal matter—if you break a magnetic dipole (e.g. a bar magnet), you get two more (smaller) dipoles. Dirac (1931) formulated a consistent description of the magnetic monopole within the framework of quantum physics, related to the quantization of charge: if any magnetic monopole exists then the electric charge is quantized in units of $e = 2\pi\hbar/(\mu_0\, g_{\rm D})$, where $g_{\rm D}$ is the magnetic charge and μ_0 is the permeability of free space. The value of $g_{\rm D}$ is $\approx 68.5\, e$—so such objects would be very highly ionizing. Monopoles might be pair-produced at colliders: this would give rise to unusual tracks, parabolic along the axis of the solenoid field, as illustrated in Fig. 96 (a).

MoEDAL is a small experiment at the LHC dedicated to this type of search. It uses plastic foils that form Nuclear Track Detectors (NTD), deployed around the LHCb VELO as a passive detector (see Fig. 96 (b)). HIPs would leave ionization trails in the plastic, revealed as large holes when etched after exposure to the beam. Aluminium blocks are also deployed to *trap* monopoles: the material samples are then passed through superconducting SQUID magnetometers to look for the induced non-decaying current that would result from a transported monopole. No monopole candidates have been found, and limits are set as illustrated in Fig. 96 (c).

Feebly interacting particles (FIP)

Weakly Interacting Massive Particles (WIMPs) have long been a popular candidate for Dark Matter: with mass in the few $\times$ 100 GeV range and an interaction strength like the weak force, they would be produced thermally in the Big Bang with the right abundance—many searches have been made, but have not found them so far. However, there could be other Dark Matter candidates with lower mass (MeV–GeV) and weaker coupling, such as the Dark Photon (A′) that would have a long lifetime and decay to $\rm e^+e^-$. FASER is a new small experiment at the LHC to search for such feebly interacting particles. They are studying the "intensity frontier" at the LHC: since most light hadrons are produced along the beam axis in the big experiments, perhaps other light new physics particles are too? The FASER experiment

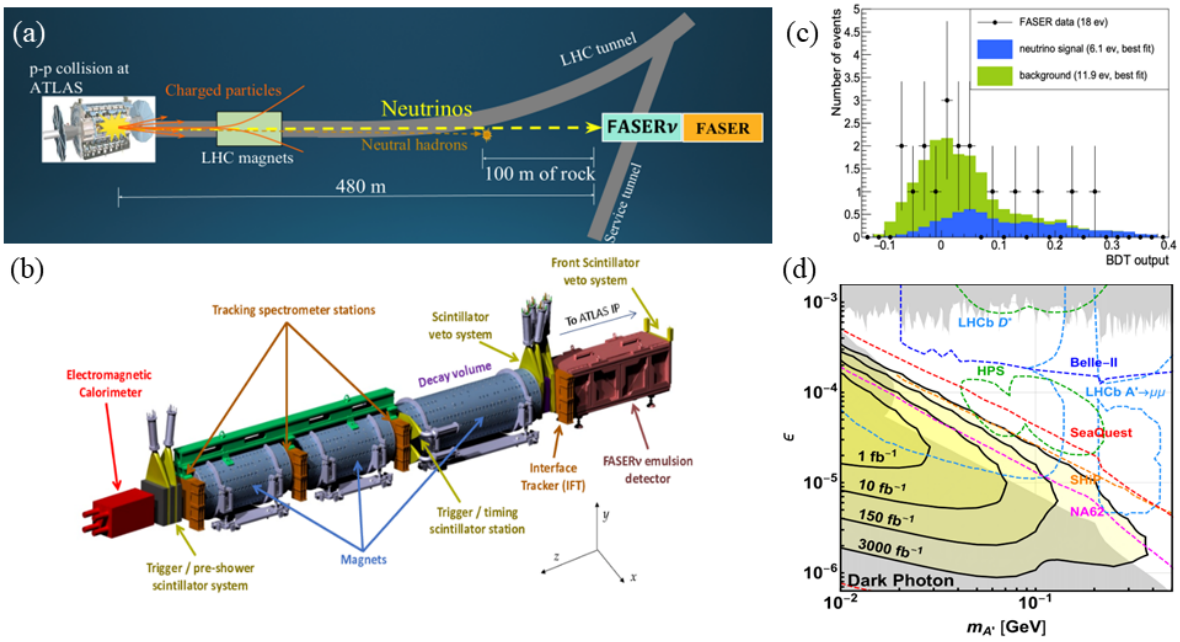

Fig. 97: (a) Location of FASER at 480 m from the ATLAS IP; (b) schematic of the FASER detectors; (c) signal seen in the prototype emulsion detector, showing a hint for neutrinos from the LHC [139]; (d) sensitivity curves for the dark photon as a function of integrated luminosity, in the plane of coupling *vs* mass [140].

is situated $\sim$500 m from the ATLAS collision point, on the beam collision axis line-of-sight, in an unused former service tunnel. A small spectrometer has been installed to detect the close e^+e^- tracks, see Fig. 97, with an emulsion detector added in front to detect neutrinos: FASERν (covering $\eta > 9$). Neutrinos produced in the pp collisions of the LHC will also be mostly in the forward direction, and can be detected by FASER in that additional detector, allowing another test of the Standard Model. The first candidate collider neutrino events have been seen in a prototype of the emulsion detector, see Fig. 97 (c).

SND is a similar detector on the opposite side of ATLAS, but slightly off axis ($7.2 < \eta < 8.4$), which enhances the neutrinos coming from heavier hadron decays such as charm. FASER and SND are making good progress, but the access tunnels where they are sited are too small to exploit the full physics potential in the forward region of the LHC. A new shaft has been proposed to be dug 620 m from the ATLAS interaction point, with a 65 m-long underground cavern to host more and larger experiments. At the moment there are five proposed experiments to be situated in this "Forward Physics Facility", with different capabilities and covering different rapidity regions. However, the facility is not yet approved, and a decision on it will probably only be taken in a few years' time.

Physics Beyond Colliders

The LHC (including its future HL-LHC phase) is the flagship of the CERN programme, providing data at the energy frontier for the next 20 years. A future collider should follow after the LHC, but most likely not before the mid-2040s. The Physics Beyond Colliders study [141] was initiated to maintain a diverse physics programme at CERN, help to fill gaps between colliders: using the injector complex at CERN for fixed-target physics at the intensity frontier—searching for rare or weakly-coupled physics with high intensity beams. A current example of such experiments is NA62, that searches for the decay

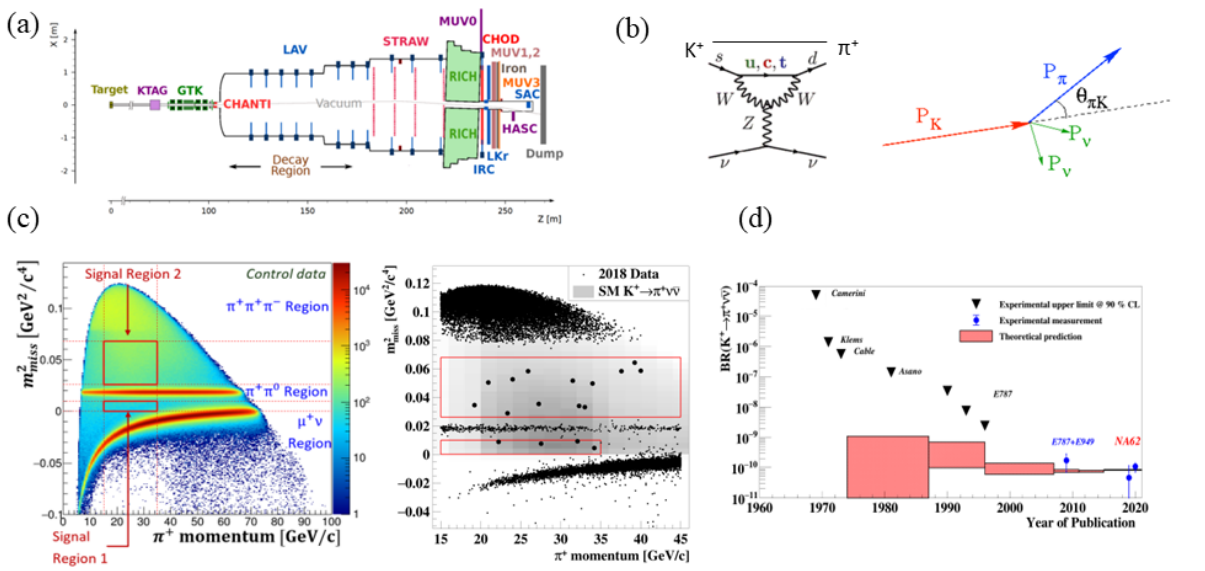

Fig. 98: (a) Layout of the NA62 spectrometer; (b) the penguin diagram responsible for the $K^+ \to \pi^+ \nu\overline{\nu}$ decay in the SM (left) and the signature in the experiment (right); (c) the definition of signal regions in the plane of missing mass squared vs pion momentum (left), and the 2018 data (right); (d) the evolution of the experimental limit (arrows) and theoretical prediction (pink shaded) for this decay mode over the years, showing the recent evidence for its discovery [142].

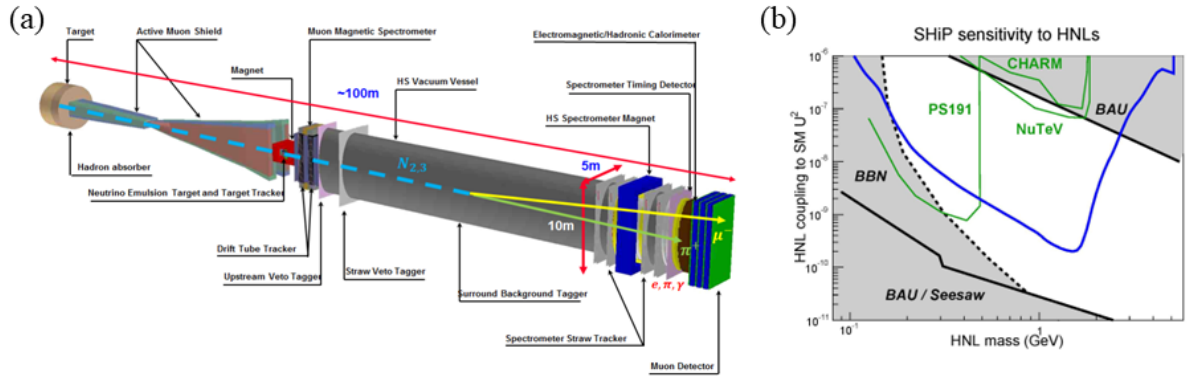

Fig. 99: (a) The proposed SHiP spectrometer, with a decay of an HNL illustrated; (b) sensitivity of SHiP to HNLs in the plane of coupling vs mass [143].

$K^+ \to \pi^+ \nu\overline{\nu}$ at the SPS, see Fig. 98. This is a very rare decay ($\mathcal{B}_{\rm SM} \sim 10^{-10}$) but is precisely predicted in the SM: another good place to look for new physics in loop diagrams. The signal is a single charged track in the final state: an intense beam containing K^+ is used to study the missing mass in the decay due to the neutrinos. Evidence for the decay has recently been seen, as shown in Fig. 98 (d), in agreement with the SM expectation. When the NA62 experiment is completed at the end of Run 3 (in 2025) there will be the opportunity to upgrade the intensity of the beam-line and either extend the study of kaon physics (proposal HIKE) or make a beam-dump to search for new physics such as Heavy Neutral Leptons (at the proposed SHiP experiment or a competing off-axis proposal, SHADOWS). This intensity upgrade has recently been strongly supported by the CERN Research Board[45]—approval is expected by end of this year.

[45] In a meeting that was held in the same week as this school took place.

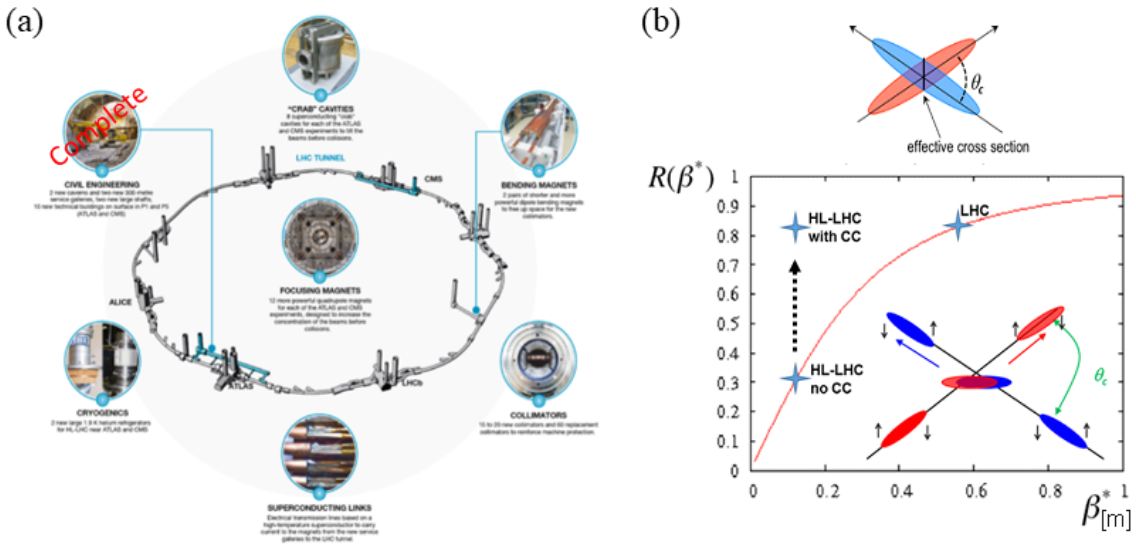

Fig. 100: (a) Modifications required to the LHC machine for its high luminosity upgrade; (b) sketch of the reduced overlap of bunches due to the crossing angle (above) and its influence on luminosity (below), with the loss being recovered by rotating the bunches using crab cavities (insert) [145].

The Standard Model was originally written down without right-handed neutrinos (the neutrinos were assumed to be massless). The discovery of neutrino oscillations implies that they must be massive, and introducing right-handed sterile partners could help to explain dark matter and the baryon asymmetry of the Universe: such sterile neutrinos are referred to as Heavy Neutral Leptons (HNL). SHiP is a proposed experiment to search for these and other dark-sector particles, via a beam-dump at SPS, see Fig. 99.

4.4 Future colliders

Having a diverse programme of experiments at lower energy is important, but it still remains the case that much of recent progress in particle physics has been driven by colliders. The long term strategy for particle physics in Europe (and at CERN) is decided in a process that takes place about every six years: the European Strategy for Particle Physics (ESPP), for which the latest update was in 2020. There is a similar consultation in the Americas known as the Snowmass process, that is currently in progress and is expected to report soon. Clear priorities were set in the latest European strategy update [144]:

1. Full exploitation of the LHC (including its **HL-LHC** phase: discussed here as a future collider);
2. The next collider after the LHC should be an $\mathrm{e^+e^-}$ **Higgs Factory**;
3. The long-term future of European particle physics should be a collider at the **energy frontier** with $E_{\mathrm{CM}} \geq 100\,\mathrm{TeV}$.

HL-LHC

This is an approved upgrade of the LHC to increase its luminosity to 5 (or even 7) $\times 10^{34}\,\mathrm{cm^{-2}s^{-1}}$. The beam energy will not be changed very much, although it may be pushed up to reach the design value of 14 TeV in the centre-of-mass, or just beyond (currently the LHC runs at 13.6 TeV). Significant changes

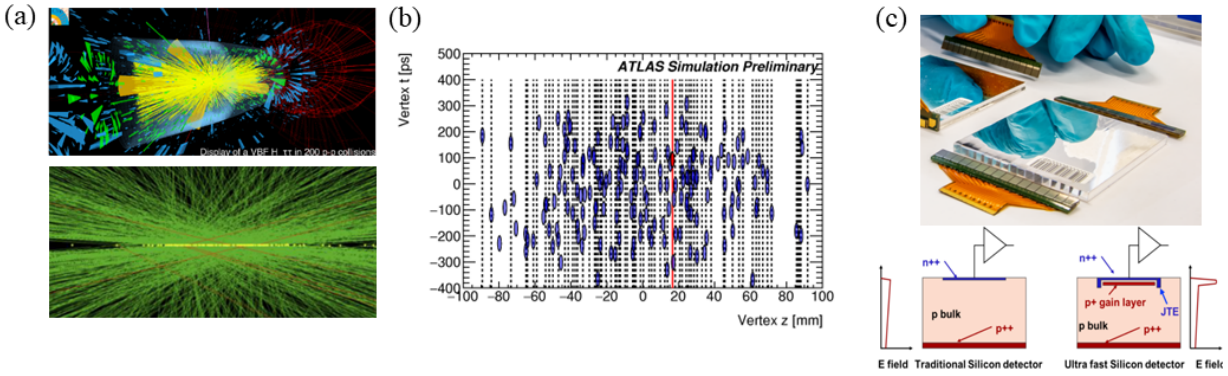

Fig. 101: (a) Event display of a high-pileup event at HL-LHC (above) and the dense track occupancy in the vertex region (below, shown in the view along the beam axis); (b) separating those pileup vertices in the plane of time vs position [146]; (c) components of the CMS timing layer, scintillating bars for the barrel (above) and the principle of LGAD operation, used in the endcap (below) [147].

need to be made to the LHC machine, as presented in Fig. 100 (a), and good progress is being made, to be ready in 2029 and to run until 2042, integrating a total of 3000 fb^{-1}/experiment, i.e. over 10 $\times$ the current sample. The luminosity is increased with stronger focusing at the interaction points, using 12 T inner-triplet magnets that require use of new superconductor, Nb_3Sn. The resulting low β^* requires a larger beam crossing angle, would reduce luminosity by factor R shown in Fig. 100 (b). To avoid this the bunches will be rotated so that they collide head on, using RF manipulation in so-called crab cavities.

The increased luminosity will lead to an increase in pileup to $\sim$200 overlapping interactions, and increased radiation, so the experiments also need to be upgraded (or their life would become hard, see Fig. 101 (a)). For ATLAS and CMS these are known as their Phase-2 upgrades, which are already designed and are now moving into production: they include new silicon pixel detectors, trackers, the HGCAL, etc. To combat the pileup, *fast timing* is a key ingredient: as the bunches pass through each other, collisions occur at different *times* as well as positions, as shown in Fig. 101 (b). Pileup can be reduced by cutting on both the vertex z-position and the vertex time t: this is known as "4D vertexing", (x, y, z, t). Timing layers are being added by both ATLAS (in the endcaps only) and CMS (both in the endcaps and barrel) as part of their Phase-2 upgrades.

As an example, the components of the MIP Timing Detector (MTD) of CMS are illustrated in Fig. 101 (c): the barrel will be instrumented with scintillator bars, and the endcaps with fast silicon detectors. The technology is selected according to the requirements: both detectors cost $\sim$ 10 MCHF, but the barrel scintillators cover 3 $\times$ the area of the endcap detector with 25 $\times$ fewer channels; on the other hand, they would not be able to handle the 10 $\times$ higher radiation in the endcap. The fast scintillators used for the barrel are LYSO crystals (Lutetium Yttrium Orthosilicate), with excellent radiation tolerance, high light yield ($\sim$40,000 photons/MeV), fast scintillation rise-time (< 100 ps), and relatively short decay-time ($\sim$40 ns). 166k LYSO crystals are readout with SiPMs at each end attached to the inner wall of tracker support tube (radius = 1.15 m, length = $\pm$2.6 m). Their expected time resolution will be 35 ps at the start, degrading to about 60 ps at end of the HL-LHC run. This will also enable time-of-flight particle ID as a bonus, with 2 σ K-π separation up to $p \sim 2$ GeV/c. The endcaps will use LGAD (Low-Gain Avalanche Diode) silicon detectors, with internal gain. LGADs can achieve 30 ps resolution, but this

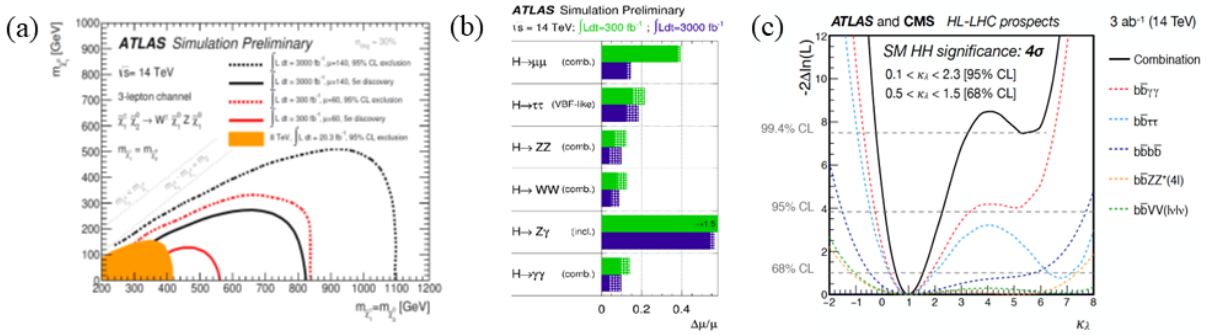

Fig. 102: HL-LHC prospects (a) the increased sensitivity in a Supersymmetry search [148]; (b) the expected improvement in precision on the Higgs boson couplings [149]; (c) combined sensitivity of ATLAS and CMS to the Higgs self-coupling [6].

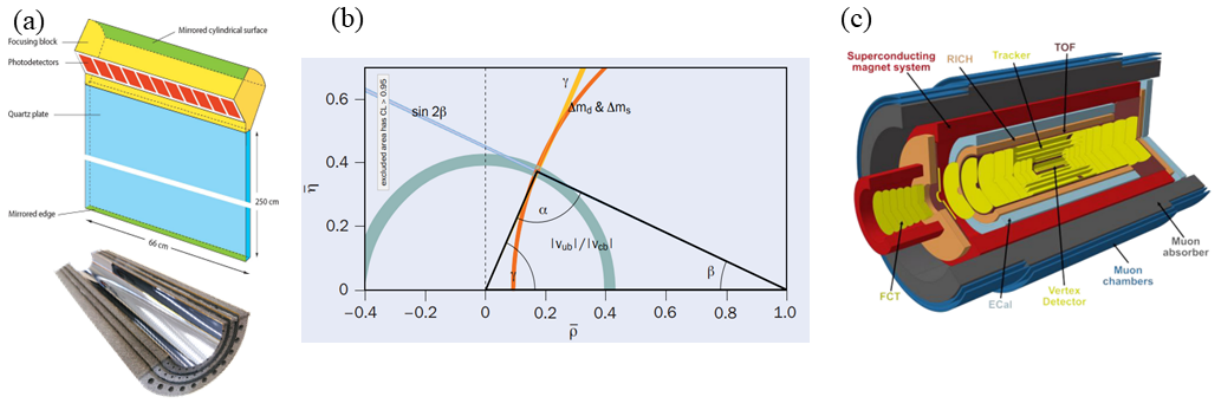

Fig. 103: LS4 upgrades: (a) a module of the proposed fast time-of-flight detector for LHCb [150] (TORCH, above) and lightweight silicon detector for ALICE (using silicon wafers bent into a cylinder, below); (b) the prospects for the Unitarity Triangle constraints on flavour physics from LHCb Upgrade II (worth comparing to the current status that was shown earlier in Fig. 64 (b)) [84]; (c) the proposed layout of ALICE3 [151].

degrades with radiation dose, so they may need to be replaced during the run.

Concerning the physics prospects for HL-LHC, if any new physics signal is seen in Run 3 it will allow the first detailed exploration with a well understood machine and experiments. Otherwise it will extend the direct discovery potential by 20–30% in mass reach, see Fig. 102. In either case, over 100 million Higgs bosons will be produced, allowing the Higgs couplings to be measured to a few percent including to the 2$^{\text{nd}}$ generation via $\text{H} \to \mu^+\mu^-$, plus providing first sensitivity to HH production and the Higgs self-coupling.

LHCb and ALICE have just been upgraded for Run 3, so their future upgrades will be on a longer timescale than those of ATLAS & CMS. They plan upgrades to make use of the high luminosity available at HL-LHC, to be installed during Long Shutdown 4 (LS4), currently scheduled in ten years' time (2033-34), so there is still time for interesting R&D. LHCb is planning to make use of fast timing, e.g. 4D tracking in the VELO and a novel time-of-flight system shown in Fig. 103. They aim to record 300 fb^{-1} of data, leading to greatly improved precision on flavour observables. ALICE is planning a radical all-new experiment (ALICE3) for their upgrade in LS4. They intend to replace their TPC with an extremely

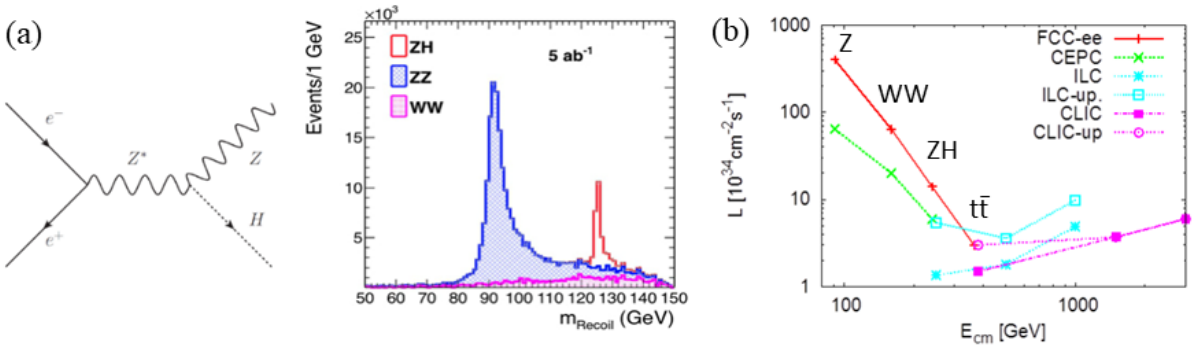

Fig. 104: (a) Diagram for the Higgstrahlung process (left) and simulation of the recoil mass spectrum in FCC-ee; (b) luminosity (on a logarithmic scale) *vs* centre-of-mass energy for the different Higgs Factory proposals [152].

light-weight silicon tracking system, and run at higher rate. These are exciting ideas, but they first need to be approved (after checking that sufficient funding is available).

Higgs Factory

Now that the Higgs boson has been discovered, the highest priority future collider is an e^+e^- Higgs Factory, to study it in great detail. There are four (at least) implementations under discussion, none of them approved yet. All target associated production $e^+e^- \to ZH$ "Higgstrahlung" shown in Fig. 104, which will allow unbiased Higgs boson properties to be measured by selecting the Z decay and looking at everything that recoils against it, sensitive to possible invisible Higgs decays. The main choice to be made is between a linear or circular collider geometry: linear colliders are better at high energy, circular at low energy, while their performance is quite similar at the energy for ZH (240 GeV). The linear options are the ILC (in Japan) or CLIC (CERN), see Fig. 105, and circular FCC (CERN) or CEPC (China), see Fig. 106.

1. **ILC** (International Linear Collider): a mature technology, discussed for over 20 years, based on superconducting niobium RF cavities at 1.3 GHz frequency giving an accelerating gradient $\sim$35 MV/m; two separate linacs for e^+ and e^- beams, with a single IP; baseline 250 GeV (30 km), upgradable to 1 TeV; a possible site has been selected in Japan, but there has been no recent progress towards approval from the Japanese government.
2. **CLIC** (Compact Linear Collider): normal conducting cavities allow for a higher frequency of 12 GHz, leading to higher gradient $\sim$100 MV/m; different stages considered—380 GeV (11 km) up to 3 TeV (50 km)—and could be sited in the CERN region; two-beam acceleration system with a low-energy high-current drive beam powering the RF cavities of the main linac.
3. **FCC** (Future Circular Collider): feasibility of a 91-km circular tunnel is under study at CERN—it could be ready (technically) by around 2045; it will make use of developments made for the B Factories, such as continuous injection, leading to enormous luminosity possible at low energy—running on the Z could repeat whole of the LEP programme in a few minutes, integrating 10^{12} Z decays, and over 10^6 Higgs bosons; possibility of 4 IPs, allowing 4 experiments.
4. **CEPC** (Circular Electron Positron Collider): proposed in China, with very similar design to FCC.

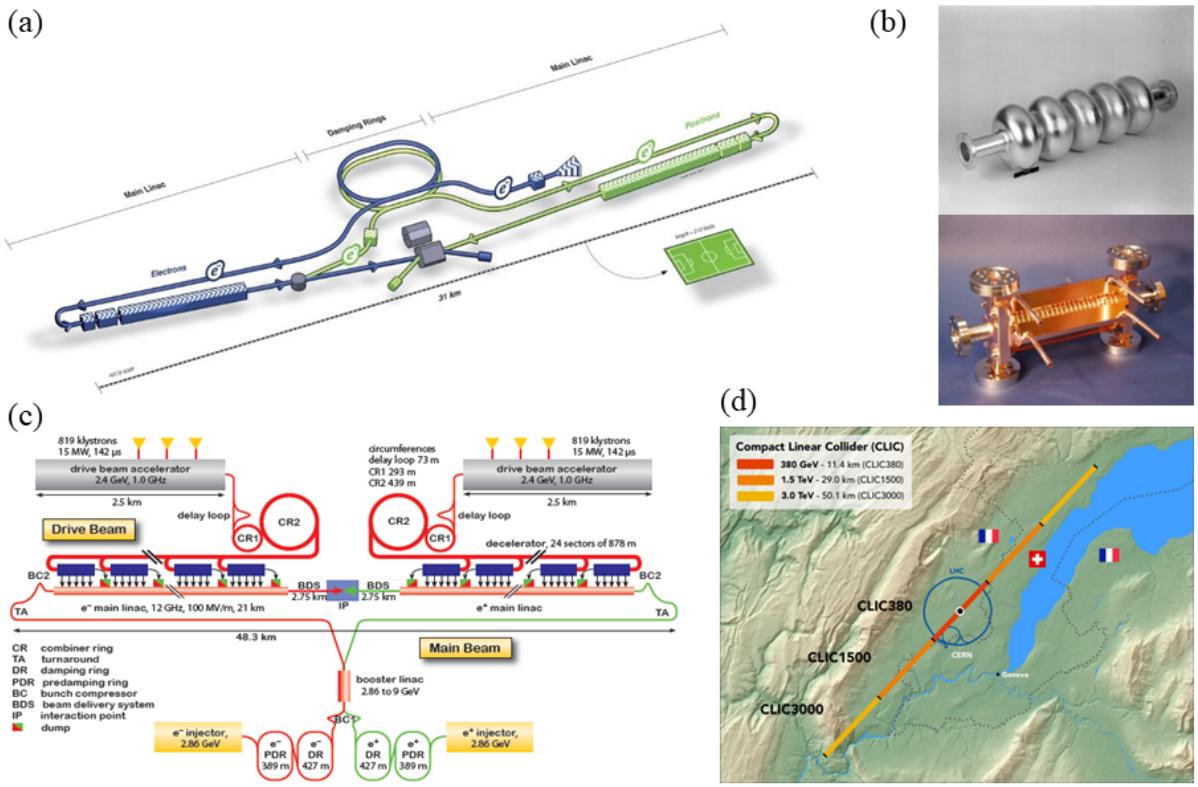

Fig. 105: (a) ILC layout [153]; (b) accelerating structures for the ILC (above) and CLIC (below); (c) CLIC layout [154]; (d) possible siting of CLIC in the CERN region.

From a CERN perspective, CLIC (or ILC technology) is kept as a backup in case FCC turns out to be too expensive (estimated ~ 11 BCHF for the first phase, FCC-ee). Experiments for an e^+e^- Higgs Factory are similar to those used at LEP, but aiming for higher precision: radiation and pileup are less severe than at the LHC, see Fig. 107. Common developments are being discussed between the different proposed facilities. At FCC-ee it is expected to measure Higgs couplings to better than 1%, m_W and m_Z to < 1 MeV, m_t to < 20 MeV from a threshold scan, etc. HH production is only directly accessible at higher energy. An example of R&D towards a future Higgs factory experiment—that I am working on now—is the adaptation of a twin-radiator RICH (similar to the original design in LHCb) to a 4π detector at a Higgs Factory, such as FCC-ee, aiming to be as compact (20 cm in radial thickness) and lightweight (5% of X_0) as possible, see Fig. 106 (c).

The use of s-channel production might appear attractive for studying the Higgs (i.e. setting $E_{CM} = m_H$, in a similar way to $e^+e^- \to Z$ at LEP) but it is tough: the cross-section is low and Γ_H (4 MeV) $\ll$ the beam energy spread (100 MeV), see Fig. 108 (a). FCC-ee might just be able to measure it, with dedicated running over a few years, as shown in Fig. 108 (b). One might consider trying to use muons instead of electrons for this, as their higher mass would give a larger cross-section. Muon Colliders are being studied, see Fig. 108 (c), but the statistics in the s-channel would still be lower than for $e^+e^- \to ZH$, plus the design is complicated: muons decay, giving severe background in the detector. This may be an option for the longer-term, though, as a Muon Collider could reach high energy.

Sustainability is an important consideration for future colliders: accelerators need to be powered

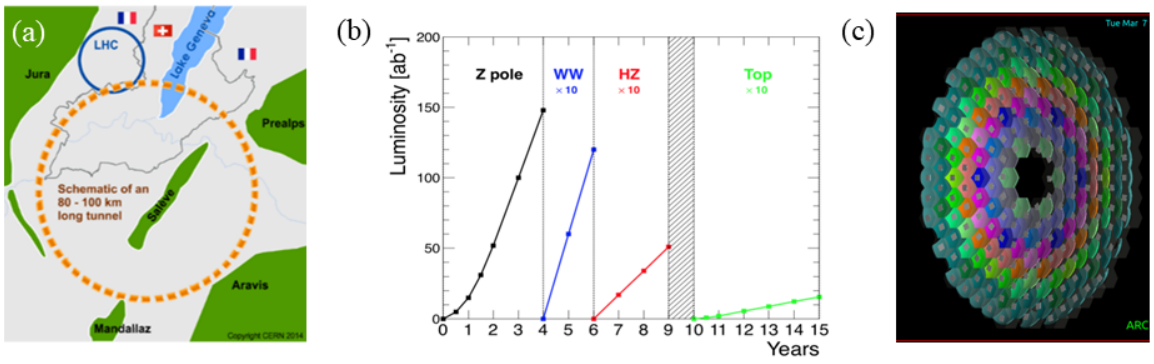

Fig. 106: (a) Possible siting of the FCC in the CERN region; (b) luminosity as a function of time that could be achieved in FCC-ee, for operation at various energies [152]; (c) example of detector R&D for FCC-ee—design for the cells of a lightweight RICH detector [155].

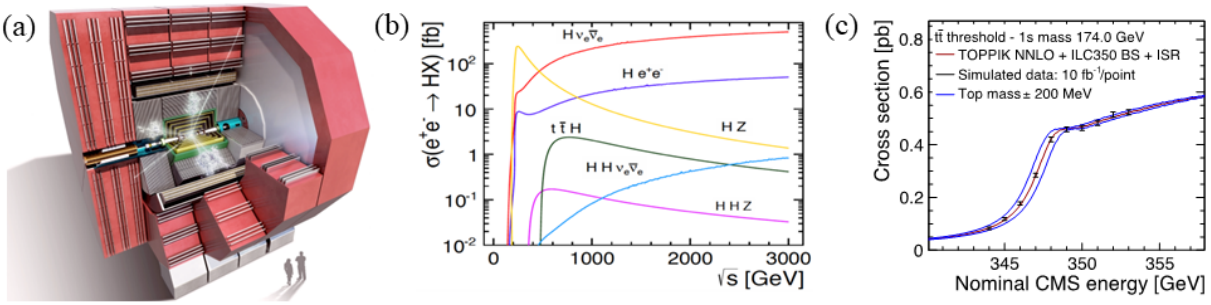

Fig. 107: (a) Layout of a proposed experiment at an e^+e^- Higgs Factory; (b) cross-sections vs centre-of-mass energy; (c) example of a possible scan of the top-quark pair-production threshold [154].

by electricity, and recently the cost has increased, in addition to the environmental concerns. The LHC uses $\sim$ 200 MW when running. Electricity provided to CERN is already climate friendly—nuclear (from France) and renewable (from Switzerland), 90% carbon-free. But we must continue to strive for improvement for future colliders: e.g. more efficient RF, increased use of renewable energy, possible use of Energy-Recovery Linac technology to extract energy from the beams after they have collided, or use of permanent magnets, etc. FCC-ee is the most energy efficient of the Higgs factory proposals (up to the energy for $t\bar{t}$ production), as shown in Fig. 109 (a).

Going further

After the Higgs Factory, the priority will be to push the energy frontier as far as possible, in particular if deviations from the Standard Model have been seen in the precision Higgs + Electroweak measurements. Advanced accelerating techniques are under study to reach higher accelerating gradients, to allow for more compact colliders. Limitations in current RF structures come from discharges due to material imperfections, which could be overcome by avoiding solid structures and using a *plasma* instead. Wake-fields can be induced in a plasma using a laser or drive beam, and then injected electrons "surf" the waves to high energy, see Fig. 109 (b). Such developments aim to reach gradients > GV/m: e.g. at the AWAKE facility at CERN.[46]

[46] It will be more tricky to accelerate positrons with such an accelerator technology, though.

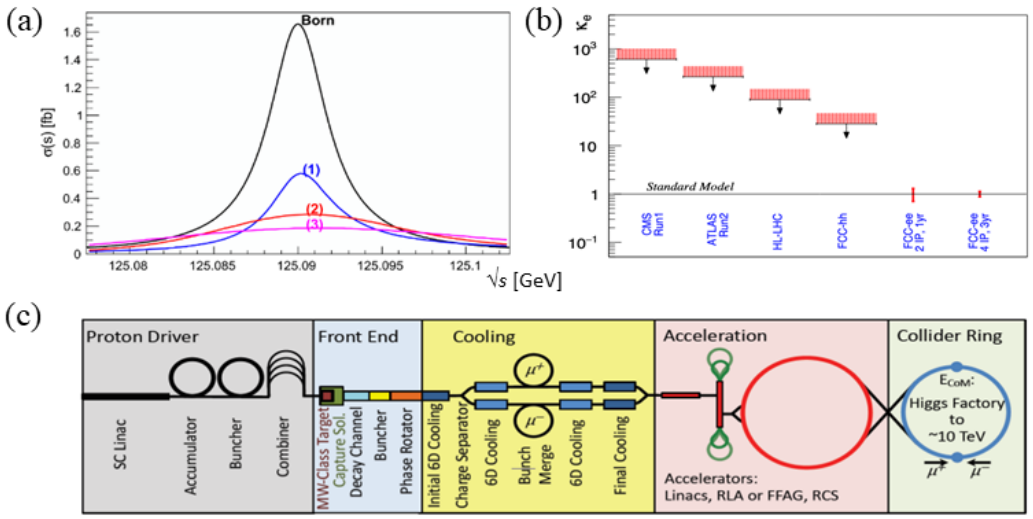

Fig. 108: (a) s-channel production of the Higgs boson, $e^+e^- \to H$, and the influence of realistic beam energy spread on the measured cross-section; (b) sensitivity to s-channel production at various facilities [156]; (c) the components of a Muon Collider [157].

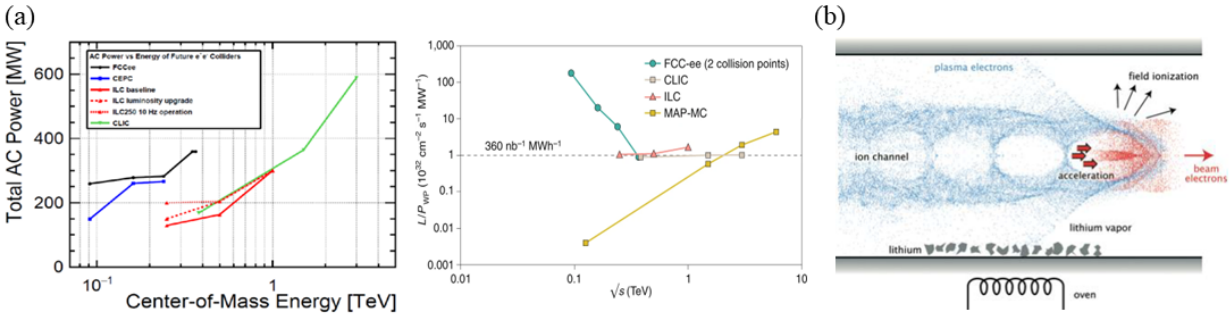

Fig. 109: (a) The total power vs centre-of-mass energy required for various future colliders (left), and rescaled to show the luminosity achieved per MW of power (right) [158]; (b) using wakefields in a plasma to accelerate electrons [159].

While waiting for a breakthrough in accelerating technology, or demonstration of the feasibility of the Muon Collider discussed above, it is planned to re-use FCC tunnel for a *hadron* collider at the energy frontier in the same way that the LHC followed LEP. Its circumference will be 3.5 × that of the LHC, so it will need to use high-field magnets to reach ≥ 100 TeV pp collisions: Nb_3Sn should allow 16 T to be achieved, and high-temperature superconductor (HTS) even higher, see Fig. 110 (a); since the envisioned start date for FCC-hh is only $\sim$ 2070 there is plenty of time for R&D! At high energy a detailed study of HH production and the Higgs potential can be made, and the search for new physics extended by a big step. The experiments will need to be even larger than at LHC, as illustrated in Fig. 110 (b), and will have to be designed to survive very high radiation dose and pileup $\mathcal{O}(1000)$.

4.5 Summary of the fourth lecture

The Standard Model is very successful, but we know it is not the full story. Many searches have been made at the LHC, but so far no clear signs of new physics have been seen: Supersymmetry, Dark Matter

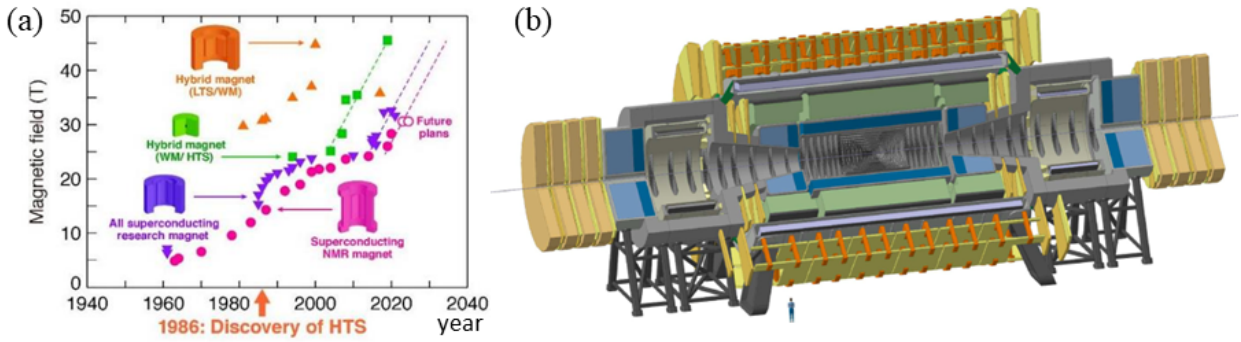

Fig. 110: (a) Increase in magnetic field that has been achieved in different magnet types as a function of year (although note that accelerator magnet design is more demanding than the test magnets shown here) [160]; (b) design of an experiment for the FCC-hh [161].

or other BSM. Hints of new physics have been claimed in a few corners—the flavour anomalies, the W mass from CDF, muon $(g-2)$—but they remain unconvincing, further experimental and/or theoretical consolidation is needed. As a result, the searches are being widened: both within the LHC, e.g. looking for long-lived particles, or going beyond colliders to search for feebly-interacting particles—for which new experiments are being proposed right now. There is a clear future for collider physics, first with higher luminosity at HL-LHC, where fast timing will be important to suppress pileup; and then at a new future collider, that most likely will be an e^+e^- Higgs Factory. The feasibility of the FCC is under study at CERN, with a decision expected around 2026; if approved it will provide physics for many decades to come: an Electroweak and Higgs Factory (FCC-ee) followed by a hadron collider (FCC-hh) at 100 TeV or beyond—that I see as a very exciting prospect! I hope you will participate in this adventure, furthering the quest to understand the hidden secrets of the Universe.

Acknowledgements

I gathered the material for these lectures from many sources, in particular the previous lectures in this series of schools given by Cecilia Gerber [22], Paris Sphicas [18], and Peter Jenni [3], as well as those on detector instrumentation from Christian Joram [26]. Many thanks to them—and to those they borrowed from in turn. It is also a pleasure to thank the organisers of the school for giving me the opportunity to visit such a remarkable place, and the students for their enthusiasm and curiosity.

References

[1] L. de Broglie, Ann. Phys. 3 (1925) 22.

[2] Figure from https://ep-news.web.cern.ch/content/how-many-fundamental-constants-does-it-take-explain-universe.

[3] P. Jenni, lectures at CLASHEP, Ecuador, 2015.

[4] E. Noether, Nachrichten von der Gesellschaft der Wissenschaften zu Göttingen (1918) 235.

[5] R. Brout and F. Englert, Phys. Rev. Lett. 13 (1964) 321; P.W. Higgs, Phys. Rev. Lett. 13 (1964) 508.

[6] R.L. Workman *et al.* (Particle Data Group), Prog. Theor. Exp. Phys. (2022) 083C01; see https://pdg.lbl.gov/.

[7] P. Koppenburg, LHCb-FIGURE-2021-001, and updates.

[8] R. Aaij *et al.* (LHCb collab.) Phys. Rev. Lett. 115 (2015) 072001.

[9] A.D. Sakharov, J. of Exp. and Theor. Phys. Lett. 5 (1967) 24.

[10] Planck collab., Astronomy and Astrophys. 641 (2020) A1.

[11] R. Amanullah *et al.* Supernova Cosmology Project, Astrophys. J. 716 (2010) 712.

[12] E. Corbelli and P. Salucci, Monthly Notices of the Royal Astronom. Soc. 311 (2000) 441447.

[13] D. Farrah *et al.* Astrophys. J. Lett. 944 (2023) L31.

[14] E.O. Lawrence, patent application, 1932.

[15] M.S. Livingston (1954), updated version from J. Spentzouris *et al.*, J. Phys. Conf. Series 125 (2008) 012005.

[16] LEP and SLD collab., Phys. Rep. 427 (2006) 257.

[17] Figure from https://web.pa.msu.edu/people/huston/cteq4lhc/higgs/cteq4lhc_higgs.html.

[18] P. Sphicas, lectures at CLASHEP, Mexico, 2017.

[19] J. Liouville, J. de mathématiques pures et appliquées 3 (1838) 342.

[20] Amazingly (to me, at least) the answer is not that the collider would move imperceptibly, given that 1 m $\ll$ 50,000 km: in fact it would move by 1 m$/2\pi \approx 16$ cm, since the radius of a circle is just given by the circumference$/2\pi$; this apparent paradox merits its own entry in Wikipedia: https://en.wikipedia.org/wiki/String_girdling_Earth.

[21] Figure from M. Jeitler, "Particle Physics: Status and Perspectives" SS 2014.

[22] C. Gerber, lectures at CLASHEP, Argentina, 2019.

[23] A high pileup event from CMS, CMS-PHO-EVENTS-2012-006-5.

[24] A. Djouadi *et al.*, DESY 97-079 (1997).

[25] E. Rutherford, The London, Edinburgh, and Dublin Philosoph. Mag. and J. of Sci. 21 (1911) 669.

[26] C. Joram, "Basics of Particle Detection", lectures at CBPF, Rio de Janeiro, Brazil (2017).

[27] L. Ropelewski, "Introduction to the Micropattern Gaseous Detectors", CSEM-CERN meeting, 2013.

[28] J. Alme *et al.*, NIM A 622 (2010) 316; J. Adolfsson *et al.*, JINST 16 (2021) P03022.

[29] ATLAS Liquid Argon Calorimeter Technical Design Report, CERN/LHCC/96-41.

[30] R.E. Kalman, J. of Basic Eng. 82 (1960) 35.

[31] Plenty of such plots can be found here: https://twiki.cern.ch/twiki/bin/view/CMSPublic/PixelOfflinePlotsOctober2018.

[32] Figure from https://cms.cern/detector/identifying-tracks/silicon-pixels.

[33] L. Musa and S. Beolé, "ALICE tracks new territory", CERN Courier 2021.

[34] D. Cockerill, "Introduction to Calorimeters", lectures at Southampton (2016).

[35] M. Thomson, NIM A 611 (2009) 25.

[36] Figure from https://hamamatsu.magnet.fsu.edu/articles/photomultipliers.html.

[37] Hamamatsu Photonics (Japan).

[38] T. Gys, RICH 2007, Trieste.

[39] A. Gola *et al.*, Sensors 19 (2019) 308.

[40] N. Agafonova *et al.* (OPERA colab.) Prog. Theor. Exp. Phys. (2014) 101C01.

[41] CMS collab., JINST 13 (2018) P05011.

[42] ATLAS collab. webpages: https://twiki.cern.ch/twiki/bin/view/AtlasPublic.

[43] CMS collab., Eur. Phys. J. C 74 (2014) 3076.

[44] ATLAS collab., Phys. Rev. D 90 (2014) 052004.

[45] J. Engelfried *et al.* (SELEX collab.) FERMILAB-PUB-98/299-E.

[46] LHCb collab. webpages:
https://lhcb-outreach.web.cern.ch/category/physics-results/.

[47] ALICE collab., Int. J. Mod. Phys. A 29 (2014) 1430044.

[48] R. Calabrese *et al.* (LHCb collab.) JINST 17 (2022) P07013.

[49] F. Tegenfeldt (DELPHI collab.) Ph.D thesis, Uppsala 2001.

[50] I. Adam *et al.* (BaBar collab.) NIM A 433 (1999) 121.

[51] A.M. Sirunyan *et al.* (CMS collab.) JINST 13 (2018) P06015.

[52] V.V. Gligorov and E. Rodrigues (LHCb collab.) LHCb-FIGURE-2020-016.

[53] See https://wlcg.web.cern.ch/.

[54] CMS collab. webpages: https://cms.cern/news/physics-results

[55] ALICE collab. webpages:
https://twiki.cern.ch/twiki/bin/view/ALICEpublic/ALICEPublicResults

[56] ATLAS collab., Summary plots (2017) https:
//atlas.web.cern.ch/Atlas/GROUPS/PHYSICS/CombinedSummaryPlots/SM/index.html.

[57] ATLAS collab., CERN-EP-2022-281.

[58] C. Barschel, Ph.D thesis, Rheinisch-Westfälische Technische Hochschule (2013)
CERN-THESIS-2013-301.

[59] ATLAS collab., Phys. Lett. B 722 (2013) 305.

[60] ATLAS collab., Nucl. Phys. B 889 (2014) 486, and references therein.

[61] LHCf collab., Phys. Lett. B 780 (2018) 233.

[62] M. Cacciari, G.P. Salam and G. Soyez, JHEP 04 (2008) 063.

[63] R. Atkin, J. Phys. Conf. Ser. 645 (2015) 012008.

[64] ATLAS collab., Eur. Phys. J. C 75 (2015) 17.

[65] ATLAS collab., Eur. Phys. J. C 81 (2021) 689.

[66] CMS collab., JHEP 03 (2017) 156.

[67] CMS collab., CERN-EP-2016-277.

[68] CMS collab., Eur. Phys. J. C 75 (2015) 288.

[69] ALICE collab., Phys. Rev. C 101 (2020) 034911.
[70] CMS collab., Phys. Rev. Lett. 109 (2012) 222301.
[71] A. Schmidt, "Jet substructure in CMS", seminar at RAL (2016).
[72] CMS collab., JHEP 08 (2023) 204.
[73] M. Alhroob (ATLAS collab.) EPS Conf. on HEP, Ghent, 2017.
[74] ATLAS collab., ATLAS-CONF-2013-046.
[75] ATLAS collab., Eur. Phys. J. C 74 (2014) 3109.
[76] ATLAS and CMS collab., JHEP 04 (2018) 033.
[77] Figure from Wikipedia, based on a lecture of S. Boyd (Warwick).
[78] L. Wolfenstein, Phys. Rev. Lett. 51 (1983) 1945.
[79] Physics Briefing Book for the ESPP, CERN-ESU-004 (2020).
[80] LHCb collab., Nature Phys. 18 (2022) 1.
[81] A.J. Buras and R. Fleischer, TUM-HEP-275/97, in "Heavy Flavours II", World Scientific (1997).
[82] LHCb collab., Phys. Rev. Lett. 115 (2015) 031601.
[83] ARGUS collab., Phys. Lett. B 192 (1987) 245.
[84] CERN Courier, "LHCb looks forward to the 2030s", March 2023, adapted from CKMfitter.
[85] LHCb collab., Phys. Lett. B 777 (2018) 16.
[86] LHCb collab., Phys. Rev. Lett. 128 (2022) 041801.
[87] D.M. Straub, arXiv:1012.3893v2, presented at CKM2010, Warwick.
[88] CMS collab., J. High Energy Phys. 10 (2011) 132.
[89] ATLAS collab., Eur. Phys. J. C 77 (2017) 367.
[90] CMS collab., CMS-PAS-EWK-11-019.
[91] CMS collab., Phys. Rev. D 90 (2014) 032004.
[92] ATLAS collab., Eur. Phys. J. C 78 (2018) 110.
[93] ATLAS collab., JHEP 05 (2018) 077.
[94] CMS collab., JHEP 03 (2014) 032.
[95] J. Manjarrés (ATLAS collab.) ATL-PHYS-SLIDE-2021-020.
[96] ATLAS collab., ATLAS-CONF-2018-030.
[97] ATLAS collab., ATLAS-CONF-2017-045.
[98] CMS collab., CMS-PAS-HIG-19-001.
[99] G. Degrassi *et al.*, CERN-PH-TH/2012–134; J.R. Espinosa, LATTICE 2013.
[100] CMS collab., Nat. Phys. 18 (2022) 1329.
[101] ATLAS collab., CERN-EP-2023-023.
[102] L.D. Landau, Dokl. Akad. Nauk SSSR 60 (1948) 207; C.N. Yang, Phys. Rev. 77 (1950) 242.
[103] ATLAS collab., Eur. Phys. J. C 75 (2015) 476.
[104] CMS collab., Phys. Rev. Lett. 121 (2018) 121801.
[105] ATLAS collab., Phys. Lett. B 786 (2018) 59.

[106] ATLAS-collab., Nature 607 (2022) 52.
[107] CMS collab., Nature 607 (2022) 60.
[108] CMS collab., Phys. Lett. B 793 (2019) 520.
[109] CMS collab., JHEP 01 (2021) 148.
[110] CMS collab., JHEP 03 (2020) 131.
[111] ATLAS collab., JHEP 07 (2023) 166.
[112] ATLAS collab., Phys. Lett. B 800 (2020) 135103.
[113] U. Amaldi *et al.*, Phys. Lett. B 260 (1991) 447.
[114] L. Randall, "A New View of Weak Scale Physics", Harvard.
[115] CMS collab., JHEP 04 (2019) 031.
[116] ATLAS collab., Phys. Rev. D 88 (2013) 072001.
[117] J. Manjarrés (ATLAS collab.) DESY colloquium, May 2019.
[118] L. Hsu, ICHEP 2020, Prague.
[119] A. Boveia *et al.*, LHC DM Working Group, CERN-LPCC-2016-001.
[120] CMS collab., Phys. Rev. D 97 (2018) 092005.
[121] ATLAS collab., JHEP 09 (2016) 001.
[122] CMS collab., Phys. Rev. Lett. 117 (2016) 051802.
[123] ATLAS collab., ATLAS-CONF-2016-059.
[124] LHCb collab., Phys. Rev. Lett. 108 (2012) 181806.
[125] LHCb collab., JHEP 06 (2014) 133.
[126] HFLAV, https://hflav.web.cern.ch/.
[127] W. Altmannshofer and P. Stangl, arXiv:2103.13370.1.
[128] LHCb collab., Nature Phys. 18 (2022) 277.
[129] LHCb collab., JHEP 08 (2017) 055.
[130] LHCb collab., Phys. Rev. Lett. 131 (2023) 051803.
[131] Figures from A. Keshavarzi, "The Muon g-2 Experiment at Fermilab", PhiPsi 2019.
[132] T. Aoyama *et al.*, Phys. Rev. Lett. 109 (2012) 111808.
[133] B. Abi *et al.* (Muon g-2 collab.) Phys. Rev. Lett. 126 (2021) 141801.
[134] T. Aoyama *et al.* Phys. Rep. 887 (2020) 1.
[135] J. Alimena *et al.*, J. Phys. G 47 (2020) 090501.
[136] ATLAS collab., Phys. Rev. Lett. 122 (2019) 151801.
[137] CMS collab., JHEP 05 (2018) 127.
[138] MoEDAL collab., Eur. Phys. J. C 82 (2022) 694.
[139] FASER collab., Phys. Rev. D 104 (2021) 091101.
[140] FASER collab., Phys. Rev. D 99 (2019) 095011.
[141] See https://pbc.web.cern.ch/.
[142] E. Cortina Gil *et al.* (NA62 collab.), JHEP 06 (2021) 093.

[143] E. van Herwijnen (SHiP collab.) PoS (ICHEP2016) 490.

[144] ESPP update (2020), https://home.cern/resources/brochure/cern/european-strategy-particle-physics.

[145] O. Brüning *et al.*, Rep. Prog. Phys. 85 (2022) 046201.

[146] ATLAS collab., "A High-Granularity Timing Detector for the ATLAS Phase-2 Upgrade", CERN-LHCC-2020-007.

[147] CMS collab., "A MIP Timing Detector for the CMS Phase-2 Upgrade", CERN-LHCC-2019-003; S. Grinstein, IAS-HEP 2021.

[148] ATLAS collab., ATL-PHYS-PUB-2013-011.

[149] ATLAS collab., ATL-PHYS-PUB-2013-014.

[150] LHCb collab., Framework TDR for LHCb Upgrade II, CERN-LHCC-2021-012.

[151] ALICE collab., Letter of Intent for ALICE 3, CERN-LHCC-2022-009.

[152] A. Abada *et al.*, Eur. Phys. J 228 (2019) 261.

[153] ILC Technical Design Report (2013), https://linearcollider.org/technical-design-report/.

[154] CLIC Conceptual Design Report, CERN-2012-007.

[155] R. Forty, "ARC: a solution for particle identification at FCC-ee", FCC week 2021; figure from A. Tolosa Delgado.

[156] D. d'Enterria *et al.*, Eur. Phys. J. 137 (2022) 201.

[157] J.P. Delahaye *et al.*, arXiv:1901.06150.

[158] I. Agapov *et al.*, Proceedings of Snowmass 2021, arXiv:2203.08310v1

[159] R. Pattathil, 111$^{\text{th}}$ Plenary ECFA Meeting, November 2022.

[160] H. Maeda and Y. Yanagisawa, J. Magn. Reson. 306 (2019) 80.

[161] FCC-hh Conceptual Design Report, Eur. Phys. J. 228 (2019) 755.